UC San Diego
UC San Diego Electronic Theses and Dissertations

Title
Gyrokinetic studies of particle transport in tokamaks

Permalink
https://escholarship.org/uc/item/554020j5

Author
Estrada-Mila, Carlos A.

Publication Date
2006

Peer reviewed|Thesis/dissertation

eScholarship.org Powered by the California Digital Library
University of California

UNIVERSITY OF CALIFORNIA, SAN DIEGO

Gyrokinetic Studies of Particle Transport in Tokamaks

A dissertation submitted in partial satisfaction of the
requirements for the degree Doctor of Philosophy

in

Engineering Sciences (Engineering Physics)

by

Carlos A. Estrada-Mila

Committee in charge:

Sergei I. Krasheninnikov, Chair
Jeff Candy
Thomas M. O'Neil
Sutanu Sarkar
George R. Tynan
Ronald E. Waltz

2006

Copyright
Carlos A. Estrada-Mila, 2006
All rights reserved.

The dissertation of Carlos A. Estrada-Mila is approved, and it is acceptable in quality and form for publication on microfilm:

Chair

University of California, San Diego

2006

TABLE OF CONTENTS

Signature Page iii

Table of Contents iv

List of Figures vii

List of Tables x

Acknowledgements xi

Vita and Publications xii

Abstract of the Dissertation xiii

1 Introduction 1
- 1.1 The problem of transport 3
- 1.2 Historical background 4
  - 1.2.1 Fluid models 6
  - 1.2.2 Gyrofluid models 7
  - 1.2.3 Kinetic models 8
- 1.3 The gyrokinetic approach 8
- 1.4 Outline of the dissertation 11
  - 1.4.1 Chapter 2: Theoretical background 11
  - 1.4.2 Chapter 3: Particle transport in a pure plasma 12
  - 1.4.3 Chapter 4: Particle transport in impure plasmas 13
  - 1.4.4 Chapter 5: Turbulent transport of alpha particles 14

2 Theoretical Background 15
- 2.1 Introduction 15
- 2.2 Gyrokinetic ordering 15
- 2.3 The ion gyrokinetic equation 16
- 2.4 Field-aligned coordinates 17
- 2.5 The ion gyrokinetic equation in flux tube geometry 18
- 2.6 The Poisson equation 21
- 2.7 The gyroaverage operator 22
- 2.8 Example: The $s - \alpha$ equilibrium 23

3 Particle Transport in a Pure Plasma 27
- 3.1 Introduction 27
- 3.2 Units and conventions 29
- 3.3 Nonlinear simulations 30
- 3.4 Characteristics of a thermal pinch 31

- 3.5 Effect of electron collisions on a thermal pinch 32
- 3.6 Pinch due to electron curvature drift 34
- 3.7 The problem of density peaking 35
- 3.8 Conclusions 39
- 3.9 Acknowledgement 40

4 Particle Transport in Impure Plasmas 41
- 4.1 Introduction 41
- 4.2 Units and conventions 42
- 4.3 Quasilinear results 43
- 4.4 Density gradient effects 43
- 4.5 Dilution effects 45
  - 4.5.1 Inward impurity peaking 46
  - 4.5.2 Outward impurity peaking 48
  - 4.5.3 The dilution model 48
  - 4.5.4 The lumped-mass approximation 48
- 4.6 Particle transport in D-T plasmas 49
- 4.7 Analysis 51
  - 4.7.1 General theory 52
  - 4.7.2 Helium pinch formation 54
  - 4.7.3 Density gradient and dilution effects on energy confinement 55
  - 4.7.4 DT flow separation 57
  - 4.7.5 On the accuracy of selected approximations 60
- 4.8 Conclusions 62
- 4.9 Acknowledgement 63

5 Turbulent Transport of Alpha Particles 64
- 5.1 Introduction 64
- 5.2 Alpha particle physics 66
  - 5.2.1 Slowing-down form of the alpha particle distribution 66
  - 5.2.2 An equivalent alpha-particle Maxwellian 68
  - 5.2.3 Alpha particle profiles in ITER 70
- 5.3 Simulation units and conventions 71
- 5.4 GYRO simulations 72
  - 5.4.1 Nonlinear temperature scan 74
  - 5.4.2 Quasilinear GYRO scans 76
- 5.5 Discussion of results 79
  - 5.5.1 General features and relevance of alpha transport 79
  - 5.5.2 Implications for alpha confinement 82
- 5.6 Analysis 83
  - 5.6.1 General theory 84
  - 5.6.2 Helium pinch 86
  - 5.6.3 Turbulence decay at high energies 89

5.7 Conclusions . . . 92
5.8 Acknowledgement . . . 92

6 Conclusions . . . 93

A Units and Conventions . . . 95
A.1 Units . . . 95
A.2 Diffusivities and Fluxes . . . 95
A.3 Gradient scale lengths . . . 96

B The $s - \alpha$ equilibrium in Shafranov Coordinates . . . 97

C The GYRO Code . . . 100
C.1 Code variables . . . 101
C.2 Numerical techniques . . . 101
C.2.1 Radius ($r \rightarrow \mathtt{i}$) . . . 102
C.2.2 Poloidal angle ($\tau \rightarrow \mathtt{m}$) . . . 102
C.2.3 Toroidal angle ($n \rightarrow \mathtt{n}$) . . . 103
C.2.4 Velocity Space ($(\lambda, \epsilon) \rightarrow (\mathtt{k}, \mathtt{ie})$) . . . 103
C.2.5 Nonlinearity . . . 103
C.2.6 Time-advance . . . 104

Bibliography . . . 105

LIST OF FIGURES

1.1 Schematic diagram of a tokamak. [Figure courtesy of EFDA-JET.] 2

3.1 Effect of high $k_\theta \rho_s$ on particle flow at two different resolutions: S/F and L/C (see Table 3.1). 32
3.2 L_{Te} scan (at fixed L_{ne}, with $L_{Te} = L_{Ti}$). Plot (a) compares the total ion particle (dotted line) and thermal (solid lines) diffusivity from GYRO (circles) to that from GLF23 (squares). In plot (b), a similar comparison is presented for the electron diffusivities. 33
3.3 Ion particle flow (a) and electron particle flow (b) separated into trapped and passing fractions. The flows are normalized to $\chi_{ie} \doteq (\chi_i + \chi_e)/2$. . . 33
3.4 Dependence of the normalized electron particle flow on magnetic shear (s). The dashed-dotted line (P+C) shows parallel plus curvature effects. The dashed line (P) shows parallel effects only, whereas the the dotted line shows curvature effects (C) only. The crossing point at $s = -3/8$ is indicated with a cross. The solid line shows thermodiffusion effects ($1/L_{Te} = 3$). 34
3.5 DIII-D profile data for discharge 101391. Plot (a) shows experimental electron density and temperature profiles, while plot (b) shows the calculated electron-ion collisionality based on these profiles. The vertical dotted lines denote the radial domain used in the simulations. 36
3.6 Radial electron particle flow in MW/keV (a) and average energy flow in MW (b) from baseline simulation (solid line), compared to their experimental counterparts. 37
3.7 Plot (a) shows the variation of radial electron particle flow as $1/L_{te}$ is increased by 10% and 20% while $1/L_{ne}$ is kept fixed. Plot (b) shows the same variation when $1/L_{ne}$ is decreased by 10% and 20% and $1/L_{te}$ is kept fixed. 39
3.8 Variation of radial electron particle flow as $1/L_{te}$ is increased and $1/L_{ne}$ is decreased simultaneously by 10% and 20%. 40

4.1 Normalized impurity flow, D_{He}, versus $L_{n\mathrm{He}}$ scan (at fixed $L_{ne} = 1$) for two different impurity concentrations: $f_{\mathrm{He}} = 0.1$ and 0.3. Quadrant 1 refers to outward flow and a peaked profile, 2 to inward flow and peaked profile, 3 to outward flow and hollow profile, and 4 to inward flow and hollow profile. Plot (a) shows GLF23 results while plot (b) shows GYRO results. 44
4.2 Same as Fig. 4.1, except showing the main ion flow, D_i/χ_i, rather than the impurity flow, D_{He}/χ_i. As before, plot (a) shows GLF23 results while plot (b) shows GYRO results (both at fixed $L_{ne} = 1$). According to Eq. (4.3), $1/L_{ni} > 0$ in these scans. 45

4.3 Helium diffusivity, D_{He}, versus $L_{n\mathrm{He}}$ scan (at fixed $L_{ne} = 1$) for two different impurity concentrations: $f_{\mathrm{He}} = 0.1$ (solid line) and 0.3 (dashed line), using GYRO. The diffusive term D^d_σ is given by the vertical intercept of the graph whereas the convective velocity v_{in} is given by its slope. The dotted line shows the results for adiabatic electrons at $f_{\mathrm{He}} = 0.1$. 46
4.4 Particle flow, D_i and D_{He} as functions of impurity fraction, f_{He}. Here, two different impurity density gradients, $1/L_{n\mathrm{He}} = \pm 1$, are considered. Plot (a) compares D_{He} results for GLF23 and GYRO, while plot (b) compares D_i results. 47
4.5 GYRO f_{He} scans for $1/L_{n\mathrm{He}} = \pm 1$, comparing the dilution model with full kinetic dynamics. Plot (a) shows GYRO runs at $1/L_{n\mathrm{He}} = -1$ while plot (b) shows GYRO runs at $1/L_{n\mathrm{He}} = 1$. In both cases the lumped-mass approximation is included (triangle at $f_{\mathrm{He}} = 0.3$). 49
4.6 Comparison of D-T transport coefficients with those from a pure-D plasma (solid curves). In the two-component DT simulation, we obtain separate transport coefficients for deuterium (dotted curve) and tritium (dashed curve). Plot (a) compares χ while plot (b) compares D. Recall that the normalization, χ_{GBD}, is computed with respect to pure deuterium. 51
4.7 Comparison of collisionless and collisional DT simulations for different values of $1/L_{Te}$. As usual the density gradient is fixed ($L_{ne} = 1$) and the electron and ion temperature gradients are equal ($L_{Te} = L_{TD}$). 52
4.8 Comparison of eigenfrequencies for theory including nonperturbative drift resonance (solid curves) with those from the nonresonant expansion (dotted curves). GA Standard Case parameters for a 50-50 D-T plasma are used. 61
4.9 Plot (a) compares three GYRO calculations of the quasilinear deuterium flow in a 50-50 D-T plasma for the GA Standard Case. GYRO (1) makes no approximation. GYRO (2) neglects particle trapping by setting $r = 0.05$ (whereas GYRO (1) has $r = 0.5$) and GYRO (3) ignores the parallel motion (ion-sound physics) altogether. Plot (b) compares the GYRO (3) simulation with the full local kinetic theory (Theory 1, which uses Eq. (4.14)) and the long-wavelength local kinetic theory (Theory 2, which uses the simpler Eq. (4.16)). 62

5.1 Comparison of slowing-down (F_{S}) and Maxwellian distributions weighted by v^2 for $T_e = 15\,\mathrm{keV}$. F_{M} (dotted line) shows a Maxwellian with equivalent temperature given by Eq. (5.14), and used in all our simulations. F_{M1} and F_{M4} denote the resulting ditributions if v-moments and v^4-moments were matched instead. 68
5.2 ITER-FEAT profile data for electrons and ions (a) and energetic helium (alpha particles) (b). Data in part (b) was computed using Eqs. (5.7) and (5.14) and complemented with SPOT simulations [93]. 70

5.3 Dependence of energy diffusivity (a) and particle diffusivity (b) on the temperature ratio, $\lambda_\alpha = T_\alpha/T_e$, for deuterium and electrons for $\eta_{\mathrm{He}} = 0.1$. The helium fraction is $n_\alpha/n_e = 0.005$. Otherwise, GA standard case parameters are used. 73
5.4 Same as previous figure, except $\eta_\alpha = 3.0$. 74
5.5 Dependence of the normalized helium energy flux (a) and helium particle flux (b) on $\lambda_\alpha = T_\alpha/T_e$. Data is from the same simulations as in Fig. 5.3. 75
5.6 Same as previous figure, but the data is from the simulations shown in Fig. 5.4. 76
5.7 Comparison of $k_\theta\rho_\alpha$-dependence of the normalized helium energy flux (a) and helium particle flux (b) for three different temperatures ($\lambda_\alpha = 1, 10, 40$) at $\eta_\alpha = 0.1$. The solid line ($[J_0(k_\theta\rho_\alpha)]^2$) is a measure of gyroaveraging effects. 77
5.8 Comparison of nonlinear simulation results with quasilinear theory for helium energy fluxes (a) and helium particle fluxes (b) as functions of λ_α. The fluxes are normalized to the deuterium energy flux. Solid curves show full nonlinear simulation results (GYRO-NL), while dotted curves show quasilinear results (GYRO-QL) at fixed $k_\theta\rho_s = 0.2$. 78
5.9 Same as previous figure, except $\eta_\alpha = 3.0$. 79
5.10 Quasilinear scan showing magnetic shear dependence of the helium transport fluxes for $\eta_\alpha = 3.0$. 80
5.11 Quasilinear scan showing η_α dependence of the helium transport for $s = 1$. 81
5.12 Growth rate (γ) and helium density (n_α) as a function of the minor radius (r/a) for ITER parameters. The vertical line shows the reference point ($r/a = 0.5$) used in the simulations. 83
5.13 Comparison of quasilinear theory with analytic resonant integral theory for helium energy diffusivity (a) and helium particle diffusivity (b) as functions of λ_α. 86
5.14 Large-λ_α form of the energetic helium (alpha-particle) response function for $k_\theta\rho_s = 0.05$ (a), $k_\theta\rho_s = 0.2$ (b), and $k_\theta\rho_s = 0.4$ (c). Solid lines show the full resonant theory as defined in Eq. (5.42), and dotted lines show the $\lambda^{-3/2}$-theory of Eq. (5.48). We have plotted the low-$k_\theta\rho_s$ formula, given by Eq. (5.50, as a dashed curve in (a). Similarly, we have plotted the high-$k_\theta\rho_s$ formula, given by Eq. (5.51), in (c). 91

B.1 $s - \alpha$ equilibrium in Shafranov Coordinates. 98

LIST OF TABLES

3.1 Results for box-size and perpendicular-grid-size convergence study. In the "Simulation" column, L=Large Box, S=Small Box; C=Coarse Grid, F=Fine Grid. 31

4.1 Summary of deuterium-tritium plasma study. All quantities already normalized to χ_{GBD} (deuterium gyroBohm diffusivity). The D-simulation is the base GA Standard Case. The collisional D+T simulation has a relatively small collision frequency: $\nu_e = 0.01$. Note that the identical value 11.73 in two separate cases is not a typo. 50
4.2 Physical realism of linear, adiabatic-electron calculations summarized in Table 4.3. "Trapping" refers to ion trapping, "parallel motion" to treating $\partial/\partial\theta$ and the θ-dependence of the drifts exactly, "FLR" to full inclusion of finite-larmor-radius effects, and "drift resonance" to a nonperturbative treatment of the curvature drift resonance. RF denotes the "root finder" solution of Eqs. (4.14) and (4.15), while "analytic" refers to Eqs. (4.21) and (4.22). 57
4.3 Summary of growth rate shift, γ/γ_0, for $1/L_{n\mathrm{He}} = \pm 1$ and $f_{\mathrm{He}} = 0.1, 0.3$, for each of the six models outlined in Table 4.2. Here, γ_0 refers to the growth rate at $f_{\mathrm{He}} = 0$ for a given $1/L_{n\mathrm{He}}$ and model. 58

5.1 T_e-dependence of parameters related to the alpha-particle distribution. Here, T_α and λ_α are the equivalent alpha-particle Maxwellian temperatures for each value of T_e. 67
5.2 T_e-dependence of $\lambda_\alpha \doteq T_\alpha/T_e$. Here, $\lambda_\alpha^{(1)}$ and $\lambda_\alpha^{(4)}$ denote the equivalent alpha-particle Maxwellian temperatures obtained by matching v-moments and v^4-moments respectively. 69
5.3 Approximate expected local alpha parameters in ITER, ignoring finite-orbit effects. 71
5.4 Comparison between alpha particles fluxes and total helium ash fluxes (alpha ash + recycling). 82
5.5 Eigenvalues for the resonant integral model. Here, STD case parameters are used, assuming $f_{\mathrm{D}} = 1$ and $f_\alpha = 0$. 87
5.6 Helium null-flow temperatures (for which $\Gamma_\alpha = 0$) as predicted by different theories. Here, QL refers to a quasilinear simulation (GYRO-QL), RI refers to the resonant integral theory of Eq. (5.42), and NR refers to the nonresonant formula given by Eq. (5.41). 88

A.1 Summary of basic units. 96

ACKNOWLEDGEMENTS

I would like to thank Dr. J.Candy and Prof. R.E. Waltz for all their help, patience and vote of confidence during my graduate studies. I would also like to acknowledge Prof. S.I. Krasheninnikov for serving as the liaison between General Atomics and UCSD.

The text of this dissertation, in part, includes material from "Gyrokinetic simulations of ion and impurity transport" [C. Estrada-Mila, J. Candy and R.E. Waltz, Phys. Plasmas **12**, 022305 (2005)], "Density peaking and turbulent pinch in DIII-D discharges" [C. Estrada-Mila, J. Candy and R.E. Waltz, submitted to Phys. Plasmas (2006)] and "Turbulent transport of alpha particles in reactor plasmas" [C. Estrada-Mila, J. Candy and R.E. Waltz, submitted to Nucl. Fusion (2006)]. The dissertation author was the primary researcher.

VITA

2000	B.S., Universidad Pontificia Bolivariana, Medellín, Colombia.
2003	M.S., University of California, San Diego.
2006	Ph.D., University of California, San Diego.

ABSTRACT OF THE DISSERTATION

Gyrokinetic Studies of Particle Transport in Tokamaks

by

Carlos A. Estrada-Mila
Doctor of Philosophy in Engineering Sciences (Engineering Physics)

University of California San Diego, 2006

Sergei I. Krasheninnikov, Chair

In this dissertation a systematic study of particle transport in tokamaks, using gyrokinetic simulations and theory, is presented. This work can be divided into three major parts. The first part studies particle transport in pure plasmas and investigates the origin and nature of flows against density gradients, also known as particle pinches. It is found that these pinches, which are primarily driven by temperature gradients, can also be responsible for the density peaking observed in experiments such as ASDEX-U, DIII-D or JET.

The second part of this work studies plasmas with multiple ion species. First, we study helium ash transport and its effects in the core of a reactor plasma, finding that a helium pinch driven by finite toroidicity can be created in some cases. Second, we study deuterium and tritium plasmas from the point of view of isotope flow separation, finding that in a $50-50$ deuterium-tritium plasma, a small fuel separation may occur.

Finally, the last part studies the behavior of energetic species in reactor plasmas. It is found that alpha particles interact strongly with the background turbulence. Perhaps the most surprising finding is that the fluxes per particle of alphas can be stronger than the fluxes per particle of deuterium (i.e. main ion), as opposed to "conventional wisdom" which assumes that species with large gyroradii do not significantly interact with the turbulence.

1

Introduction

Nuclear fusion is a type of reaction in which two isotopes of hydrogen fuse together to form an atom of helium. In the process, some of the hydrogen mass is converted into vast amounts of energy, making this reaction highly attractive as an energy source for the future. Compared to other major energy alternatives, it has the advantages of an abundant and easy to extract supply of cheap fuels, it is not based on chain reactions such as nuclear fission which makes it safer, and its radioactive waste is manageable. The least difficult fusion reaction to initiate on earth is the one between the hydrogen isotopes deuterium (D) and tritium (T)

$$\mathrm{D} + \mathrm{T} \rightarrow^4 \mathrm{He}\,(3.5\ \mathrm{MeV})\ + \mathrm{n}\,(14.1\ \mathrm{MeV})\ \ . \tag{1.1}$$

In the expression above He denotes helium and n denotes a neutron. To have an idea of the energy that can be released in this reaction, it is sufficient to say that a typical 1000 MW power plant consumes 2.7×10^9 kg of coal or 1.9×10^9 kg of oil in one year. Using fusion reactions the same plant would only require 100 kg of D and 150 kg of T. However, in order to achieve this, the D and T isotopes must be heated to temperatures on the order of 100 to 200 million C, and then make sure that the reaction can be self-sustained. This task is extremely complex from both scientific and technical points of view. At present there are two approaches to generate nuclear fusion: inertial and magnetic. In this work we focus on the second alternative. Simply put, in magnetic fusion D and T are heated by some external source and then transformed into a gas of charged particles (i.e. plasma) that can be “trapped” with magnetic fields. The resulting

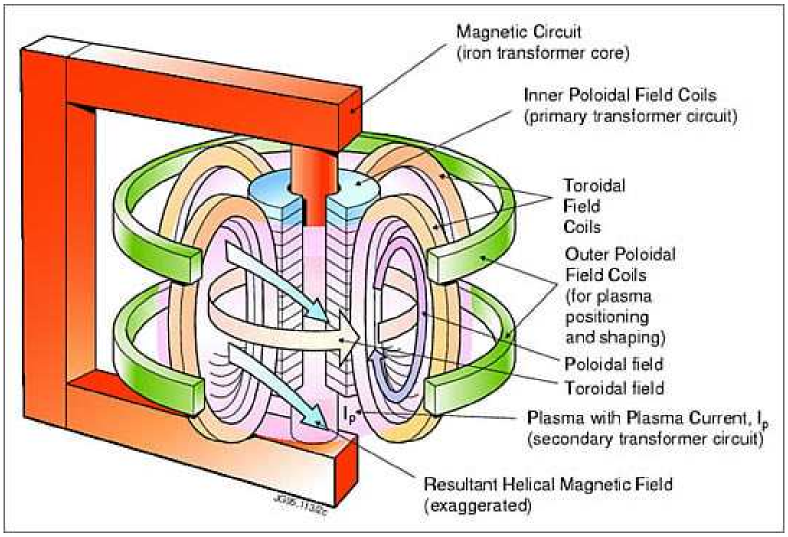
Magnetic Circuit
(iron transformer core)
Inner Poloidal Field Coils
(primary transformer circuit)
Toroidal
Field
Coils
Outer Poloidal
Field Coils
(for plasma
positioning
and shaping)
Poloidal field
Toroidal field
I_p
Plasma with Plasma Current, I_p
(secondary transformer circuit)
Resultant Helical Magnetic Field
(exaggerated)
JG05.113/2c

Figure 1.1 Schematic diagram of a tokamak. [Figure courtesy of EFDA-JET.]

plasma must be confined long enough in order to achieve the required temperatures and fusion of the fuel, such that the nuclear reactions can occur without external sources of energy (i.e. self-sustained reaction). However, if the confinement is excessive the spent fuel or "ash" will accumulate and quench the reactions.

The simplest way to confine a plasma using this method and achieve fusion is with a tokamak. Generally speaking, a tokamak is a doughnut-shaped or toroidal device, in which a poloidal magnetic field is created by a toroidal current, and a toroidal magnetic field is generated by a toroidal field coil system as shown in Fig. 1.1. In general, these fields can be manipulated and shaped to obtain the best magnetic topology that can confine the plasma, which remains in a vacuum chamber. Tokamak research is interdisciplinary by nature, although it is usually divided into different areas. For example, one of these areas is plasma equilibrium and stability, where the macroscopic equilibrium of the plasma and its response to perturbations is considered. Another research front is transport and confinement, which studies the energy and particle transport that arises from collisional and anomalous (i.e. non-classical) processes. Other areas include plasma heating, energetic particles physics, edge physics, plasma-surface interactions, etc.

1.1 The problem of transport

The research presented here addresses some of the open issues in the area of transport. However, before discussing our work it is useful to present a more detailed description of this problem. Transport is probably the most critical physics issue in magnetic fusion. It has a direct impact on the size of the tokamak and everything that this entails, such as cost or practicality. At the same time its intrinsic complexity has not allowed a complete understanding of the physics involved, making realistic predictions about the behavior of the plasma rather difficult. Although the classical mechanisms of transport are well understood [56] (and references therein), the anomalous ones which represent most of the observed transport are not. The main reason for this is that plasma turbulence is believed to be the main mechanism behind anomalous processes, which makes understanding transport equivalent to understanding plasma turbulence. The difficulties of turbulence in classical fluids are well known [44]. However, if we add several charged fluids coupled through an electromagnetic field, and boundary conditions that depend on the edge but can affect the core, the problem becomes even more difficult. Despite these intrinsic complications, a lot of theoretical and experimental progress has been made during the last decades [22] (and references therein).

Surprisingly enough, most transport studies, both computational and theoretical, have focused almost exclusively on the energy transport of core ions with little attention given to the study of plasma flow (i.e. particle transport). This is not a superfluous issue since ultimately these particles (e.g. D,T) are the ones responsible for the energy generation. This dissertation helps to bridge that gap by presenting a systematic study of particle transport in tokamaks via gyrokinetic simulations and theory. With regard to the approach, it is believed that the gyrokinetic equation coupled to Maxwell's equations lay a firm foundation of first-principle calculations of anomalous tokamak transport. Consequently, the numerical solution of this system can provide realistic and useful information about particle behavior in a tokamak. The methodology was to use highly realistic nonlinear simulations and complement them with theory and linear calculations. This approach allows us to understand the most important physics results provided by the simulations, without having to make the sacrifices that a purely analytical study or a simplified numerical model would require.

1.2 Historical background

One of the well known (and accepted) facts is that once a macroscopically stable equlibrium is reached in a reactor, the transport of energy and particles is determined by turbulence driven by microinstabilities [22, 58, 33]. These type of instabilities can be characterized by small scales on the order of the ion gyroradius, across magnetic field lines, and low frequencies compared to the ion cyclotron frequency. Among these instabilities the dominant ones are the so-called drift waves or drift-ballooning modes. Although there are different types of drift waves, they can be loosely classified in two main groups: ion temperature gradient (ITG) modes [30], which rotate in the ion direction, and trapped electron modes (TEM) [3, 72], which rotate in the opposite (electron) direction. It is important to mention that despite the differences between them, they all have the same source of free energy, which comes from density and temperature gradients present in the plasma. A somewhat recent review of these instabilities, including the different mechanisms of destabilization and their experimental observation, can be found in Ref. [58].

Using the typical scales that drift waves have, we can perform a straightforward dimensional analysis and get an estimate of the energy (χ) and particle (D) diffusivities by writing

$$\chi\,,\,D \sim \frac{L^2}{T} \sim \rho_s^2 \omega_* \ \ . \tag{1.2}$$

In the expression above, $\rho_s \doteq c_s/\Omega_{ci}$ is the ion gyroradius, where $c_s \doteq \sqrt{T_i/m_i}$ is the ion sound speed and $\Omega_{ci} \doteq z_i e B/m_i$ is the ion cyclotron frequency. The frequency ω_* is the diamagnetic drift frequency, defined to be $k_\theta \rho_s c_s/L_{ni}$, where k_θ is a poloidal mode number and $L_{ni} \doteq -[\partial(\ln n_i)/\partial r]^{-1}$ is the ion density scale length. If we take $k_\theta \rho_s \sim 1$ and $L_{ni} \sim a$ (a is the minor radius of the tokamak), we can write the above diffusivities in a useful form

$$\chi\,,\,D \sim \frac{\rho_s^2 c_s}{a} \ \ . \tag{1.3}$$

The above result is the gyroBohm diffusivity, which gives estimates that agree with the general size and ordering observed in different tokamak experiments, and also serves as a convenient normalization definition. This type of agreement supports the fact that microinstabilities and consequently "microturbulence" are responsible for the anomalous transport observed in many experiments. However, these estimates fail completely in predicting the variation of fluctuation levels and diffusivities with minor radius. For example, experiments show that the energy diffusivity χ increases with increasing the minor radius, while Eq. 1.3 predicts the opposite because of its $T_i^{3/2}$ dependence. Because of this, the losses predicted in a tokamak are too high in the core and too low in the edge compared to the experimental ones. Another problem is that going beyond these simple theoretical predictions is quite challenging. The combined difficulties of including more complicated dynamics (e.g. kinetic effects) and realistic geometry into an essentially nonlinear problem make this alternative close to intractable. Despite these intrinsic difficulties sophisticated analytic theories of plasma turbulence have been developed over the years. Although they have contributed a great deal to improve our basic understanding of transport, they are still based on heuristic reasoning, have simplified physics and do not offer practical applicability in most cases. An interesting review on the available analytic theories of plasma turbulence, limitations and perspectives can be found in Ref. [65].

One of the conclusions reached over the years is that, in order to provide a model of plasma transport with predictive capabilities, one must resort to numerical simulations. The issue then is to choose a model that offers the best balance between physical realism and computational affordability. Because of the latter, the models have changed dramatically over the years. These can be roughly classified in three groups: fluid, gyrofluid and kinetic. Fluid models are usually obtained by taking moments of more fundamental equations such as the Vlasov or Fokker-Planck equations. A similar approach is used by gyrofluid models in which the moments are taken from the gyrokinetic equation instead, which is a simplified version of the Vlasov equation. These moment procedures are followed by a series of approximations to close the system of equations (closure problem) to finally get a tractable problem. Kinetic models, on the other hand either solve the primitive equations directly or make slight approximations or reductions as in the case of gyrokinetic and drift kinetic equations [54]. In general, the simpler (less realistic) a model is, the easier to implement numerically, and viceversa.

1.2.1 Fluid models

Fluid models are the simplest to describe and implement. Once the velocity space moments are obtained from a given kinetic equation, the moment hierarchy is closed by assuming a highly collisional plasma. It is important to point out that although magnetohydrodynamics (MHD) models are fluid models, they cannot describe drift waves (or transport) because finite-Larmor-radius (FLR) terms are ignored in the MHD ordering. It turns out that these terms, which appear in the pressure tensor or heat flow are the ones responsible for the anomalous energy and particle flows observed in a plasma. Another consequence of the MHD ordering is that the typical scales and velocities are usually larger than the ion gyroradius and ion sound speed respectively. To properly describe drift waves, a two-fluid description such as the Braginskii model [15] is required.

Probably the first nonlinear model to capture low-frequency and short-wavelength dynamics was derived by Hasegawa and Mima [52], eventually becoming the standard model to study drift-wave turbulence. It consists of a one field description with adiabatic electrons and the nonlinearity arising from the convective derivative in the ion polarization drift. This model predicts an inverse cascade of total energy from small radial scales to large radial scales. One of its main limitations is the assumption of adiabatic electrons ($\delta n_{e,k} = e\phi_k/T_e$), which automatically excludes the density dynamcis and causes the model to miss important effects such as particle transport.

A latter model by Terry [99] improved the previous results by adding a nonadiabatic contribution to the electron response

$$\delta n_{e,k} = \frac{e\phi_k}{T_e}(1 - i\delta_k) \ , \tag{1.4}$$

where $\delta n_{e,k}$ is the perturbed electron density at a given wavenumber, e is the electron charge, ϕ_k is the electrostatic potential, T_e is the electron temperature and $i\delta_k$ is the nonadiabatic electron contribution. This modified Boltzmann density response, usually called the "$i\delta$ model", gives rise to a nonlinear $\mathbf{E}\times\mathbf{B}$ drift of nonadiabatic electrons not captured before. Here, $\mathbf{E}$ and $\mathbf{B}$ are the electric and magnetic fields respectively. This nonlinearity transfers energy from larger to smaller scales and dominates when $k_\theta \rho_s \ll 1$. For $k_\theta \rho_s \sim 1$ both nonlinearities must be taken into account, with the $\mathbf{E}\times\mathbf{B}$ nonlinearity blocking the "condensation" effects to larger scales.

The fluid approach, as a paradigm for core transport, reached its zenith during the eighties, which is evidenced on the vast number of publications produced in that decade [58]. Most of these were natural extensions of the models discussed above, and focused on either adding more physics effects (e.g. particle trapping, shear, curvature, etc.), or adapting them to different regimes (e.g. collisionless, dissipative, etc.). The main contribution of fluid models is that they produced clear qualitative understanding and predictions of the dynamics involved. Eventually, this approach was dropped and replaced by more sophisticated ones. We should mention that presently, most of the effort in fluid models has been directed to the study of the highly collisional plasma edge, where a fluid description is more suitable.

1.2.2 Gyrofluid models

The gyrofluid model takes velocity space moments from the gyrokinetic equation, and then closes the highest moment with a closure that can replicate kinetic effects. This closure approach, developed by Hammett and Perkins [51], provides an excellent model of linear Landau damping while preserving density, momentum and energy. Subsequent works [37, 50] extended the closure method to include nonlinear damping effects, although it was not perfect and had some limitations near marginal stability.

The model (and its closure) was developed first in slab geometry [37] and subsequently implemented in toroidal geometry using four moment equations with FLR terms and adiabatic electrons [107]. This latter work was succesfully benchmarked against linear gyrokinetic theory and eventually became the foundation of the transport model GLF23 [111]. Moreover, the first realistic nonlinear simulations using gyrofluid models in toroidal geometry were also based on that particular model [109]. A subsequent improvement used six moment equations [12], together with trapped ions and a model for trapped electron dynamics. The work that followed studied finite electromagnetic effects [94] with nonadiabatic passing electrons. More recently, a new linear model with 15 moment equations has been developed [95], which includes trapped and passing particles, general geometry, collisions and electromagnetic effects.

Gyrofluid simulations improved dramatically the understanding of plasma transport and turbulence. They confirmed the belief that the ITG mode plays the central role in driving microturbulence and the associated ion transport observed in the core of many tokamaks [12]. They also performed the first nonlinear simulations of TEM turbulence [12] and electromagnetic fluctuations [94]. Moreover, they show that nonlinear zonal flows, which are the $k_\theta = 0$ components of the $\mathbf{E}\times\mathbf{B}$ flow (θ is a poloidal angle), control the nonlinear saturation of transport [108, 109, 38, 14]. However, their inability to properly treat residual flows [90] motivated the eventual switch to gyrokinetic codes.

1.2.3 Kinetic models

Kinetic models solve more fundamental type of equations such as the six-dimensional Vlasov equation or the five-dimensional gyrokinetic equation. Although this approach is more desirable for the study of microinstabilities, due to their kinetic nature, it is considerably more problematic to handle. Issues such as the different temporal and spatial scales involved or its intrinsic size, make numerical simulations difficult to perform.

Kinetic simulations began with the early work of Cheng and Okuda [24], in which they studied dissipative trapped electron instabilities in a torus using particle simulations. The ion dynamics was described with a Vlasov equation, while the electron motion was approximated with a drift kinetic equation (gyroradius effects treated perturbatively).

Subsequent works focused their attention in the gyrokinetic model instead, since the problem was apparently simpler to handle (five dimensions instead of six). This approach will be discussed in more detail in the next section.

1.3 The gyrokinetic approach

The gyrokinetic equation is an approximation of Vlasov's equation in which the fast gyromotion of particles is averaged out, therefore reducing the number of dimensions of the problem. This is usually acomplished by performing a suitable expansion in a small parameter which leads to an ordering where equilibrium quantities are assumed to be slowly varying, while perturbations are smaller but rapidly varying.

From an historical point of view, gyrokinetics can be divided in two periods. During the first period all the theoretical machinery was created, beginning with the pioneering work of Rutherford and Frieman [92] and Taylor and Hastie [97], where the gyrokientic formalism was developed and the linear gyrokinetic equation was derived. Later work by Connor and Hastie[27] obtained a form for the electrostatic potential (ϕ), that satisfied both poloidal and toroidal periodicity constraints in axisymmetric geometries with finite magnetic shear (ballooning representation). An extension of this formalism was done by Antonsen and Lane [7] in which they added electromagnetic perturbations associated with shear and compressional Alfvén waves. The first work to include nonlinear effects into the gyrokinetic equation was performed by Frieman and Chen [43] via a multiple-scale expansion. As a result of this approach the so-called gyrokinetic ordering (see Ch.2 for more details) was introduced for the first time. Subsequent works improved this formalism by making the derivation procedure more rigorous [71, 40, 48], yielding as a result energy-conserving equations. However, they are seldom used in numerical simulations due to practical reasons.

The second period of gyrokinetics, which deals with the actual solution of the equations, began around the mid-eighties slightly overlapping the theoretical effort. The first numerical approach to the problem was via Lagrangian simulations. This technique, which is also called particle-in-cell (PIC), uses a moving grid that follows the guiding-center particles. The more particles, the better the Monte Carlo representation of the continuous equations. The advantage of PIC codes is that they are easier to implement, however they are susceptible to numerical noise due to their discrete nature. One of the first studies using this method was performed in slab geometry with electrostatic fluctuations and adiabatic electrons [67]. Subsequent works [68, 69] kept the same degree of realism but looked at other effects. Probably one of the major breakthroughs in Lagrangian codes was the creation of the δf method by Kotschenreuther [63], in which the equlibrium Maxwellian (and its noise) is removed from the simulation, leaving only the small departure (δf) from the equilibrium distribution. This method allowed more realistic simulations with toroidal geometry and bigger simulation domains. Codes developed after this were either flux-tube [34, 23] or global [81, 96, 70] and had different capabilities. Probably today, the most advanced PIC code is GEM [23] which has electron and ion dynamics, collisions and electromagnetic fluctuations.

The second numerical approach to gyrokinetic simulations is via Eulerian schemes.

These methods, which are sometimes called "continuum", use a fixed grid in the five-dimensional "gyrokinetic space". They are more complicated algorithmically than PIC codes, and therefore less abundant, although they provide a higher-quality solution and are noise-free. The first initial-value Eulerian solver was Kotschenreuther's GSTOTAL [64], which had trapped and passing particles with collisional and electromagnetic physics. An evolution of this solver was GKS, which added real geometry and other effects. These codes were the true forerunners to a robust, practical nonlinear gyrokinetic code. During the late nineties, Dorland extended GKS to include nonlinear dynamics [39]. The new code, called GS2, has become the most widely used microstability analysis code in the world fusion program. It includes kinetic dynamics for all species, collisions, electromagnetism, real geometry and compressional $\delta B_{\|}$ perturbations. Another nonlinear code developed around that time was GENE [61], which uses a three dimensional slab geometry with passing electrons. What is interesting about GENE despite its simplified physics, is that it was the first gyrokinetic solver to specifically address the problem of particle transport in a pure plasma [60], showing the existence of anomalous pinches (flow against gradients) from first principles equations. However, because of the simplified electron dynamics and geometry (no curvature), the magnitude and location of the pinch are substantially different from what is observed in experiments. More recently, GENE has been extended to include particle trapping [32] for the study of TEM turbulence. Finally, the most recent Eulerian effort is the GYRO code developed by Candy and Waltz [20, 19]. In addition to the physics capabilities that GS2 has, it includes $\mathbf{E}\times\mathbf{B}$ shear, global effects, experimental profiles, neoclassical transport, parallel nonlinearity, turbulent heating and coupled ITG-ETG dynamics.

One of the first major contributions from nonlinear gyrokinetic codes was the verification of the importance of Rosenbluth-Hinton [90] residual flows, as demonstrated by the flux-tube PIC code PG3EQ [34]. It was found that these flows give rise to an upshift in the nonlinear treshold for ITG turbulence with no electron dynamics (Dimits Shift). Another landmark contribution was the first comparison between a simulation (done with GS2) and an experiment [91]. Although the predicted levels were twice as high as the experimental ones, to do such a comparison fully kinetic species (ions, impurities and electrons) and pitch-angle scattering were required; a nontrivial task for the time. A more recent contribution from a gyrokinetic code comes from a highly realistic simulation of a DIII-D L-mode discharge done with GYRO [19]. The simulations included fully kinetic species, electromagnetism, shaped geometry, collisions and a global domain. The transport levels predicted by the code agree with the experimental values well within experimental uncertainty. This was the first demonstration of an operating code including all the relevant physics required to describe the core of a tokamak.

We believe that the arguments presented above justify the choice of gyrokinetics as a model to study particle transport in the core. For the simulations we use the GYRO code, with full nonlinear gyrokinetic dynamics of all ions, trapped and passing. Most of the work presented here uses the $\rho_* \to 0$ flux-tube (local) limit, where $\rho_* \doteq \rho_s/a$. In this limit, periodic boundary conditions and no profile variation are implied. This limit is entirely appropriate since finite-ρ_* corrections (global effects), which are weak in existing tokamaks, will be many times smaller in a reactor. In addition to this, we consider only electrostatic fluctuations, and assume unshifted circular geometry, but retain full kinetic electron dynamics. Specific details about the different simulations will be presented in the respective chapters.

1.4 Outline of the dissertation

1.4.1 Chapter 2: Theoretical background

The connection between the physical gyrokinetic equation and the one solved numerically by the codes is usually never made, even though it is not simple and require considerable work. In this chapter we introduce the gyrokinetic formalism, and make all the connections between the physical equations and the ones solved numerically. Various issues are discussed, including the flux-tube coordinate system and how each term in the gyrokinetic equation is transformed, the resulting Poisson equation and the gyroaverage operator. As an example, the case of the $s - \alpha$ equilibrium is discussed in detail.

1.4.2 Chapter 3: Particle transport in a pure plasma

Large tokamaks like DIII-D have very weak plasma flows as a consequence of almost negligible particle sources in the core. However, by looking at the observed peaked density profiles and based on diffusive arguments alone, one would expect the density gradients to drive a significant outward flow. This simple observation proves that other mechanisms can counteract, and in some cases dominate, diffusive processes in magnetically confined plasmas. This impasse is usually resolved by taking into account some inward flow or pinch to nearly cancel the outflow and yield the experimental levels. In other words, the total flow becomes the sum of an outward diffusive term and an inward convective term

$$\Gamma = -D\,\frac{\partial n}{\partial r} - n\,v_{\mathrm{in}} \quad . \tag{1.5}$$

In the expression above $D > 0$ is a diffusion coefficient, n is the density and v_{in} is an inward convective velocity. Unfortunately, putting this ansatz on a solid theoretical framework has proven to be a difficult problem, partly because the driving mechanisms are unclear. The neoclassical Ware pinch [112], which occurs as the result of toroidal electric fields, is too small to explain experimental observations, leaving turbulence as virtually the only candidate. A theoretical analysis of the problem is very difficult despite working with the pure plasma assumption. Here, the label pure refers to a plasma with electrons and a single ion species. The reason is the ambipolar flow condition (i.e. no net current flows), which requires electrons and ions to "flow together". Therefore, any simplification of the particle dynamics, such as adiabatic species, is simply out of the question if realistic results are expected. If on top of that we add a complicated geometry and particle trapping the problem becomes even worst.

The importance of pinches is not merely academic but practical as well, since they can cause density peaking, which in turn can improve the power production and energy confinement of the plasma. This chapter can be divided in two parts. The first one presents a computational study of anomalous particle pinches using local (flux-tube) simulations. Here we want to understand their dependence on critical parameters such as temperature gradients and collisions. The second part goes beyond the local assumption and makes connections between the pinch, which was studied locally, and density peaking, which is essentially a global problem. To perform the latter study we used global GYRO simulations of an L-mode DIII-D discharge, that will be described in the respective chapter. The text of this chapter, in full, includes material from "Gyrokinetic simulations of ion and impurity transport" [C. Estrada-Mila, J. Candy and R.E. Waltz, Phys. Plasmas **12**, 022305 (2005)] and "Density peaking and turbulent pinch in DIII-D discharges" [C. Estrada-Mila, J. Candy and R.E. Waltz, submitted to Phys. Plasmas (2006)]. The dissertation author was the primary researcher.

1.4.3 Chapter 4: Particle transport in impure plasmas

In this chapter we study the case of plasma flow in the presence of impurities (more than one ion species). Although this can be seen as a generalization of the previous chapter, its focus is different. Our main objective here is to determine how impurities behave and their effects on the main plasma. There are multiple critical issues in which impurities play a major role, such as in the design and operation of the fueling and pumping systems for burning plasmas. For example, the projected performance of the International Thermonuclear Experimental Reactor (ITER) depends strongly on the fraction of accumulated helium ash during long-pulse or steady-state operation [1]. Similarly, the accumulation of impurities (injected or originating from material surfaces) in the core of a burning plasma can result in excessive fuel dilution or core radiation.

The first part of the chapter studies the particle dynamics of helium ash and its effect on the energy confinement of the plasma. This impurity is simply a by-product of the fusion reactions and cannot be avoided or controlled. Moreover, any external pumping or removal of the ash can only be performed at the edge, leaving turbulence as the only possible mechanism of removal in the core (Ref. [102], and references therein). Consequently, one of the key issues is to determine if for typical experimental parameters the turbulence can perform this task. The second multispecies plasma we consider is one with deuterium and tritium. In particular, we would like to see how such a mixture behave and verify if the usual assumption of "almost-equal flows" is satisfied. The mechanics of this chapter is very similar to the previous one and studies how the transport depends on different parameters such as concentration, density gradients, collisions, etc. Although this problem is more difficult from a computational point of view, because more species are present, it is actually possible to do a theoretical analysis. The analysis, which is presented at the end of the chapter, can reproduce and explain the trends observed in the simulations. The reason again is ambipolarity, which only requires two species to yield particle flow. The remaining one (i.e. electrons) can then be assumed to have very simple dynamics or no dynamics at all (e.g. adiabatic response). The text includes partial material from "Gyrokinetic simulations of ion and impurity transport" [C. Estrada-Mila, J. Candy and R.E. Waltz, Phys. Plasmas **12**, 022305 (2005)]. The dissertation author was the primary researcher.

1.4.4 Chapter 5: Turbulent transport of alpha particles

This chapter presents a systematic study of the behavior of alpha particles (i.e. ^{4}He at 3.5 MeV) in reactor plasmas such as ITER. The chapter deviates somewhat from the previous two ones in the sense that the focus is not only on the particle transport, but also on the energy transport. Most research in this area has been devoted to the interaction between energetic ions, characterized by large gyroradius, and global MHD modes, paying little attention to the effects of turbulence. The "conventional wisdom" is that alpha particles "average" over the turbulence and do not interact with it, although this statement has never been verified directly.

Our purpose with this study is twofold. First, we want to know what is the interaction between microturbulence and large gyroradii particles; and second, if there are practical implications that can affect the performance of a reactor. To address these issues we use a combination of simulations and theory, which are explained in great detail in the chapter. The text of this chapter, in full, is taken from "Turbulent transport of alpha particles in reactor plasmas" [C. Estrada-Mila, J. Candy and R.E. Waltz, submitted to Nucl. Fusion (2006)]. The dissertation author was the primary researcher.

2

Theoretical Background

2.1 Introduction

This chapter introduces the physical gyrokinetic equation for ions and makes all the necessary connections with the equations solved numerically. Although this may seem a superflous step, there are some issues such as the coordinate system chosen and the particular geometry of the problem that need to be explained in detail.

2.2 Gyrokinetic ordering

As mentioned before, the gyrokinetic equation is an approximation of Vlasov's equation in which the fast gyromotion of particles is averaged out, therefore reducing the number of dimensions of the problem. This is usually acomplished by performing an expansion in a small parameter ρ_* [7, 43] which leads to an ordering where equilibrium quantities are assumed to be slowly varying, while perturbations are smaller but rapidly varying. In more detail we can write

$$\frac{e\delta\phi}{T_i} \sim \frac{\delta B}{B} \sim \frac{\delta f}{F} \sim \frac{k_\parallel}{k_\perp} \sim \frac{\rho_i}{a} \doteq \rho_* \ll 1 \ . \tag{2.1}$$

Here, the subscript i denotes ions, $\delta\phi$ and δB are the perturbed potential and magnetic field respectively, and δf is the perturbed distribution function (F is the equilibrium distribution). The ordering also gives information about the relative size of the gradient lengths for perturbed quantities $k_\parallel$ and $k_\perp$, as well as the Larmor radius of the ions ρ_i

with respect to the tokamak minor radius a. It is worth noticing that the perpendicular gradient lengths are taken to be comparable to the ion gyroradius ($k_\perp \rho_i \sim 1$). Finally, an extra assumption often used is that the frequency of field perturbations is small compared to the ion gyrofrequency ($\omega/\Omega_i \sim \epsilon$).

2.3 The ion gyrokinetic equation

Our derivation follows closely the presentation and notation of Ref. [57] for the electrostatic case. Notice that unless otherwise specified all quantities are physical (not normalized). The ion distribution f_s, where s is a species label, is written as a sum of an equilibrium part, F_{0s}, and fluctuating terms:

$$f_s(\mathbf{x}, \varepsilon, \mu, t) = F_{0s} - \frac{z_s e}{T_s} F_{0s} \left[\delta\phi(\mathbf{x}, t) - \overline{\delta\phi}(\mathbf{R}, t)\right] + h_s(\mathbf{R}, \varepsilon, \mu, t) \ . \tag{2.2}$$

Above, $\mathbf{x} = \mathbf{R} + \boldsymbol{\rho}$ is the particle position, $\mathbf{R}$ is the guiding-center position and $\boldsymbol{\rho} = \mathbf{b} \times \mathbf{v}/\Omega_{\mathrm{cs}}$ is the gyroradius vector, where $\mathbf{b} \doteq \mathbf{B}/B$ is the unitary magnetic field vector, $\mathbf{v}$ is the velocity vector and $\Omega_{\mathrm{cs}} = z_s e B/m_s$. The energy is $\varepsilon \doteq v^2/2 + (z_s e/m_s)\Phi_0(\mathbf{x})$, where $\Phi_0(\mathbf{x})$ is the equlibrium potential, and the magnetic moment is $\mu \doteq v_\perp^2/(2B)$, where $v_\perp$ is the velocity perpendicular to the magnetic field and B is the magnitude of said field. Bars denote gyroaverages, which can be defined formally as

$$\overline{z}(\mathbf{R}, t) \doteq \oint \frac{da}{2\pi}\, z(\mathbf{R} + \boldsymbol{\rho}, t) \ , \tag{2.3}$$

for any function, z. The equilibrium is assumed to be a Maxwellian

$$F_{0s}(\mathbf{R}, \varepsilon) \doteq \frac{n_{0s}(\mathbf{R})}{(2\pi T_s/m_s)^{3/2}} e^{-m_s v^2/2T_s} \ . \tag{2.4}$$

The gyrokinetic equation for h_s is

$$\frac{\partial h_s}{\partial t} + (v_\parallel \mathbf{b} + \mathbf{v}_{\mathrm{d}}) \cdot \nabla \left(h_s + \frac{z_s e}{T_s} F_0\, \overline{\delta\phi} \right) + \mathbf{v}_{\mathrm{E}} \cdot \nabla \left(F_{0s} + h_s\right) = C(h_s) \ , \tag{2.5}$$

where the drift velocities are

$$\mathbf{v}_{\mathrm{d}} \doteq \frac{v_\parallel^2 + \mu B}{\Omega_{\mathrm{cs}} B} \mathbf{b} \times \nabla B + \frac{4\pi v_\parallel^2}{\Omega_{\mathrm{cs}} B^2} \mathbf{b} \times \nabla p \quad \text{and} \quad \mathbf{v}_{\mathrm{E}} \doteq \frac{1}{B} \mathbf{b} \times \nabla \overline{\delta\phi} \ . \tag{2.6}$$

In the equations above, $v_\parallel$ is the velocity parallel to the magnetic field and ∇p is the pressure gradient. Also, in Eq. 2.5, we did not include the equilibrium or background $\mathbf{E}\times\mathbf{B}$ drift ($\mathbf{v}_{\mathrm{E0}} = \mathbf{b}\times\nabla\Phi_0/B$) since none of our simulations has it, although its treatment is almost identical to $\mathbf{v}_{\mathrm{E}}$.

2.4 Field-aligned coordinates

The gyrokinetic equation introduced previously is general and does not specify a particular set of coordinates. Therefore, any precise information about quantities such as the equlibrium magnetic field or the space gradients is not known beforehand. Moreover, in order to construct a solution we need to decide which geometry is the most appropiate. In principle one could think about solving the problem in a full tokamak, although such simulation will be beyond presently available computational resources, if all the relevant scales are to be resolved properly. However, there are two advantages which could make unnecessary to simulate a whole torus. The first one is that the turbulence we want to solve is locally driven and characterized by small scales (microturbulence). The second advantage is that this type of turbulence evolves from instabilities characterized by short perpendicular and long parallel wavelengths ($k_\perp \gg k_\parallel$). For instance, a coordinate system that exploits this anisotropy while resolving a much smaller volume compared to a full torus is the so-called field-aligned coordinate system [13] or flux tube geometry. In this system the coordinates follow field lines and the volume in question is a flux tube (a tube with a surface parallel to $\mathbf{B}$) that is bent by curvature and twisted by magnetic shear, allowing a mapping into a simple rectangular domain. An extra advantage of these coordinates besides the computational efficiency is that the required periodicty can be enforced easily.

To introduce this system we first notice that if we want to follow the magnetic field it is natural to use coordinates that are constant on field lines. A useful way to describe any magnetic field is by using the Clebsch representation [66] which is given by

$$\mathbf{B} = \nabla\alpha \times \nabla\psi \quad \text{such that} \quad \mathbf{B}\cdot\nabla\alpha = \mathbf{B}\cdot\nabla\psi = 0 \ . \tag{2.7}$$

Consequently, α and ψ, which are scalar functions of position can be used as coordinates. The third choice, θ, will represent distance along the flux tube. In these coordinates, the associated Jacobian is $\mathcal{J} \doteq (\nabla\alpha \times \nabla\psi \cdot \nabla\theta)^{-1}$ and the poloidal flux is $\psi \doteq (2\pi)^{-1}\int \mathbf{B}\cdot\nabla\theta d\tau$, where $d\tau$ refers to a volume element. The choice for α has to be done in such a way that periodicity requirements are satisfied. We can write in general

$$\alpha \doteq \varphi - \nu(\psi, \theta) \ , \tag{2.8}$$

subject to $\nu(\psi, 2\pi) = 2\pi q(\psi)$ and $\nu(\psi, 0) = 0$. With this definition the magnetic field becomes

$$\mathbf{B} = \nabla\alpha \times \nabla\psi = \nabla\varphi \times \nabla\psi - \frac{\partial\nu}{\partial\theta}\nabla\theta \times \nabla\psi = \nabla\varphi \times \nabla\psi - f(\psi)\nabla\varphi \ . \tag{2.9}$$

In order to determine the general form $\nu(\psi, \theta)$ we take the $\mathbf{B} \cdot \nabla\varphi$ product and integrate to find

$$\nu(\psi, \theta) = -f(\psi) \int_0^\theta \mathcal{J} \left|\nabla\varphi\right|^2 d\theta \ . \tag{2.10}$$

As we can see, the choice of $\nu(\psi, \theta)$ is highly dependent on the geometry of the problem. For example, in the case of concentric (unshifted) circular flux surfaces $\nu(\psi, \theta)$ reduces to the more familiar form $\nu(\psi, \theta) = q(\psi)\theta$, where $q(\psi)$ is the safety factor and satisfies $q(\psi) = \mathbf{B} \cdot \nabla\varphi / \mathbf{B} \cdot \nabla\theta$. The two variables φ and θ are the physical angles in the toroidal and poloidal directions. The periodicity requirements in this case can be seen by considering the following representation for functions

$$z(\psi, \theta, \alpha) = \sum_j z_n(\psi, \theta)\, e^{-in\alpha} \quad \text{with} \quad n = j\Delta n \ . \tag{2.11}$$

We impose the following topological requirements on the real quantity z:

1. z is $2\pi/\Delta n$-periodic in φ for fixed ψ and θ,

2. z is 2π-periodic in θ for fixed ψ and φ.

In particular, condition 2 implies that the (complex) expansion coefficients satisfy

$$z_n(\psi, -\pi) = e^{2\pi i n q(\psi)} z_n(\psi, \pi) \ . \tag{2.12}$$

The final constraint we introduce is related to the radial periodicity of the expansion coefficients and can be expressed as

$$z_n(\psi, \theta) = z_n(\psi + L, \theta) \ . \tag{2.13}$$

2.5 The ion gyrokinetic equation in flux tube geometry

The gyrokinetic equation introduced previously (Eq. 2.5) can be written in this coordinate system. We begin by considering first the parallel motion contribution which becomes

$$v_{\parallel}\mathbf{b}\cdot\nabla\left(h_s+\frac{z_s e}{T_s}F_{0s}\,\overline{\delta\phi}\right)=\frac{v_{\parallel}}{\mathcal{J}B}\frac{\partial}{\partial\theta}\left(h_s+\frac{z_s e}{T_s}F_{0s}\,\overline{\delta\phi}\right)\quad . \tag{2.14}$$

We now proceed with the drift terms that include the ∇B and curvature contributions. These are given by the third term on the LHS of Eq. 2.5

$$\begin{aligned}\mathbf{v}_{\mathrm{d}}\cdot\nabla\left(h_s+\frac{z_s e}{T_s}F_{0s}\,\overline{\delta\phi}\right)&=\frac{v_{\parallel}^2+\mu B}{\Omega_{\mathrm{cs}}B^2}\mathbf{B}\times\nabla B\cdot\nabla\left(h_s+\frac{z_s e}{T_s}F_{0s}\,\overline{\delta\phi}\right)\\&+\frac{4\pi v_{\parallel}^2}{\Omega_{\mathrm{cs}}B^3}\mathbf{B}\times\nabla p\cdot\nabla\left(h_s+\frac{z_s e}{T_s}F_{0s}\,\overline{\delta\phi}\right)\quad .\end{aligned} \tag{2.15}$$

The first thing we need to do is find an expression for $\mathbf{B}\times\nabla B\cdot\nabla$. Using the Clebsch representation for $\mathbf{B}$ (Eq. 2.7) we find

$$\begin{aligned}\mathbf{B}\times\nabla B\cdot\nabla\sim B^2\left(\frac{\partial B}{\partial\alpha}\frac{\partial}{\partial\psi}-\frac{\partial B}{\partial\psi}\frac{\partial}{\partial\alpha}\right)+\mathbf{B}\cdot\left(\nabla\theta\times\nabla\alpha\right)\frac{\partial B}{\partial\theta}\frac{\partial}{\partial\alpha}\\-\mathbf{B}\cdot\left(\nabla\psi\times\nabla\theta\right)\frac{\partial B}{\partial\theta}\frac{\partial}{\partial\psi}\quad .\end{aligned} \tag{2.16}$$

Using the same approach and noting that $p=p(\psi)$, we can also compute $\mathbf{B}\times\nabla p\cdot\nabla$ which yields

$$\mathbf{B}\times\nabla p\cdot\nabla\sim -B^2\frac{\partial p}{\partial\psi}\frac{\partial}{\partial\alpha}\quad . \tag{2.17}$$

In the previous two equations we used certain approximations consistent with the gyrokinetic ordering; namely, $\partial/\partial\psi\sim O(1)$, $\partial/\partial\alpha\sim O(1)$ and $\partial/\partial\theta\sim O(\rho_*)$ for the fluctuating quantities h_s and $\overline{\delta\phi}$. Using the resulting expressions the drift terms become:

$$\begin{aligned}\mathbf{v}_{\mathrm{d}}\cdot\nabla\left(h_s+\frac{z_s e}{T_s}F_{0s}\,\overline{\delta\phi}\right)\sim\Bigg\{&\frac{v_{\parallel}^2+\mu B}{\Omega_{\mathrm{cs}}B^2}\left[B^2\left(\frac{\partial B}{\partial\alpha}\frac{\partial}{\partial\psi}-\frac{\partial B}{\partial\psi}\frac{\partial}{\partial\alpha}\right)\right.\\&+\ \mathbf{B}\cdot\left(\nabla\theta\times\nabla\alpha\right)\frac{\partial B}{\partial\theta}\frac{\partial}{\partial\alpha}\\&\left.-\ \mathbf{B}\cdot\left(\nabla\psi\times\nabla\theta\right)\frac{\partial B}{\partial\theta}\frac{\partial}{\partial\psi}\right]\\&-\ \frac{4\pi v_{\parallel}^2}{\Omega_{\mathrm{cs}}B^3}\left[B^2\frac{\partial p}{\partial\psi}\frac{\partial}{\partial\alpha}\right]\Bigg\}\left(h_s+\frac{z_s e}{T_s}F_{0s}\,\overline{\delta\phi}\right)\quad .\end{aligned} \tag{2.18}$$

Next, we evaluate the fluctuating or generalized **E**×**B** contribution given by the last two terms on the LHS of Eq. 2.5. Using the same approach as for the drift contribution we get

$$\mathbf{v}_\mathrm{E}\cdot\nabla F_{0s} = \frac{\mathbf{B}\times\nabla\overline{\delta\phi}}{B^2}\cdot\nabla F_{0s} \sim \frac{\partial F_{0s}}{\partial\psi}\frac{\partial\overline{\delta\phi}}{\partial\alpha}\ , \tag{2.19}$$

$$\mathbf{v}_\mathrm{E}\cdot\nabla h_s = \frac{\mathbf{B}\times\nabla\overline{\delta\phi}}{B^2}\cdot\nabla h_s \sim \frac{\partial h_s}{\partial\psi}\frac{\partial\overline{\delta\phi}}{\partial\alpha} - \frac{\partial h_s}{\partial\alpha}\frac{\partial\overline{\delta\phi}}{\partial\psi}\ , \tag{2.20}$$

where the RHS of Eq. 2.20 has a Poisson bracket structure and can also be written using its short-hand notation $\left\{\overline{\delta\phi}, h_s\right\}$. The linear part of the $\mathbf{E}\times\mathbf{B}$ motion leaves a residual connected with the energy-dependent part of

$$\frac{1}{F_{0s}}\frac{\partial F_{0s}}{\partial\psi} = \frac{1}{n_{0s}}\frac{\partial n_{0s}}{\partial\psi} + \frac{1}{T_s}\frac{\partial T_s}{\partial\psi}\left(\frac{m_s v^2}{2T_s} - \frac{3}{2}\right)\ . \tag{2.21}$$

By putting all these contributions together (Eqs. 2.14,2.18,2.19,2.20 and 2.21) into Eq. 2.5 we can get an expression for the ion gyrokinetic equation in flux-tube geometry given by

$$\begin{aligned}\frac{\partial h_s}{\partial t} &+ \left\{\frac{v_\parallel}{\mathcal{J}B}\frac{\partial}{\partial\theta} + \frac{v_\parallel^2+\mu B}{\Omega_\mathrm{cs}B^2}\left[B^2\left(\frac{\partial B}{\partial\alpha}\frac{\partial}{\partial\psi} - \frac{\partial B}{\partial\psi}\frac{\partial}{\partial\alpha}\right) + \mathbf{B}\cdot(\nabla\theta\times\nabla\alpha)\frac{\partial B}{\partial\theta}\frac{\partial}{\partial\alpha}\right.\right.\\ &- \left.\left.\mathbf{B}\cdot(\nabla\psi\times\nabla\theta)\frac{\partial B}{\partial\theta}\frac{\partial}{\partial\psi}\right] - \frac{4\pi v_\parallel^2}{\Omega_\mathrm{cs}B^3}\left[B^2\frac{\partial p}{\partial\psi}\frac{\partial}{\partial\alpha}\right]\right\}\left(h_s + \frac{z_s e}{T_s}F_{0s}\overline{\delta\phi}\right)\\ &+ F_{0s}\left[\frac{1}{n_{0s}}\frac{\partial n_{0s}}{\partial\psi} + \frac{1}{T_s}\frac{\partial T_s}{\partial\psi}\left(\frac{m_s v^2}{2T_s} - \frac{3}{2}\right)\right]\frac{\partial\overline{\delta\phi}}{\partial\alpha} + \left\{\overline{\delta\phi}, h_s\right\} = C(h_s)\ .\end{aligned} \tag{2.22}$$

For the next step we expand the perturbed quantities $(h_s, \overline{\delta\phi})$ as Fourier series in α. Recalling Eq. 2.11 we can write for example, h_s as

$$h_s(\psi,\theta,\alpha) = \sum_j h_{sn}(\psi,\theta)\, e^{-in\alpha}\ . \tag{2.23}$$

The required derivatives are

$$\frac{\partial h_s}{\partial\psi} = \sum_j \frac{\partial h_{sn}}{\partial\psi}\, e^{-in\alpha}\ , \tag{2.24}$$

$$\frac{\partial h_s}{\partial\theta} = \sum_j \frac{\partial h_{sn}}{\partial\theta}\, e^{-in\alpha}\ , \tag{2.25}$$

$$\frac{\partial h_s}{\partial\alpha} = \sum_j (-inh_{sn})\, e^{-in\alpha}\ . \tag{2.26}$$

Now, we can write the gyrokinetic equation for a single toroidal harmonic using the above relations, and noting that $\mathbf{B} = \mathbf{B}(\psi, \theta)$ we find

$$\begin{aligned} \frac{\partial h_{sn}}{\partial t} &+ \left[\frac{v_\parallel}{\mathcal{J}B}\frac{\partial}{\partial\theta} - i\omega_{ds}^{(1)} - i\omega_{ds}^{(r)}\frac{\partial}{\partial\psi}\right]\left(h_{sn} + \frac{z_s e}{T_s}F_{0s}\,\overline{\delta\phi}_n\right) - iF_{0s}\omega_{*s}\overline{\delta\phi}_n \\ &+ \left\{\overline{\delta\phi}, h_s\right\}_n = C(h_{sn}) \ . \end{aligned} \tag{2.27}$$

Above, the curvature drift coefficients, $\omega_{ds}^{(1)}$ and $\omega_{ds}^{(r)}$ can be written as

$$\omega_{ds}^{(1)} \doteq -\,n\,\frac{v_\parallel^2 + \mu B}{\Omega_{\mathrm{cs}}B^2}\left[B^2\frac{\partial B}{\partial\psi} - \mathbf{B}\cdot(\nabla\theta\times\nabla\alpha)\,\frac{\partial B}{\partial\theta}\right] - n\,\frac{4\pi v_\parallel^2}{\Omega_{\mathrm{cs}}B}\,\frac{\partial p}{\partial\psi} \ , \tag{2.28}$$

$$\omega_{ds}^{(r)} \doteq -\,i\,\frac{v_\parallel^2 + \mu B}{\Omega_{\mathrm{cs}}B^2}\,\mathbf{B}\cdot(\nabla\psi\times\nabla\theta)\,\frac{\partial B}{\partial\theta} \ , \tag{2.29}$$

whereas the diamagetic frequency ω_{*s} is given by

$$\omega_{*s} \doteq n\,\left[\frac{1}{n_{0s}}\frac{\partial n_{0s}}{\partial\psi} + \frac{1}{T_s}\frac{\partial T_s}{\partial\psi}\left(\frac{m_s v^2}{2T_s} - \frac{3}{2}\right)\right] \ . \tag{2.30}$$

This is the final form of the ion gyrokinetic equation in the desired coordinates. The equation is general in the sense that it is independent of the particular equilibrium used.

2.6 The Poisson equation

For a multi-species plasma the Poisson (quasineutrality) equation can be written as

$$\delta n_e = \sum_s z_s \delta n_s \ , \tag{2.31}$$

where

$$\sum_s z_s \delta n_s = \sum_s z_s \int d^3v\,\delta f_s \ , \tag{2.32}$$

and

$$\delta f_s = -\frac{e z_s}{T_s}F_{0s}\left[\delta\phi(\mathbf{x},t) - \overline{\delta\phi}(\mathbf{R},t)\right] + h_s(\mathbf{R},\varepsilon,\mu,t) \ . \tag{2.33}$$

After some manipulations, we can write the quasineutrality equation in a more compact form

$$\sum_s^{n_{ion}} n_{0s}\frac{e z_s^2}{T_s}\left[\delta\phi(\mathbf{x},t) - \overline{\overline{\delta\phi}}(\mathbf{x},t)\right] = \sum_s^{n_{ion}} z_s\delta N_s(\mathbf{x},t) - \delta n_e(\mathbf{x},t) \ , \tag{2.34}$$

where n_{ion} refers to the total number of ions, and the double gyroaveraged potential is given by

$$\overline{\overline{\delta\phi}}(\mathbf{x},t) = \frac{1}{n_{0s}} \int d^3v\, F_{0s}\, \overline{\delta\phi}(\mathbf{x}-\boldsymbol{\rho},t) \ \ , \tag{2.35}$$

and

$$\delta N_s(\mathbf{x},t) = \int d^3v\, h_s(\mathbf{x}-\boldsymbol{\rho},\varepsilon,\mu,t) \ \ . \tag{2.36}$$

The electron gyroradius contributions are neglected, which is an acceptable approximation for $k_\theta \rho_s \leq 5$, where $k_\theta \doteq nq/r$. It is important to realize that all the physics of interest (ITG/TEM) are well within this range and therefore such simplification is justified. This statement has been verified a posteriori multiple times, where it is always found that for $k_\theta \rho_s > 2$ the contribution to the total transport is negligible. With this approximation we can write

$$\delta n_e(\mathbf{x},t) = \int d^3v\, \delta f_e \sim \int d^3v\, h_e(\mathbf{x}-\boldsymbol{\rho},\varepsilon,\mu,t) = \delta N_e(\mathbf{x},t) \ \ . \tag{2.37}$$

Finally, the Poisson equation becomes

$$\sum_s^{n_{ion}} n_{0s} \frac{e z_s^2}{T_s} \left[\delta\phi(\mathbf{x},t) - \overline{\overline{\delta\phi}}(\mathbf{x},t)\right] = \sum_s^{n_{kinetic}} z_s \delta N_s(\mathbf{x},t) \ \ , \tag{2.38}$$

where $n_{kinetic}$ refers to ions and electrons.

2.7 The gyroaverage operator

As it was the case with the previous equations we need to derive a more precise expression for the gyroaverage operator. Recalling Eq. 2.27 we can write the gyroaveraged potential as

$$\overline{\delta\phi}(\mathbf{R},t) \doteq \oint \frac{da}{2\pi}\, \delta\phi(\mathbf{R}+\boldsymbol{\rho},t) \ \ , \tag{2.39}$$

or equivalently

$$\overline{\delta\phi}(\mathbf{R},t) \doteq \oint \frac{da}{2\pi} \sum_j \delta\phi_n(\psi'(a),\theta'(a)) e^{-in\alpha'(a)} \ \ , \tag{2.40}$$

where the primed coordinates are evaluated along a gyro-orbit. The equivalence of the previous two forms can be easy established since the representation $\delta\phi(\mathbf{R}+\boldsymbol{\rho},t)$ denotes a potential over said gyro-orbit.

In order to describe quantities over each of such orbits we need two mutually perpendicular unit vectors given by

$$\hat{\psi} = \frac{\nabla\psi}{|\nabla\psi|} \quad \text{and} \quad \hat{e} = \mathbf{b} \times \hat{\psi} \ . \tag{2.41}$$

With these vectors, the perpendicular Larmor radius can be written as

$$\boldsymbol{\rho}_\perp = \frac{\mathbf{v}_\perp}{\Omega_{cs}} = \frac{v_\perp}{\Omega_{cs}} \left(\hat{\psi} \cos a + \hat{e} \sin a \right) \ . \tag{2.42}$$

The next step consists in relating the primed variables with the non-primed ones. The a-variation of θ' in the integrand is dominated by the rapidly-varying exponential, and according to the gyrokinetic ordering it is valid to set $\theta'(a) = \theta$ in $\delta\phi_n$. For ψ', we can write exactly

$$\psi' = \psi + \boldsymbol{\rho}_\perp \cdot \nabla\psi = \psi + \frac{v_\perp}{\Omega_{cs}} \cos a |\nabla\psi| \ , \tag{2.43}$$

and for α' we use the small gyro-orbit excursion (small α') approximation

$$\alpha' = \alpha + \boldsymbol{\rho}_\perp \cdot \nabla\alpha + \ldots \sim \alpha + \frac{v_\perp}{\Omega_{cs}} \left(\hat{\psi} \cdot \nabla\alpha \cos a + \hat{e} \cdot \nabla\alpha \sin a \right) \ . \tag{2.44}$$

The gyroaveraged potential for a single harmonic then becomes

$$\overline{\delta\phi}_n = \oint \frac{da}{2\pi} \, \delta\phi_n \left(\psi + \boldsymbol{\rho}_\perp |\nabla\psi| \cos a, \theta \right) e^{-i\rho_\perp (\zeta_x \cos a + \zeta_y \sin a)} \ , \tag{2.45}$$

where

$$\zeta_x \doteq n \frac{\nabla\psi \cdot \nabla\alpha}{|\nabla\psi|} \quad \text{and} \quad \zeta_y \doteq -n \frac{B}{|\nabla\psi|} \ . \tag{2.46}$$

2.8 Example: The $s - \alpha$ equilibrium

In order to further illustrate the connection between the previous equation and more intuitive physical quantities, it is useful to consider a simple case in which the geometry is simple enough to allow explicit equilibrium quantities such as the magnetic field. Because of this, we choose the $s - \alpha$ model [28] characterized by shifted circular flux surfaces and large aspect ratio ($a/R_0 \ll 1$). Another reason is to illustrate the connection between the pressure gradient and the Shafranov shift from the standpoint of the gyrokinetic formalism. Using Shafranov coordinates we can express this particular geometry as

$$R = R_0 + r\cos\theta - \Delta(r) \ , \tag{2.47}$$

$$\xi = \ -\varphi \ , \tag{2.48}$$

$$Z = r\sin\theta \ . \tag{2.49}$$

where Z is the usual cartesian coordinate. The connection with x and y is given by $x = R\cos\xi$ and $y = R\sin\xi$. The remaining quantities are as follows: R_0 denotes the major radius, ϕ a toroidal angle, θ its poloidal counterpart and $\Delta(r)$ is the Shafranov shift. To determine the structure of **B** we need to find a suitable expression for α. The first step consists in determing the value of $\nu(\psi, \theta)$ which, recalling Eq. 2.10, is given by

$$\nu(\psi, \theta) = -f(\psi)\int_0^\theta \mathcal{J}\left|\nabla\varphi\right|^2 d\theta \ . \tag{2.50}$$

From Appendix B we know that the Jacobian in (ψ, θ, φ) coordinates can be written as $\mathcal{J} = rR(1 - \Delta'(r)\cos\theta)/\psi'$, where the prime denotes a derivative with respect to r, and also that $\left|\nabla\varphi\right|^2 = 1/R^2$. After expanding the integrand through orders $\mathcal{O}(\epsilon)$, where $\epsilon \doteq r/R_0$, and $\mathcal{O}(\Delta/R_0)$ we find

$$\nu(\psi, \theta) \sim -\frac{rf(\psi)}{R_0\psi'}\left[\left(1 + \frac{\Delta}{R_0}\right)\theta - \left(\frac{r}{R_0} + \Delta'\right)\sin\theta\right] + \mathcal{O}(\epsilon^3) \ . \tag{2.51}$$

By applying the condition $\nu(\psi, 2\pi) = 2\pi q(\psi)$ we can determine the safety factor which is given by

$$q(\psi) = -\frac{rf(\psi)}{R_0\psi'}\left(1 + \frac{\Delta}{R_0}\right) \sim -\frac{rf(\psi)}{R_0\psi'} + \mathcal{O}(\epsilon^2) \ . \tag{2.52}$$

Using this result we can write an expression for the coordinate α in this particular geometry

$$\alpha \sim \varphi - q\theta + q\sin\theta\left(\frac{r}{R_0} + \Delta'(r)\right) + \mathcal{O}(\epsilon^2) \ . \tag{2.53}$$

Going back to Eq. 2.27 we are now in capacity to write a more explicit form of the gyrokinetic equation. In particular, we can compute $in\mathbf{B}\cdot(\nabla\theta\times\nabla\alpha)\,(\partial B/\partial\theta)$, $\mathbf{B}\cdot(\nabla\psi\times\nabla\theta)\,(\partial B/\partial\theta)(\partial/\partial\psi)$ and $inB^2(\partial B/\partial\psi)$. The first expression we need to determine is the magnitude of the magnetic field, which can be found in Appendix B and is given by

$$\frac{B}{B_0} \sim 1 - \frac{r}{R_0}\cos\theta + \mathcal{O}(\epsilon^2) \ . \tag{2.54}$$

Notice that this magnitude is the same one for the case of zero β (unshifted) large-aspect-ratio toroidal equilibrium [47]. The same occurs with the poloidal flux which is given by $\psi \sim \int (B_0 r/q(\psi))dr$. With this information, the quantities $inB^2(\partial B/\partial\psi)$ and $in(\partial p/\partial\psi)$ are straightforward to calculate and can be written as

$$inB^2\frac{\partial B}{\partial\psi} \sim -\frac{ik_\theta B_0^2}{R_0}\cos\theta \quad \text{and} \quad in\frac{\partial p}{\partial\psi} \sim \frac{ik_\theta}{B_0}\frac{\partial p}{\partial r} \ , \tag{2.55}$$

where

$$k_\theta \doteq \frac{nq}{r} \ . \tag{2.56}$$

To determine the remaining quantities from the gyrokinetic equation we first need to compute the following terms

$$\mathbf{B}\cdot(\nabla\theta\times\nabla\alpha) = (\nabla\alpha\cdot\nabla\theta)(\nabla\psi\cdot\nabla\alpha) - |\nabla\alpha|^2(\nabla\psi\cdot\nabla\theta) \ , \tag{2.57}$$

$$\mathbf{B}\cdot(\nabla\psi\times\nabla\theta) = (\nabla\alpha\cdot\nabla\psi)(\nabla\psi\cdot\nabla\theta) - |\nabla\psi|^2(\nabla\alpha\cdot\nabla\theta) \ . \tag{2.58}$$

In the above expressions we need to specify $\nabla\alpha$ in order to go further. Using the expression derived in Eq. 2.53 we can write

$$\nabla\alpha = \nabla\varphi + a\nabla\theta + b\nabla\psi \ , \tag{2.59}$$

where a and b are given by

$$a = -q\left(1 - \left(\frac{r}{R_0} + \Delta'\right)\cos\theta\right) \ , \tag{2.60}$$

$$b = -\frac{q}{B_0 r}\left[\frac{q}{r}s\left(\theta - \left(\frac{r}{R_0} + \Delta'\right)\sin\theta\right) - \frac{q}{R_0}\sin\theta\,(1 + R_0\Delta'')\right] \ . \tag{2.61}$$

In the expression above the primes denote derivatives with respect to r and the magnetic shear is defined as $s \doteq (r/q)q'$. Now, if we replace Eq. 2.61 into Eqs. 2.57 and 2.58, and use the appropiate identities from Appendix B we get

$$-in\mathbf{B}\cdot(\nabla\theta\times\nabla\alpha)\frac{\partial B}{\partial\theta} \sim -\frac{ik_\theta B_0^2}{R_0}\sin\theta\,[s\theta - \alpha_{\mathrm{GK}}\sin\theta] \ , \tag{2.62}$$

$$-\mathbf{B}\cdot(\nabla\psi\times\nabla\theta)\frac{\partial B}{\partial\theta}\frac{\partial}{\partial\psi} \sim -\frac{B_0^2}{R_0}\sin\theta\frac{\partial}{\partial r} \ , \tag{2.63}$$

where α_{GK} is given by

$$\alpha_{\mathrm{GK}} = r\Delta'' + s\left(\frac{r}{R_0} + \Delta'\right) \ . \tag{2.64}$$

Before going further it is important to discuss this last term. We decided to call it α_{GK} since it can be related to the pressure gradient in the same fashion as the well known α_{MHD} term that arises in MHD theory. By definition this term is given by

$$\alpha_{\mathrm{MHD}} \doteq -q^2 R_0 \frac{\partial \beta}{\partial r} \ , \tag{2.65}$$

where $\beta \doteq 8\pi p/B_0^2$ and $(d\beta/dr) < 0$ is implied [114]. In order to make a connection between α_{GK} and α_{MHD}, we need to relate Δ'' and Δ' with the pressure gradient. This can be achieved by using the Grad-Shafranov equation for this particular equilibrium. For instance, using the same equation as in Ref. [76] we can write

$$\frac{\partial}{\partial r}\left[r\left(\frac{\partial \psi}{\partial r}\right)^2 \Delta'\right] = 8\pi r^2 R_0 \frac{\partial p}{\partial r} - \frac{r}{R_0}\left(\frac{\partial \psi}{\partial r}\right)^2 \ . \tag{2.66}$$

By combining the above equation with the poloidal flux, $\psi \sim \int (B_0 r/q(\psi))dr$, and the definition of β, we can write $r\Delta''$ as

$$r\Delta'' = -q^2 R_0 \frac{\partial \beta}{\partial r} - \frac{r}{R_0} + \Delta'(2s-3) \ , \tag{2.67}$$

where s is the shear. Replacing Eq. 2.67 into Eq. 2.64, and neglecting higher order corrections gives

$$\alpha_{\mathrm{GK}} \sim -q^2 R_0 \frac{\partial \beta}{\partial r} \rightarrow \alpha_{\mathrm{MHD}} \ . \tag{2.68}$$

Finally, if we take Eqs. 2.55,2.62 and 2.63 into Eqs. 2.28 and 2.29 we can write a specific form for the curvature drifts coefficients $\omega_{ds}^{(1)}$ and $\omega_{ds}^{(r)}$, given by

$$\omega_{ds}^{(1)} \doteq k_\theta \frac{2v_\parallel^2 + v_\perp^2}{2\Omega_{\mathrm{cs}} R_0}\left[\cos\theta + s\theta\sin\theta - \alpha_{\mathrm{MHD}}\sin^2\theta\right] - k_\theta \frac{v_\parallel^2}{2\Omega_{\mathrm{cs}}}\frac{\partial \beta}{\partial r} \ , \tag{2.69}$$

$$\omega_{ds}^{(r)} \doteq -i\,\frac{2v_\parallel^2 + v_\perp^2}{2\Omega_{\mathrm{cs}} R_0}\sin\theta \ . \tag{2.70}$$

In the same fashion, the diamagnetic frequency (Eq. 2.30) can be written as

$$\omega_{*s} \doteq -\frac{k_\theta}{B_0}\left[\frac{1}{L_{ns}} + \left(\frac{m_s v^2}{2T_s} - \frac{3}{2}\right)\frac{1}{L_{Ts}}\right] \ , \tag{2.71}$$

where the density and temperature gradient scale lengths are $L_{ns} \doteq -[\partial(\ln\, n_s)/\partial r]^{-1}$ and $L_{Ts} \doteq -[\partial(\ln\, T_s)/\partial r]^{-1}$, respectively. Finally, the only remaining quantities that require some algebra and serve an illustrative purpose are ζ_x and ζ_y (Eq. 2.46) found in the gyroaverage operator. In this particular geometry they reduce to

$$\zeta_x \doteq -k_\theta\left(s\theta - \alpha_{\mathrm{MHD}}\sin\theta\right) \quad \text{and} \quad \zeta_y \doteq k_\theta \ . \tag{2.72}$$

3

Particle Transport in a Pure Plasma

3.1 Introduction

In this chapter we would like to know when particle pinches occur, what is their dependence on critical parameters and more importantly, their effect on density peaking. This problem has been one of the most studied in particle transport, both theoretically and experimentally; in fact, such a pinch is necessary to explain the observed equilibrium density profiles in the core of a tokamak, where (as mentioned before) the particle source is almost negligible and the plasma flow is virtually zero. Coppi and Spight [31] were the first to elaborate on a pinch theory, although their detailed arguments are more suitable for the edge of the plasma. Their proposed mechanism for inward flow is the so called ion-mixing mode, which includes the effect of ITG mode turbulence on the nonadiabatic electron response. It was argued that kinetic electrons determine the particle transport of ions and electrons (because transport is ambipolar). The analysis ignored toroidal and shear effects, and assumed the collisional drift wave (CDW) limit. Because of this last assumption, only the circulating electrons contribute to the pinch, specifically a thermal pinch (also called thermodiffusion, as will be discussed shortly) since the inward flow component of the total transport is proportional to $\nabla T_e/T_e$, where T_e is the electron temperature. The key insight of Coppi and Spight was to observe that at the null flow point where the density gradient outward drive is balanced by the inward temperature gradient drive, the CDW mode (which rotates in the electron direction) would be stable.

Thus, an unstable ion-direction ITG mode is the required source of the turbulence. If the density peaks too much driving $\eta_i \doteq L_{ni}/L_{Ti}$ below threshold, the ITG mode will also be stabilized. Here, L_{ni} and L_{Ti} are the ion density and temperature gradients scale lengths respectively.

Subsequent works [110, 106] attempted to generalize this paradigm to the more collisionless regime appropriate to the core. The details of the Coppi-Spight theory actually apply only to the highly collisional edge where the fueling supplies the flow and a pinch is usually not needed. Ref. [110] considered the dissipative (low collisionality) regime where the trapped electron mode is excited and therefore can play a significant role. This study used sheared-slab geometry including an *ad hoc* division of electron velocity space into trapped and circulating regions. It was found that for the dissipative trapped electron mode (DTEM) the particle flow is outward. An improvement over this work [106] considered lower collisionality and showed that the trapped electron response can have a thermal pinch in the collisionless trapped electron mode (CTEM) regime. The major difference with previous works was that curvature was included, which allows a finite growth rate in the collisionless limit. It is worth mentioning that all the previous theories used quasilinear approximations to estimate the particle flow. More importantly, all acronyms used here (CDW, DTEM and CTEM) in reality refer to the electron-direction drift wave in different collisionality regimes. In all cases the ion-direction ITG mode is required to drive the turbulence at the null flow point.

More recently, a new approach emerged where pinch effects are not directly associated with density or temperature gradients but involve magnetic field curvature which can induce a pinch as the result of subtle functional constraints [116, 59, 10, 9]. Using a 3D fluid model of ITG/TEM turbulence, Garbet, *et al.* [45] were able to confirm the existence of a curvature-drift pinch in addition to the usual thermal pinch. In Ref.[45], a model expression for the particle flow of a given species is proposed. In the same spirit, we introduce a particle flow model (Γ) with three distinct terms

$$\Gamma = n\left(D^n\frac{1}{L_n} - D^T\frac{1}{L_T} - D^q\frac{d\ln q}{dr}\right) \quad . \tag{3.1}$$

In the expression above, n is a density, T is a temperature, r is a radial coordinate and q is the safety factor. The superscripts n, T and q in the diffusion coefficients refer to density gradient, temperature gradient and q-gradient mechanisms respectively. Refs. [116, 59, 10, 9] ignore the thermal pinch and always have the null point at $\partial(nq)/\partial r = 0$ so that the core peaked density profile is determined by the outwardly peaked q-profile.

The remainder of this chapter is organized as follows: In Sec. 3.2, a description of units and conventions is presented. Sec. 3.3 describes the nonlinear simulations used for this study. In Sec. 3.4 the effect of ion and electron temperature gradients on the pinch is studied, whereas Sec. 3.5 looks at the effect of electron-ion collisions. In Sec. 3.6 we investigate pinches due to electron curvature drift using quasilinear theory. Sec. 3.7 discusses the connection between particle pinches and density peaking. Finally, in Sec. 3.8, we offer a concluding summary.

3.2 Units and conventions

Length is measured in units of the minor radius a, mass in units of the deuterium mass m_{D}, temperatures in units of T_e (electron temperature) and velocities in units of the deuterium sound speed ($c_s \doteq \sqrt{T_e/m_{\mathrm{D}}}$). Frequencies and growth rates use a combination of the former and are measured in units of c_s/a. Because diffusivities have a natural gyroBohm scaling, we will generally normalize these to a reference gyroBohm level $\chi_{\mathrm{GB}} \doteq \rho_s^2 c_s/a$, where $\rho_s \doteq c_s/\Omega_{c\mathrm{D}}$ is the deuterium-sound Larmor radius and $\Omega_{c\mathrm{D}} = eB/m_{\mathrm{D}}$ is the deuterium cyclotron frequency.

The particle and energy fluxes for each species (deuterium and electrons), Γ and Q, are related to the particle and energy diffusivities, D and χ, according to

$$\Gamma = -D\,\frac{\partial n}{\partial r} \quad \text{and} \quad Q = -n\chi\,\frac{\partial T}{\partial r} \ , \tag{3.2}$$

where n and T refer to the equilibrium density and temperature, and r is a flux-surface label (physically, the midplane minor radius). The density and temperature gradient scale lengths are $L_n \doteq -[\partial(\ln n)/\partial r]^{-1}$ and $L_T \doteq -[\partial(\ln T)/\partial r]^{-1}$, respectively. Consequently, a negative density gradient means that particle density increases with radius (outwardly peaked profile), whereas a positive density gradient implies the usual inward-peaked profile. A detailed discussion about the meaning of these fluxes and how they relate to physical units can be found in Appendix A.

3.3 Nonlinear simulations

The methodology employed here was to first find the qualitative behavior of selected cases using GLF23 [111], and subsequently get quantitative results using GYRO [20]. The salient point is that for the cases considered here, a single GLF23 run takes less than a second on a desktop workstation, whereas GYRO takes about 5 hours using 32 MSPs on the Cray X1. For most of the cases considered, the GYRO–GLF23 agreement is quite good, although in a minority of cases we have been able to find notable discrepancies.

All nonlinear results use the GA Standard Case (STD) parameters [111] (for which GLF23 has been calibrated) as a reference point. These are $1/L_{Te} = 1/L_{Ti} = 3$, $1/L_{ne} = 1/L_{ni} = 1$, $R = 3$, $r = 0.5$, $s = 1$, $q = 2$, $T_e = T_i$, $\alpha = 0$, $\beta_e = 0$, $\nu_{ei} = 0$, $k_\theta \rho_s = 0.3$. Deuterium is taken as the main ion species. In addition, we use kinetic electrons ($m_i/m_e \simeq 3600$) and simplified $s - \alpha$ circular geometry. All departures from this set of parameters will be explicitly indicated. Our motivation for using these parameters is two-fold: (1) they are roughly typical of a central location in the tokamak where the gyrokinetic equations are believed to provide an accurate description of the plasma, and (2) various previous studies have been done using them.

For the first part of this chapter we are interested in local studies and thus run GYRO in the flux-tube limit. Our normal code resolution uses a 128-point velocity-space grid (8 energies, 8 pitch angles and 2 signs of velocity), and 10 poloidal (orbit) gridpoints per sign of velocity. Experience gained over three years of GYRO use, after hundreds of simulations, indicates that ITG modes are in fact very well-resolved at this velocity-space resolution even for non adiabatic electrons. Adequate resolution of the perpendicular directions $(x, y) \to (r, \varphi)$ tends to be more problematic and needs to be scrutinized for each parameter set. Since we are restricting attention to flux tubes, we content ourselves with an $(L_x, L_y) = (128, 128)$ box, $n_r = 140$ radial gridpoints (so that $\Delta r/\rho_s = 0.91$), and $n_n = 16$ complex toroidal modes. With these choices, we resolve up to $k_\theta \rho_s = 0.75$.

Recent results by Hallatschek and Dorland [49] appear to suggest that simulations relevant to particle transport need to resolve very small radial and poloidal scales. The possibility of this effect motivated a perpendicular resolution study. For this we performed two runs using the resolution defined in the previous section, but in a smaller

Table 3.1 Results for box-size and perpendicular-grid-size convergence study. In the "Simulation" column, L=Large Box, S=Small Box; C=Coarse Grid, F=Fine Grid.

Simulation	χ_i	χ_e	D_i	Δ_r/ρ_s	$(k_\theta\rho_s)_{\max}$	(L_x, L_y)
L/C	11.82	3.48	-1.93	0.91	0.75	(128,128)
S/C	9.33	2.76	-1.52	0.91	0.75	(64,64)
S/F	9.07	2.53	-1.62	0.46	1.5	(64,64)

$(L_x, L_y) = (64, 64)$ box. The first used the same perpendicular grid size: $k_\theta\rho_s \leq 0.75$ and $\Delta r/\rho_s = 0.91$ (achieved by setting $n_n = 8$ and $n_r = 70$). The second used twice the resolution in each dimension: $k_\theta\rho_s \leq 1.5$ and $\Delta r/\rho_s = 0.46$ (obtained by taking $n_n = 16$ and $n_r = 140$). The results of these two small-box cases are compared with our baseline $(L_x, L_y) = (128, 128)$ case, as summarized in Table 3.1.

Two conclusions are readily apparent. First, the smaller boxes slightly underestimate the transport magnitude in all channels compared to our baseline case (L/C). Indeed, Fig. 3.1 shows that the large box (dashed curve) is large enough to resolve the peak in the transport spectrum at $k_\theta\rho_s \sim 0.1$, whereas the small box (solid curve) does not resolve this peak and underestimates the transport by roughly 21%. Second, working at finer grid resolution (S/F versus S/C in Table 3.1) reduces the outward particle and energy flows slightly. This may be due to a reduction of effective numerical (upwind) diffusion in the radial direction. The overall effect is insignificant. Note that Fig. 3.1 also shows that while the linear growth rate (dotted curve) in the TEM regime is much higher than in the ITG regime, the actual TEM-driven transport is very small.

3.4 Characteristics of a thermal pinch

Figure 3.2a shows the variation of the normalized ion thermal and particle diffusivities, χ_i and D_i, versus the normalized temperature gradient for GLF23 and GYRO. In these simulations $L_{Te} = L_{Ti}$. Fig. 3.2b shows the analogous plots for the electron dynamics. Both codes show a thermal pinch at sufficiently high η_e. However, GLF23 does not have an accurate threshold and the electron energy flow is too high.

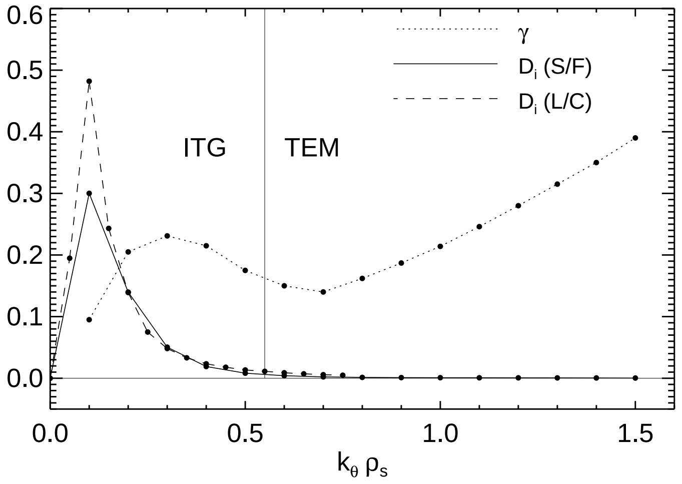

Figure 3.1 Effect of high $k_\theta \rho_s$ on particle flow at two different resolutions: S/F and L/C (see Table 3.1).

3.5 Effect of electron collisions on a thermal pinch

It has been shown recently that in the context of GLF23 transport modeling, electron collisions are needed to accurately reproduce the reduction of the anomalous particle pinch in ASDEX-U [6]. Looking again at the STD case in the collisionless limit, we observe a robust particle pinch (see Fig. 3.2 at $L_{ne}/L_{Te} = 3$). However, Fig. 3.3 shows that this pinch is rapidly converted to outward particle flow as electron collisions are increased from zero. For higher collisionality, the trapped ions flow outward while the passing ions flow inward. This is quite in contrast to the relative behaviour of the passing and trapped electron populations. Because the passing electrons are (nearly) adiabatic and thus in phase with the potential, they suffer little transport. Therefore, to maintain charge neutrality, the trapped electrons must compensate and nearly balance the total ion particle flow. However, it is incorrect to conclude that the pinch disappears for higher collisionality. The pinch threshold simply moves to a higher η_e when collisionality is included.

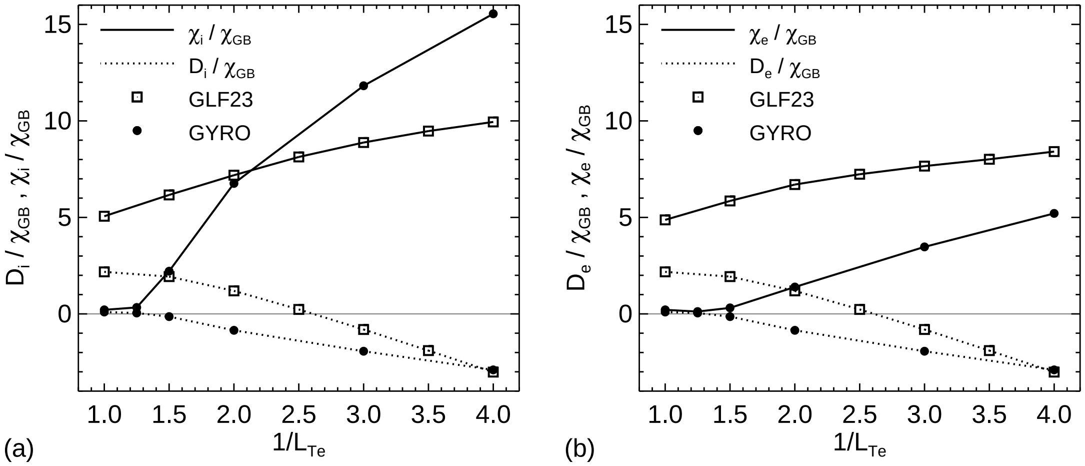

Figure 3.2 L_{Te} scan (at fixed L_{ne}, with $L_{Te} = L_{Ti}$). Plot (a) compares the total ion particle (dotted line) and thermal (solid lines) diffusivity from GYRO (circles) to that from GLF23 (squares). In plot (b), a similar comparison is presented for the electron diffusivities.

3.6 Pinch due to electron curvature drift

The study presented in this section was performed using GYRO quasilinear simulations only. For us, the quasilinear approximation is nothing more than evaluating the nonlinear fluxes using the complex linear eigenmodes and eigenfrequencies at a selected $k_\theta \rho_s$. Specifically, the particle flow is the product of the density perturbation ($\tilde{n}$) and the perturbation of the $\mathrm{E} \times \mathrm{B}$ velocity ($\tilde{v}_{\mathrm{E}\times\mathrm{B}}$) such that $\Gamma = \tilde{n}\, \tilde{v}_{\mathrm{E}\times\mathrm{B}}$. The quasilinear approximation takes $\tilde{n_k} = F(\omega_k)(\tilde{v}_{\mathrm{E}\times\mathrm{B}})_k$ for each mode k with F a complex linear function given by the linear response of the density perturbation to the potential perturbation at the complex linear mode frequency $\omega = \omega_R + i\gamma$.

In order to avoid confusion, we use the same nomenclature as Garbet [45] to describe the different pinch formation mechanisms: *thermodiffusion* [11, 77] for temperature-gradient-driven pinches and *curvature* for magnetic field curvature effects which lead to a q-gradient-driven pinch. When thermal pinches are ignored, a null flow state can arise as indicated in Eq. (3.1). In this case, positive shear can balance a positive density gradient. Figure 3.4 shows a magnetic shear scan in the presence of flat density profiles ($1/L_n = 0$), but with otherwise GA Standard Case parameters ($1/L_{Ti} = 3$, in particular).

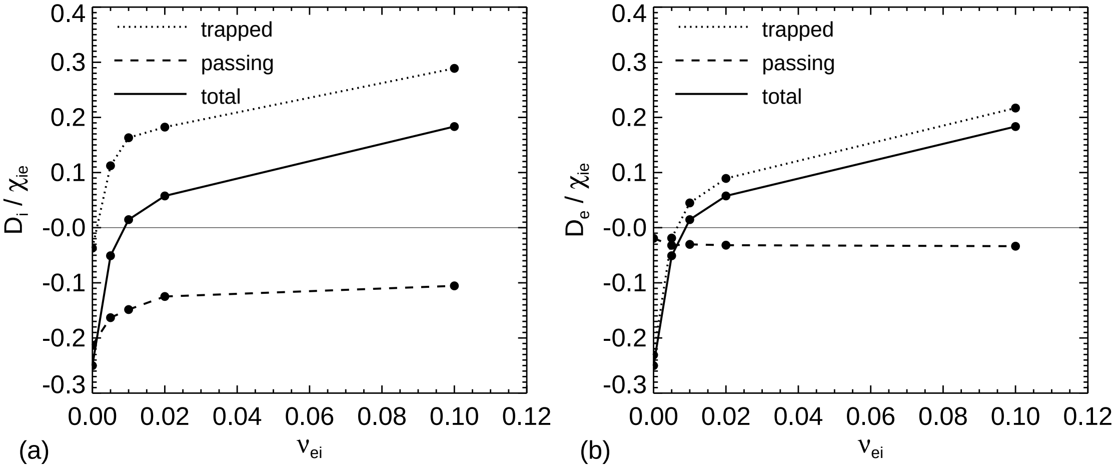

Figure 3.3 Ion particle flow (a) and electron particle flow (b) separated into trapped and passing fractions. The flows are normalized to $\chi_{ie} \doteq (\chi_i + \chi_e)/2$.

The normalized electron fluxes are calculated at $k_\theta \rho_s = 0.3$. Parallel effects (isolated by setting $\omega_d = 0$) with no electron temperature gradient ($1/L_{Te} = 0$) are indicated with a dashed line and denoted by the letter P. A dashed-dotted line indicates parallel plus curvature effects (P+C) with no electron temperature gradient. Since we cannot compute curvature effects (C) directly, we have to infer these effects from (P+C) and (P) so C = (P+C) - P. The subtraction is indicated by a dotted line, showing that for $s > -0.5$ a curvature-driven pinch really exists. When the electron temperature gradient is set to its standard value ($1/L_{Te} = 3$) a much more pronounced pinch is observed (solid line). The main conclusion is that although a curvature pinch exists its effects are almost negligible when compared to the thermodiffusion contribution. Indicated with a cross is the predicted null point in Ref. [45] at $s = -3/8$. Notice also that even when the temperature gradient is turned off ($1/L_{Te} = 0$), the curvature pinch effect can be overwhelmed by the parallel motion effects (i.e. (P+C) is outward).

3.7 The problem of density peaking

Density peaking has recently attracted considerable experimental [4, 100, 89, 113, 118] and theoretical modelling [6, 4, 83, 82, 5] attention. Its importance relies on the

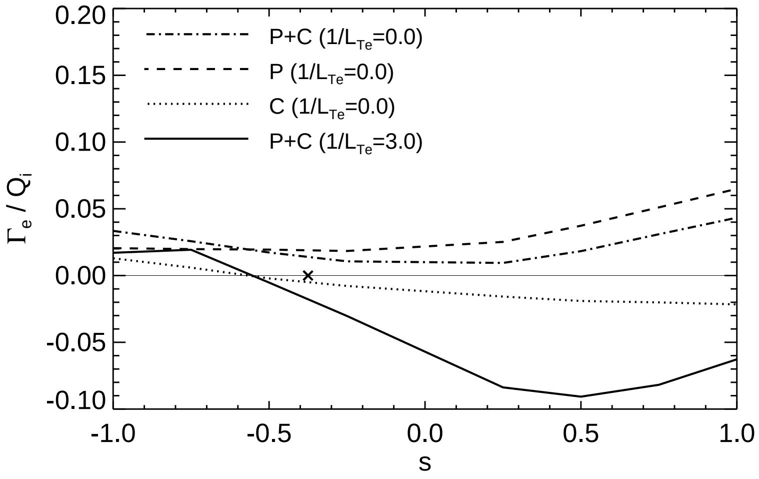

Figure 3.4 Dependence of the normalized electron particle flow on magnetic shear (s). The dashed-dotted line (P+C) shows parallel plus curvature effects. The dashed line (P) shows parallel effects only, whereas the the dotted line shows curvature effects (C) only. The crossing point at $s = -3/8$ is indicated with a cross. The solid line shows thermodiffusion effects ($1/L_{Te} = 3$).

fact that a peaked profile can increase the power production, energy confinement and bootstrap current of the plasma. On the other hand, an excessively peaked pressure profile can reduce the stability limit. For these reasons, it is important to understand this phenomenon, and predict its occurrence and effects in future reactors such as ITER. Evidence found in L-mode discharges [117, 46] suggests that a turbulent particle pinch is responsible for the observed peaking.

Although the simulations presented in the previous sections found enough evidence of a turbulent pinch for typical experimental parameters, the connection between density peaking and the thermal pinch remains unclear. One of the main reasons is that density peaking is a global problem, whereas our previous analysis was local. Another problematic issue with ITG/TEM simulations is the strong reduction of the pinch intensity when realistic collisionality is included.

The purpose of this section is to answer if the ITG/TEM pinch can be responsible for the observed density peaking in experiments. This question was previously addressed using linear gyrokinetic simulations and a quasilinear model [5]. It was found that for the most relevant cases such a description failed to describe the peaking. However, we believe

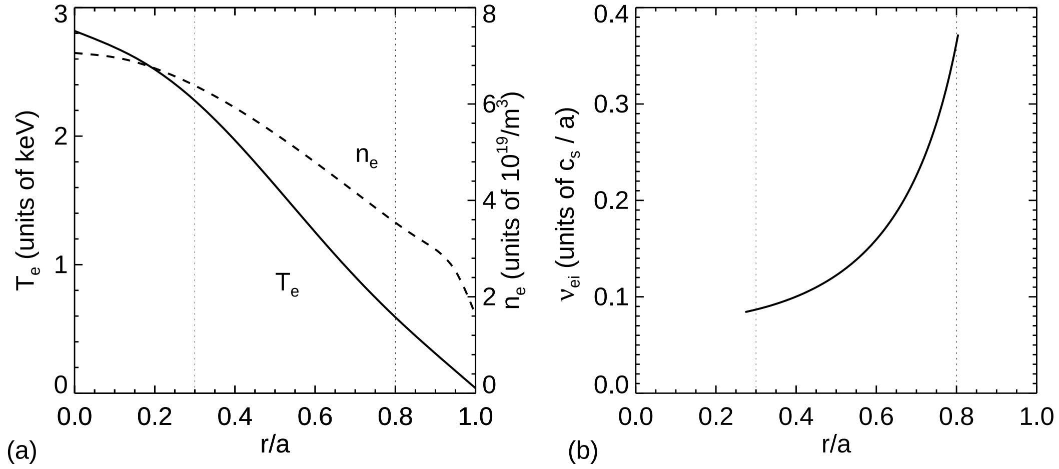

Figure 3.5 DIII-D profile data for discharge 101391. Plot (a) shows experimental electron density and temperature profiles, while plot (b) shows the calculated electron-ion collisionality based on these profiles. The vertical dotted lines denote the radial domain used in the simulations.

that the main issue is not a question of the physics model involved but of the realism of the simulations used. To test this hypothesis we present GYRO [20] simulations of a DIII-D L-mode discharge (shot 101391) [75]. These include nonlinear gyrokinetic ions and electrons, radial profile variation with **E**×**B** rotation, shaped geometry, electron pitch-angle scattering and electromagnetic fluctuations. Previous studies [19] have shown that this level of realism is enough to match the experimentally-inferred energy transport coefficients with less than 10% adjustment of the ion temperature gradient.

In the simulations that follow we use the same units and conventions defined at the beginning of the chapter. It is important to mention that all of the simulations used in this particular study have the same reference radius ($r/a = 0.6$). The reference radius is the point where normalizations such as c_s or ρ_s are computed and where the resolution is best. For example, at this radius the electron-ion collision frequency is given by $\nu_{ei} = 0.16$ (units of c_s/a) and $\rho_* = 0.0025$. Here, $\rho_* \doteq \rho_s/a$ is the relative gyroradius. A detailed summary of all the experimental parameters with their respective physical units is given in Ref. [105] (Table I), and some of the most relevant experimental profiles are shown in Fig. 3.5. Finally, these simulations include two gyrokinetic species (ions and electrons), and equal density gradients ($1/L_{ni} = 1/L_{ne}$) to satisfy plasma neutrality.

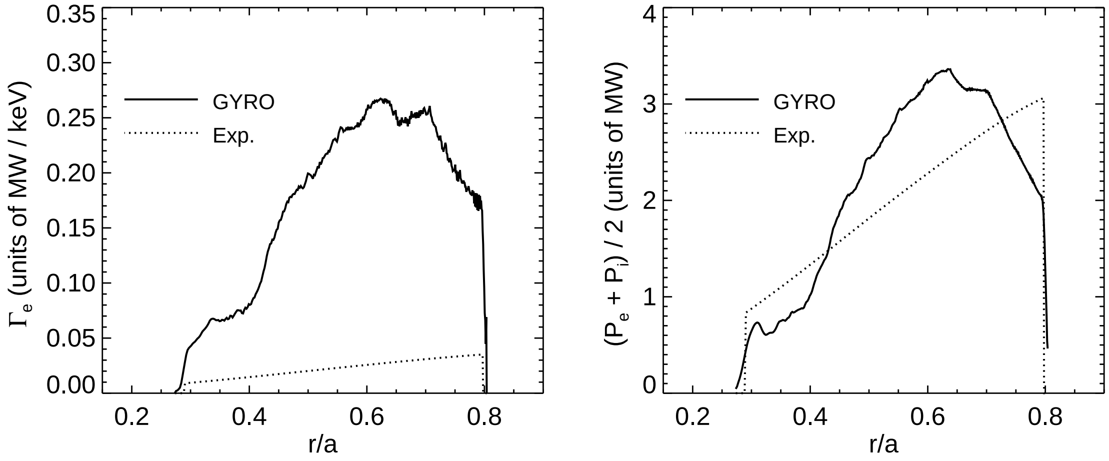

Figure 3.6 Radial electron particle flow in MW/keV (a) and average energy flow in MW (b) from baseline simulation (solid line), compared to their experimental counterparts.

With respect to code resolution we use a 128-point velocity-space grid (8 energies, 8 pitch angles and 2 signs of velocity), and 10 poloidal (orbit) gridpoints per sign of velocity. For the radial direction we employ a nonuniform grid with 360 radial grid points and a span of $0.3 < r/a < 0.8$. Finally, in the k_θ direction we have $n_n = 16$ complex toroidal modes and resolve up to $k_\theta \rho_s \leq 0.9$. This resolution is almost identical to that used in Ref. [105], although the radial resolution is 50% higher (360 instead of 240 radial grid points). It is important to mention that we used a reduced ion to electron mass ratio ($\mu_e \doteq \sqrt{m_i/m_e}$) of 40 instead of the physical 60, which is computationally more efficient, and does not significantly alter the results. Indeed, a previous study [105], found that $\mu_e = 40$ (even $\mu_e = 30$) is more than adequate for this type of discharges. Since these simulations include profile variation, an adaptive source is used to ensure that there is no turbulent modification to the equilibrium density and temperature profiles. The details of the algorithm used can be found in Ref. [104].

The strategy used here was to initially obtain a baseline case that matches the experiment, and subsequently change the electron density ($L_{ne} \doteq -[\partial(\ln n_e)/\partial r]^{-1}$) and temperature ($L_{Te} \doteq -[\partial(\ln T_e)/\partial r]^{-1}$) gradients lengths to determine if a pinch can exist under experimental conditions. The resulting electron particle flow for the baseline case compared to the experimental one is shown in Fig. 3.6a, and the resulting average energy

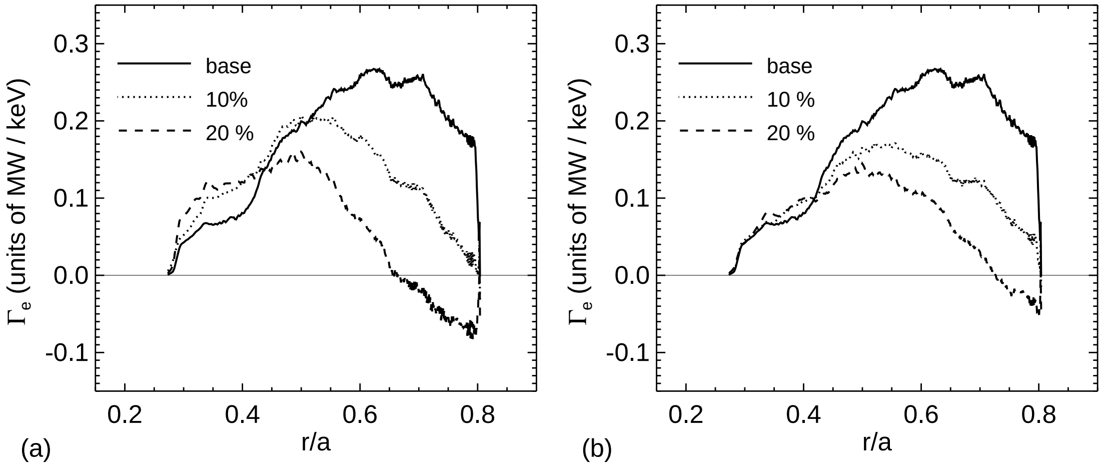

Figure 3.7 Plot (a) shows the variation of radial electron particle flow as $1/L_{te}$ is increased by 10% and 20% while $1/L_{ne}$ is kept fixed. Plot (b) shows the same variation when $1/L_{ne}$ is decreased by 10% and 20% and $1/L_{te}$ is kept fixed.

flow $(P_e + P_i)/2$ is shown in Fig. 3.6b. Notice that in this, and all other simulations, we smoothed the plots with a 5-point box-car average to guide the eye. We also lowered $1/L_{Ti}$ by 10% in all our cases in order to match the experimental χ_i and χ_e, otherwise the levels predicted could be a factor of two higher than the experimental ones. This strong sensitivity of χ_i and χ_e to L_{Ti} is a consequence of the stiffness inherent in the transport problem, which is rather striking if we consider that the experimental error for $1/L_{Ti}$ is about 10% as well. To further highlight the difficulty of this problem, the averaged experimental electron and ion power at $r/a = 0.6$ and $T_e = 1.25$ keV is 2.28 MW, whereas the experimental electron plasma flow is only 0.0256 MW/keV at the same radius and temperature. We emphasize that the small value of the electron plasma flow, which is the result of an almost negligible particle source, is very difficult to replicate in the simulations without adjusting the electron profiles at every radius. However, the average energy flow (Fig. 3.6b) shows very good agreement between simulation and experiment showing that the relevant physics are captured overall.

For the first scan we kept $1/L_{ne}$ fixed to its experimental value and raised $1/L_{Te}$ by 10% and 20%. The resulting plasma flow can be seen in Fig. 3.7a. Increasing the electron temperature gradient reduces the flow magnitude for both cases as expected from ITG considerations, and in the 20% case it creates a pinch for $r/a > 0.65$. A similar effect,

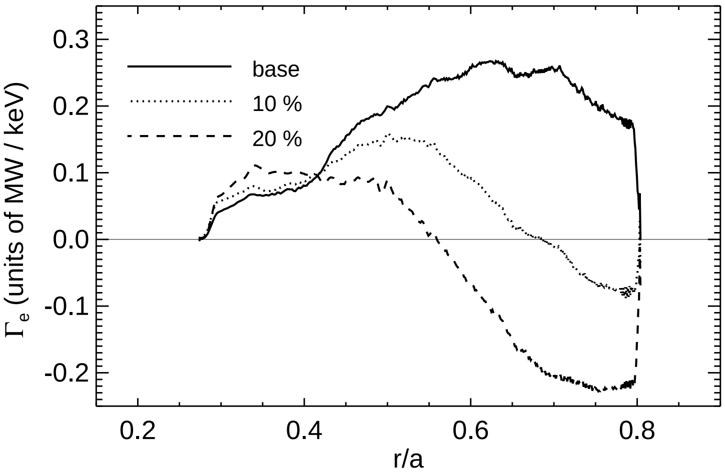

Figure 3.8 Variation of radial electron particle flow as $1/L_{te}$ is increased and $1/L_{ne}$ is decreased simultaneously by 10% and 20%.

albeit less dramatic, can be observed in Fig. 3.7b when $1/L_{ne}$ is decreased by 10% and 20%, while keeping $1/L_{Te}$ fixed to its experimental value. In this case the pinch is not as strong, although the flow is considerably reduced in most of its radial domain. It is important to mention that the experimental error for $1/L_{Te}$ and $1/L_{ne}$ is around 5% and 10% respectively. For the final scan we used a combination of the former, and simultaneously raised and decreased $1/L_{Te}$ and $1/L_{ne}$ respectively, as shown in Fig. 3.8. Unsurprisingly, the most dramatic effects are observed in this case, where the flow is greatly reduced for the 10% case with a pinch in some regions ($r/a > 0.7$), and strongly pinched for $r/a > 0.55$ in the 20% case.

One might object to these results on the grounds that they were obtained by adjusting the gradients everywhere by the same amount, or that the 20% cases were above the experimental uncertainity. *However, our main objective was to illustrate the possibilty of obtaining a pinch and consequently a density peaking under experimental conditions, in particular when "high" collisionality is included.* An improvement over this work can be done by adjusting individually the temperature and/or density gradients using a feedback mechanism, in order to get a "perfect" matching with the experimental flows. This type of approach, which has been used succesfully in a simpler electrostatic simulation with $\mu_e = 20$ and $\rho_* = 0.004$ [103], found that when the simulation flows agrees with the experimental ones at every radius, a peaking of the density is observed. The discharge in Ref. [103] is dimensionally-similar to the discharge considered here and therefore has the same collisionality.

3.8 Conclusions

The principal results of this chapter can be separated in two parts. First, we investigated the particle transport in pure plasmas via local simulations. In more detail, the different pinch formation mechanisms were studied, indicating that the temperature gradient plays the dominant role. Electron collisions, on the other hand, generally oppose the production of a thermal pinch.

In the second part, we addressed the problem of density peaking using global simulations of L-mode DIII-D discharges and found the existence of a pinch under experimental conditions. These results reconcile the apparent discrepancies between anomalous pinches and collisionality. Such evidence supports our hypothesis that fully realistic simulations are crucial to the reliable calculation of experimental flows.

3.9 Acknowledgement

The text of this chapter, in full, includes material from “Gyrokinetic simulations of ion and impurity transport” [C. Estrada-Mila, J. Candy and R.E. Waltz, Phys. Plasmas **12**, 022305 (2005)] and “Density peaking and turbulent pinch in DIII-D discharges” [C. Estrada-Mila, J. Candy and R.E. Waltz, submitted to Phys. Plasmas (2006)]. The dissertation author was the primary researcher.

4

Particle Transport in Impure Plasmas

4.1 Introduction

In this chapter we study the case of plasmas with two ion species, in which the second one can play the role of an impurity. As mentioned in the introduction of this dissertation, we first study the effects of helium ash followed by a study of plasmas with deuterium and tritium. Although previous works on multi-species plasmas used the gyrokinetic description [36, 35], the focus was mainly on impurity-driven instabilities and their effect on ITG modes. These studies did not include trapped particles, the electron response was assumed to be adiabatic, and there was little or no discussion of impurity flows. More recent studies, on the other hand, used the same degree of realism presented here, however particle transport was not studied per se [91, 19, 41].

The methodology of this chapter follows closely the same one used previously. First, we find the qualitative behavior of selected cases using GLF23, and subsequently get quantitative results using GYRO. The GA Standard Case parameters are used again and deuterium is taken as the main ion species. Concerning the code resolution, we use the same one as before: 128-point velocity-space grid (8 energies, 8 pitch angles and 2 signs of velocity), and 10 poloidal (orbit) gridpoints per sign of velocity with an $(L_x, L_y) = (128, 128)$ box, $n_r = 140$ radial gridpoints and $n_n = 16$ complex toroidal modes. With these choices, we resolve up to $k_\theta \rho_s = 0.75$.

The remainder of this chapter can be divided roughly in four parts. The first part presents some preliminary information concerning units, coventions and methodologies (Secs. 4.2 and 4.3), followed by a discussion of deuterium plasmas with helium ash (Secs. 4.4 and 4.5). The third one addresses the transport of D-T plasmas (4.6), while the fourth and final part presents a theoretical analysis of the most relevant results (4.7). Finally, a concluding summary is presented in Sec. 4.8.

4.2 Units and conventions

The same units of length, mass and temperature used in the previous chapter are employed here. Similarly, the diffusivities are normalized to a reference gyroBohm level. However, in order to avoid ambiguity we define a reference deuterium gyroBohm diffusivity, χ_{GBD}, for which $m_i \rightarrow m_{\mathrm{D}}$. Also, the symbol σ is used as the most general species label, for which three general values are allowed: i (main ion), I (impurity ion) and e (electron). Specific ion species present in the simulations will be denoted by their standard chemical symbol. The density and temperature gradient scale lengths are $L_{n\sigma} \doteq -[\partial(\ln n_\sigma)/\partial r]^{-1}$ and $L_{T\sigma} \doteq -[\partial(\ln T_\sigma)/\partial r]^{-1}$, respectively. Consequently, a negative density gradient means that particle density increases with radius (outwardly peaked profile), whereas a positive density gradient implies the usual inward-peaked profile.

It is important to warn the reader that in experimental work, the particle diffusivity is often separated into a diffusive part and a convective part

$$\Gamma_\sigma \rightarrow -D_\sigma^d \frac{\partial n_\sigma}{\partial r} - n_\sigma v_{\mathrm{in}} \ , \tag{4.1}$$

where D_σ^d is the turbulent diffusion coefficient and v_{in} is an inward convective velocity. When inward convection dominates diffusion, there is a net inward flow of particles (i.e. particle pinch). For the analysis which follows, it will be convenient to define an effective ion energy diffusivity and effective ion flux as

$$\chi_{\mathrm{eff}} = \frac{n_i \chi_i + n_{\mathrm{I}} \chi_{\mathrm{I}}}{n_i + n_{\mathrm{I}}} \quad \text{and} \quad Q_{\mathrm{eff}} = -(n_i + n_{\mathrm{I}}) \chi_{\mathrm{eff}} \frac{\partial T_i}{\partial r} \ . \tag{4.2}$$

In the previous expressions, r is a flux-surface label (physically, the midplane minor radius).

Finally, the charge dilution is defined as $f_{\mathrm{I}} \doteq z_{\mathrm{I}}\,(n_{\mathrm{I}}/n_e)$ where, as we have previously indicated, the subscript I refers to the impurity species. In order to satisfy plasma neutrality the following relation between density gradients must be satisfied:

$$\frac{1}{L_{ni}} = \frac{1/L_{ne} - f_{\mathrm{I}}/L_{n\mathrm{I}}}{1 - f_{\mathrm{I}}} \quad . \tag{4.3}$$

4.3 Quasilinear results

As an aid in understanding certain fully nonlinear results, we sometimes use a simple type of quasilinear approximation. This is nothing more than evaluating the nonlinear fluxes using the complex linear eigenmodes and eigenfrequencies at a selected $k_\theta \rho_s$. Specifically, the particle flow is the product of the density perturbation ($\tilde{n}$) and the perturbation of of the E × B velocity ($\tilde{v}_{\mathrm{E\times B}}$) such that $\Gamma = \tilde{n}\,\tilde{v}_{\mathrm{E\times B}}$. The quasilinear approximation takes $\tilde{n_k} = F(\omega_k)(\tilde{v}_{\mathrm{E\times B}})_k$ for each mode k with F a complex linear function given by the linear response of the density perturbation to the potential perturbation at the complex linear mode frequency $\omega = \omega_R + i\gamma$.

4.4 Density gradient effects

We first consider the effect of density gradient scale length, $L_{n\mathrm{He}}$, on the particle transport for both ion species. It is of interest to determine when a turbulent pinch due to density gradient is created. In this section, the particle diffusivities D_{He} and D_i are normalized to the effective energy diffusivity, χ_{eff}, given by Eq. (4.2), whereas $1/L_{n\mathrm{He}}$ was normalized to $1/L_{ne}$. First, Fig. 4.1a shows the effect of helium density gradient (including negative, or inverted, gradients) on the D/χ-ratio as estimated by the GLF23 code. Results are given for two impurity concentrations: $f_{\mathrm{He}} = 0.1$ and $f_{\mathrm{He}} = 0.3$. Figure 4.1b shows the GYRO simulations.

The results are in very good qualitative agreement, showing that for sufficiently weak, positive helium gradient, a helium pinch is created. Figure 4.2 shows analogous plots for the main ions. For positive gradients, we see a robust inward flow of the main

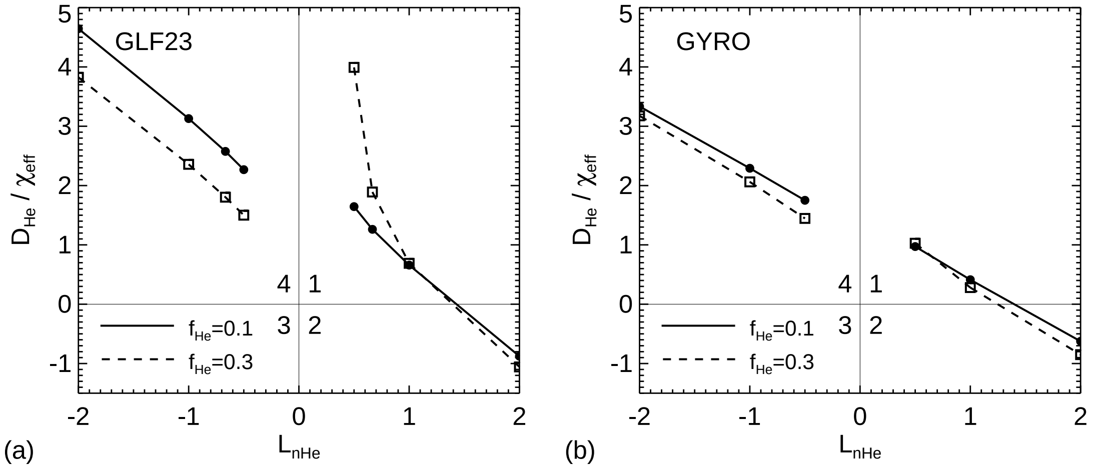

Figure 4.1 Normalized impurity flow, D_{He}, versus $L_{n\mathrm{He}}$ scan (at fixed $L_{ne} = 1$) for two different impurity concentrations: $f_{\mathrm{He}} = 0.1$ and 0.3. Quadrant 1 refers to outward flow and a peaked profile, 2 to inward flow and peaked profile, 3 to outward flow and hollow profile, and 4 to inward flow and hollow profile. Plot (a) shows GLF23 results while plot (b) shows GYRO results.

ions. This pinch feature of the GA Standard Case has been already noted in the previous section for the case of a pure plasma. For $L_{n\mathrm{He}}/L_{ne} < 0$ (helium peaked outside) the deuterium flow is outward and the helium flow is inward ($1/L_{ne} = 1$ and $1/L_{n\mathrm{D}}$ remains positive in these runs).

It is instructive to see in more detail how the value D_σ computed by GYRO is related to the diffusive and convective contributions to the transport. Eqs. (A.1) and (4.1) imply

$$D_{\mathrm{He}} = D^d_{\mathrm{He}} - v_{\mathrm{in}} L_{n\mathrm{He}} \quad . \tag{4.4}$$

If the D_{He}–$L_{n\mathrm{He}}$ relationship is assumed to be linear (in other words, D^d_{He} and v_{in} are independent of $L_{n\mathrm{He}}$), then from Eq. (4.4) it follows that D^d_{He} is given by the vertical intercept in Fig. 4.3, whereas the convective velocity v_{in} is given by the slope. From this we can estimate an inward velocity of 12.4 and 11.6 (units of c_s) for $f_{\mathrm{He}} = 0.1$ and 0.3 respectively, and a turbulent diffusion coefficient $D^d_{\mathrm{He}}/\chi_{\mathrm{GBD}} = 17$ for both dilutions. From this it seems that only convective processes have a dependence on impurity concentration, albeit a very weak one (compare solid and dashed lines in Figure 4.3). Zero flux ($D_{\mathrm{He}} = 0$) necessarily implies a balance between convective and diffusive terms.

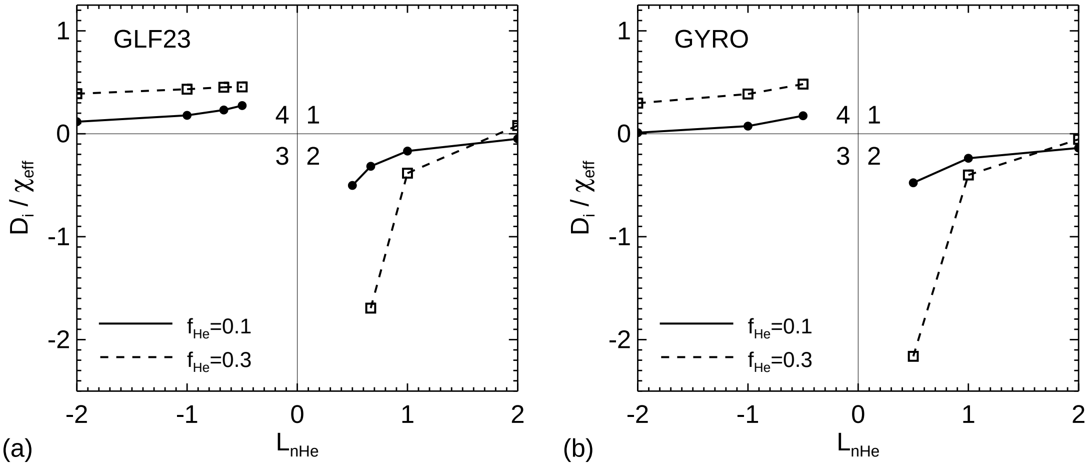

Figure 4.2 Same as Fig. 4.1, except showing the main ion flow, D_i/χ_i, rather than the impurity flow, D_{He}/χ_i. As before, plot (a) shows GLF23 results while plot (b) shows GYRO results (both at fixed $L_{ne} = 1$). According to Eq. (4.3), $1/L_{ni} > 0$ in these scans.

4.5 Dilution effects

The purpose of this section is to study the mechanics of (main ion) dilution and how all ion channels are affected by it. Two fundamental issues are discussed here: the first is the effect of f_{He} on particle transport; the second is the validity of conceivable approximations to multiple-species transport, such as the "dilution model" and the "lumped-mass approximation". Neither of these discuss the transport of impurities and are intended only to describe the effect on energy transport.

Here the dilution model is taken to mean that impurities do not respond to the potential and are assumed to have no flow. Equilibrium charge neutrality is maintained, so that the only effect of increasing f_{He} is the dilution of the main ions. The impurity ion gradient enters only via Eq. (4.3). The lumped-mass approximation, on the other hand, creates a fictitious species [36] with atomic mass M defined by:

$$M = (1 - f_{\mathrm{I}})\, m_i + f_{\mathrm{I}}\, m_{\mathrm{I}} \ . \tag{4.5}$$

For example, this would give rise, in a 50-50 D-T mixture, to the notion of a DT ion with an effective mass of $M = 2.5\, m_{\mathrm{H}}$. If the impurity has a different charge state than

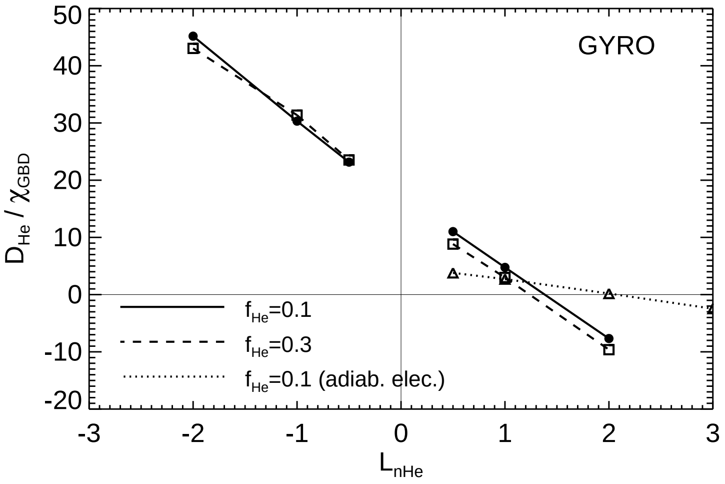

Figure 4.3 Helium diffusivity, $D_{\rm He}$, versus $L_{n\rm He}$ scan (at fixed $L_{ne} = 1$) for two different impurity concentrations: $f_{\rm He} = 0.1$ (solid line) and 0.3 (dashed line), using GYRO. The diffusive term D^d_σ is given by the vertical intercept of the graph whereas the convective velocity $v_{\rm in}$ is given by its slope. The dotted line shows the results for adiabatic electrons at $f_{\rm He} = 0.1$.

the main ion, one might also introduces an effective charge

$$Z = (1 - f_{\rm I})\, z_i + f_{\rm I}\, z_{\rm I} \ . \tag{4.6}$$

In this approximation, the lumped ion species is assumed to have the same profile as the background ions. For this study we have considered two qualitatively different plasmas: one in which impurities are inwardly peaked ($1/L_{n\rm He} > 0$), such as helium ash born at the core, and the opposite case for which the impurities are outwardly peaked ($1/L_{n\rm He} < 0$), such as incoming edge particles. For the lumped-mass approximation there is no distinction.

4.5.1 Inward impurity peaking

For positive $1/L_{n\rm He}$ there is little variation in the transport of helium (solid curves in Fig. 4.4a as $f_{\rm He}$ is increased, whereas better deuterium confinement is predicted (solid curves in Fig. 4.4b. This result agrees with experimental trends observed recently in DIII-D, and previously in several other machines (Ref. [74], and references therein).

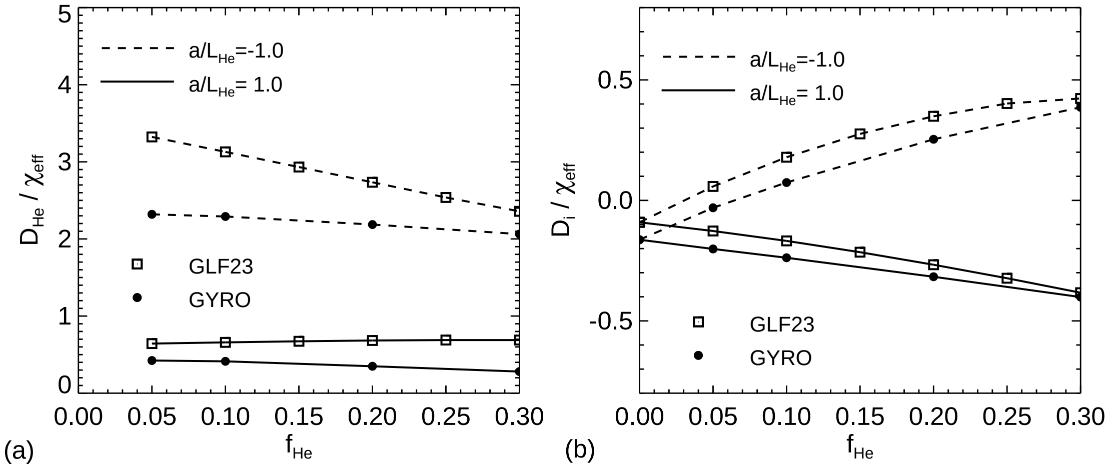

Figure 4.4 Particle flow, D_i and D_{He} as functions of impurity fraction, f_{He}. Here, two different impurity density gradients, $1/L_{n\mathrm{He}} = \pm 1$, are considered. Plot (a) compares D_{He} results for GLF23 and GYRO, while plot (b) compares D_i results.

This corresponds to the so-called radiative impurity (RI) mode in which a controlled amount of impurities tends to improve confinement.

One of the key factors in a fusion plasma is the efficient removal of helium ash. Although this problem is global in nature, since ash is generated at the core and pumped out at the edge, we can use some of our results to address this problem. The most critical quantity in this problem is the ratio between the helium ash removal time and the energy confinement time $\rho \doteq \tau_{\mathrm{He}}/\tau_E$, with a permissible operational value of $\rho \leq 7 - 15$ [85]. This confinement time ratio is usually determined by the χ/D-ratio. By looking again at Fig. 4.4 we can estimate a ratio $\chi/D \approx 2.5 - 3$ for GYRO and $\chi/D \approx 1.7$ for GLF23. Both estimates are essentially independent of dilution and give a reasonable estimate for our particular radial location. In reality, a detailed answer to the problem of helium ash removal will require a global simulation, following the dynamics from core to edge. Our results here show that GLF23 could be well-suited for such an efficient global study of this problem.

4.5.2 Outward impurity peaking

For negative $1/L_{n\mathrm{He}}$ (same figures) we discover a somewhat more interesting result: while the helium impurity ions experience a slightly improved confinement with increased f_{He} (this improvement is overestimated by GLF23), the bulk deuterium ions experience a degradation of confinement. In particular, at the critical value $f_{\mathrm{He}} \simeq 0.07$ the deuterium goes from being pinched to flowing toward the plasma edge, but helium is flowing inward while the electrons are still pinched. This behavior has been previously noted; that is, whenever two ion species peak in different radial regions, the plasma is more unstable [29]. The physical mechanisms behind this phenomenon will be discussed in the analysis section. We remark that GLF23 captures this behaviour quite accurately.

4.5.3 The dilution model

Figure 4.5 looks at the variation of energy transport with dilution as obtained from GYRO. For the case of a negative impurity density gradient, as seen in Fig. 4.5a, the dilution model is in poor agreement with the fully kinetic model of impurities. In the opposite case, shown in Fig. 4.5b, fair agreement is obtained for small values of dilution ($f_{\mathrm{He}} < 0.05$), although for larger values a dramatic loss of accuracy is observed. The reason behind these discrepancies is that the dilution model gives raise to a nonphysical electron-direction mode when $f_{\mathrm{He}} \geq 0.2$. Thus, when using GYRO, one should either treat impurities kinetically, or ignore them altogether. This is particularly true for the case of positive $1/L_{n\mathrm{He}}$ where impurities have a very weak effect on $\chi_{\mathrm{eff}}/\chi_{\mathrm{GBD}}$ (i.e., small differences when compared to the pure plasma case) in the range 0.05 to 0.20.

4.5.4 The lumped-mass approximation

This approximation is better than the dilution model, as would be expected for larger impurity fractions. However, neither model is able to capture the energy confinement degradation for $1/L_{n\mathrm{He}} < 0$. Once again, it seems more sensible to approximate an impure plasma with its pure counterpart.

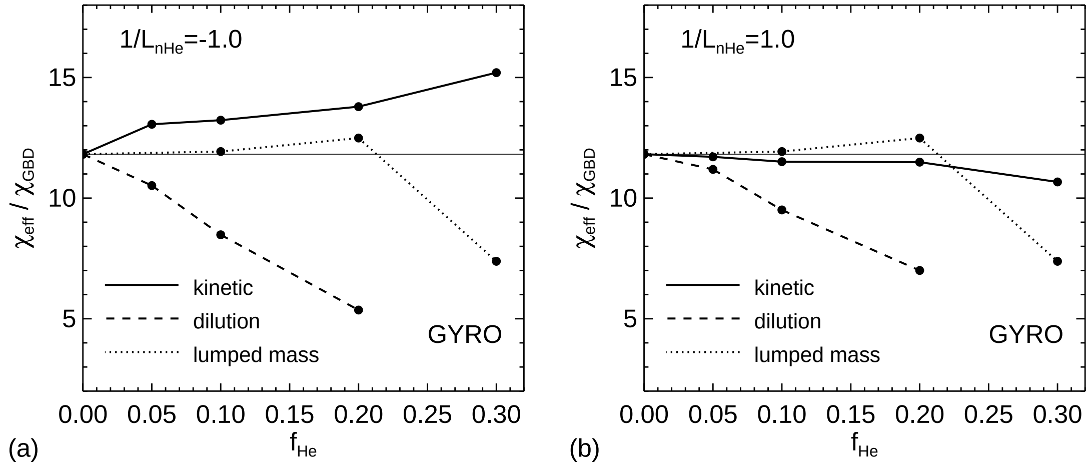

Figure 4.5 GYRO $f_{\rm He}$ scans for $1/L_{n{\rm He}} = \pm 1$, comparing the dilution model with full kinetic dynamics. Plot (a) shows GYRO runs at $1/L_{n{\rm He}} = -1$ while plot (b) shows GYRO runs at $1/L_{n{\rm He}} = 1$. In both cases the lumped-mass approximation is included (triangle at $f_{\rm He} = 0.3$).

4.6 Particle transport in D-T plasmas

It is of interest to determine the particle and energy flux in the case of a mixed deuterium-tritium plasma, but before discussing such a problem it is useful to make some comments about “intrinsic” mass scaling. For ions of arbitrary mass m_i, the intrinsic mass scaling of frequency and diffusivity can be deduced:

$$\text{FREQUENCY} \rightarrowtail \frac{c_s}{a} \propto \frac{1}{m_i^{1/2}} \quad \text{and} \quad \text{DIFFUSIVITY} \rightarrowtail \chi_{\rm GB} \propto m_i^{1/2} \quad . \tag{4.7}$$

Strictly speaking, these scalings will be exactly obtained in the flux-tube (local) limit, such that the there is a single ion species, and the electron mass is removed from the problem, as in the adiabatic electron model. This means that if one simulates a pure-D plasma with adiabatic electrons and obtains $\chi_{\rm D} = C\chi_{\rm GBD}$, then the transport in other pure plasmas can be obtained by scaling arguments alone: $\chi = \sqrt{{\rm A}/2}C\chi_{\rm GBD}$, where A is the isotope atomic mass. Finite electron mass, as treated in this paper, will give rise to a relatively small breaking of these scaling rules through the nonadiabatic part of the electron response. This effect is evident from Table 4.1, where we have summarized the results from a sequence of nonlinear GYRO simulations. Looking at the pure D, DT

Table 4.1 Summary of deuterium-tritium plasma study. All quantities already normalized to $\chi_{\rm GBD}$ (deuterium gyroBohm diffusivity). The D-simulation is the base GA Standard Case. The collisional D+T simulation has a relatively small collision frequency: $\nu_e = 0.01$. Note that the identical value 11.73 in two separate cases is not a typo.

Simulation	$\chi_{\rm D}$	$\chi_{\rm DT}$	$\chi_{\rm T}$	$D_{\rm D}$	$D_{\rm DT}$	$D_{\rm T}$
D	11.82	-	-	-1.93	-	-
Hybrid DT	-	12.84	-	-	-2.19	-
T	-	-	14.40	-	-	-2.49
D+T	12.65	-	11.73	-1.55	-	-2.75
Collisional D+T	12.47	-	11.73	0.846	-	0.128
Adiabatic D+T	4.023	-	3.585	0.202	-	-0.202

(fictitious species) and T energy diffusivities (χ), we see that the ratios (1, 1.08, 1.21) deviate little from the expected $\sqrt{\rm A/2}$ ratios (1, 1.11, 1.22).

The full nonlinear runs with kinetic electrons, as shown in Fig. 4.6, uncover two curious and potentially important results. First, in Fig. 4.6a, we see that the deuterium energy diffusivity in the D-T simulation is actually enhanced slightly from that in the pure-plasma simulation. Second, in Fig. 4.6b, we see that the tritium ions are more strongly pinched than either the deuterium ions in the D-T simulation or the deuterium ions in the pure-D simulations. We emphasize that for the D-T simulation, tritium is considered as the impurity, and so the normalization is with respect to $\chi_{\rm GBD}$ – the gyroBohm diffusivity of deuterium. Although the differences in χ in Fig. 4.6a are small and at the limit of significance, we have verified that trends are preserved as the simulation resolution is changed.

An important potential implication of the stronger tritium pinch is that the resulting offset in particle flow for the two components imply that an initial 50-50 D-T mix in the plasma core will move toward a relatively higher fraction of tritium. The physical mechanism for this effect will be discussed in the next section. A curiosity of these results is apparent in the tritium energy transport, $\chi_{\rm T}/\chi_{\rm GBD} = 11.73$, in a 50-50 plasma. This is about a 20% decrease from $\chi_{\rm T}/\chi_{\rm GBD}$ as measured in a pure tritium simulation. However, there is a counterbalancing increase (although smaller in magnitude) in $\chi_{\rm D}/\chi_{\rm GBD}$ from that measured in a pure deuterium simulation.

The addition of electron-ion collisions to the problem reduces the overall particle

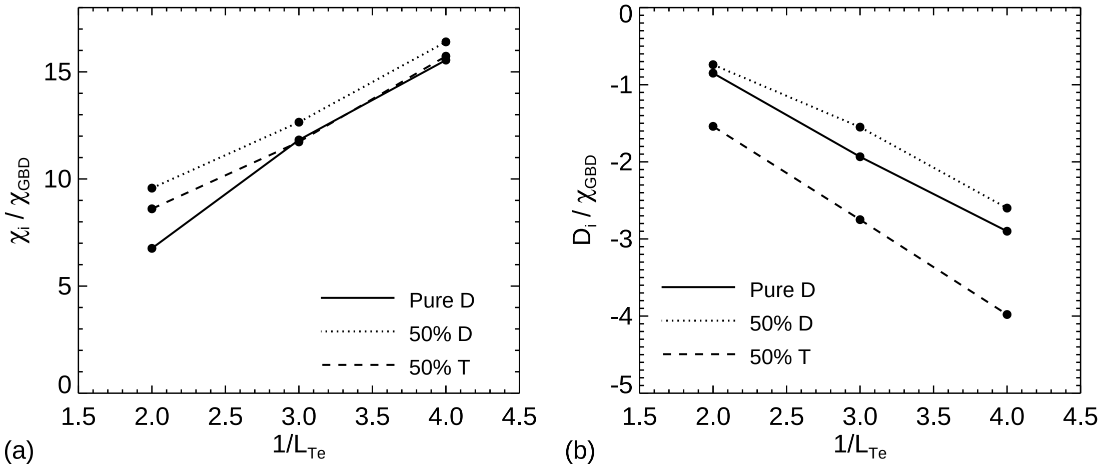

Figure 4.6 Comparison of D-T transport coefficients with those from a pure-D plasma (solid curves). In the two-component DT simulation, we obtain separate transport coefficients for deuterium (dotted curve) and tritium (dashed curve). Plot (a) compares χ while plot (b) compares D. Recall that the normalization, χ_{GBD}, is computed with respect to pure deuterium.

pinch strength but preserves the deuterium-tritium asymmetry. This is illustrated in Fig. 4.7, where a scan over $\eta_e = L_{ne}/L_{Te}$ shows that collisions shift the point of zero particle flow (the pinch null) to higher η_e.

4.7 Analysis

Although a theoretical analysis using the full nonlinear GK equation is evidently impossible, we believe that linear and quasilinear analyses can shed some light on the phenomena described in previous sections. In particular, we are interested in understanding the helium pinch formation, the effect of impurity density gradient and dilution on energy confinement (χ_{eff}), and the asymmetric flow of deuterium and tritium in a 50-50 mixture.

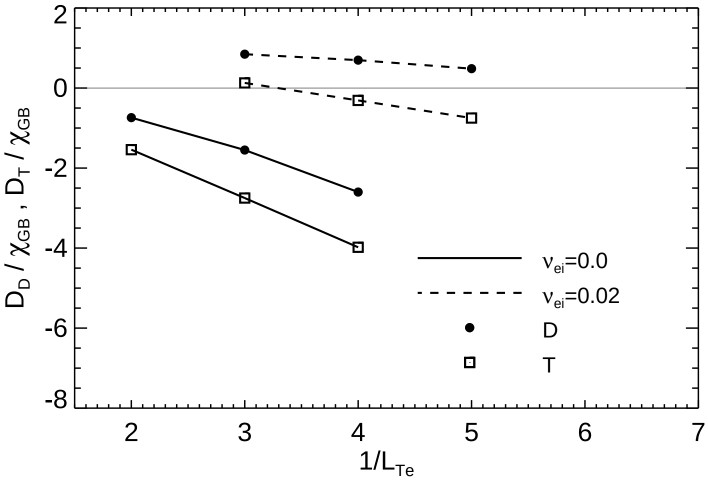

Figure 4.7 Comparison of collisionless and collisional DT simulations for different values of $1/L_{Te}$. As usual the density gradient is fixed ($L_{ne} = 1$) and the electron and ion temperature gradients are equal ($L_{Te} = L_{TD}$).

4.7.1 General theory

For all the calculations we begin from the linear GK equation. As always the unit of length is taken to be a, the unit of time is a/c_s and the unit of velocity is c_s.

$$\mu_\sigma \frac{v_\parallel}{qR}\frac{\partial g_\sigma}{\partial \theta} + (\omega + \omega_{d\sigma})g_\sigma = n_\sigma\left(z_\sigma\omega + \omega_{*\sigma}\right)\, J_0\left(\frac{bv_\perp}{z_\sigma\mu_\sigma}\right)\phi F_M \quad . \tag{4.8}$$

In Eq. (4.8), g_σ is the nonadiabatic part of the perturbed gyrocenter distribution function, n_σ is the ion density, ϕ is the normalized electrostatic potential ($\phi \doteq e\phi^{\rm p}/T_e$, where $\phi^{\rm p}$ is the physical potential), $\mu_\sigma \doteq \sqrt{m_1/m_\sigma}$ is the mass-ratio relative to the main ion, and $b \doteq k_\theta\rho_s\sqrt{1+s^2\theta^2}$ is the FLR parameter. The velocity-dependent drifts are

$$\omega_{*\sigma} \doteq k_\theta\rho_s\left[\frac{1}{L_{n\sigma}} + \left(\frac{v_\perp^2+v_\parallel^2-3}{2}\right)\frac{1}{L_T}\right] \quad , \tag{4.9}$$

$$\omega_{d\sigma} \doteq \frac{2k_\theta\rho_s}{z_\sigma R}\left(\frac{v_\perp^2}{4}+\frac{v_\parallel^2}{2}\right)(\cos\theta + s\theta\sin\theta) \quad . \tag{4.10}$$

Using the conventional $i\delta$ model for electrons, the Poisson (i.e., quasineutrality) equation for two ion species is

$$(1 - i\delta)\, n_e\, \phi = \sum_{\sigma=1,2} z_\sigma \left[-f_\sigma n_e \phi + \int d^3 v J_0 \left(\frac{b v_\perp}{z_\sigma \mu_\sigma} \right) g_\sigma \right] \tag{4.11}$$

$$\doteq \sum_{\sigma=1,2} R_\sigma(\omega)\, n_e\, \phi \tag{4.12}$$

Above, $f_\sigma \doteq z_\sigma n_\sigma / n_e$ is the charge factor such that $f_1 + f_2 = 1$. Also, we have introduced a dimensionless linear response function for the ions, R_σ. Note that the $i\delta$ model assumes electrons which are primarily adiabatic with an added, weak nonadiabatic correction, δ, to induce electron particle flow. Specifically, finite $\delta > 0$ generates an outward electron flow and tend to destabilize electron directed drift waves. In the opposite case, $\delta < 0$ generates an inward flow that tend to stabilize electron directed drift waves. The quasilinear particle fluxes at a given $k_\theta \rho_s$ are written as functions of the R_σ according to

$$\Gamma_\sigma = \mathrm{Re} \left[i k_\theta \rho_s \, |\phi|^2 R_\sigma(\omega) n_e \right] \quad . \tag{4.13}$$

In the quasilinear approximation, we take ω to be the complex linear mode frequency which is the solution of the eigenmode equation resulting from Eq. (4.12). There are various approximate methods for solution of the linear GK equations. For ions, the analysis is greatly simplified by ignoring particle trapping. This approximation, which is equivalent to working in the limit $r/R \ll 0$, is acceptable for realistic parameters and does not significantly alter the effects we are studying. We also ignore the parallel dynamics ($k_\parallel c_s / \omega \to 0$) entirely while exactly retaining the curvature drift resonance. This limit has been examined previously for the case of a pure plasma [98, 88] and will be justified in a subsequent section. Under the indicated assumptions, the response functions can be written as

$$R_\sigma = -z_\sigma f_\sigma + \frac{f_\sigma}{\sqrt{2\pi}} \int_{-\infty}^{\infty} dv_\parallel \, e^{-v_\parallel^2/2} \int_0^\infty v_\perp dv_\perp \, e^{-v_\perp^2/2} J_0^2 \left(\frac{k_\theta \rho_s v_\perp}{z_\sigma \mu_\sigma} \right) \frac{z_\sigma \omega + \omega_{*\sigma}}{\omega + \omega_{d\sigma}} \quad . \tag{4.14}$$

In Eq. (4.14), θ-dependent functions such as $\omega_{d\sigma}$ have been evaluated at $\theta = 0$. In terms of the response functions, the eigenvalue equation becomes

$$-(1 - i\delta) + R_1(\omega) + R_2(\omega) = 0 \quad . \tag{4.15}$$

The double integrals in Eq. (4.14) are straightforward to evaluate numerically, and the eigenvalue problem defined by Eq. (4.15) can be thus solved by application of a root finder. The integral form of the dispersion relation is in fact a very good linear ITG model. To obtain a purely analytic solution, we can expand the integrand in Eq. (4.14) through orders $\mathcal{O}(k_\theta \rho_s)$, $\mathcal{O}(\omega_d/\omega)$, $\mathcal{O}(\omega_d/\omega \times k_\theta \rho_s)$ to yield the response functions

$$R_\sigma = f_\sigma \left\{ \frac{\omega_{*n\sigma}}{\omega} - \frac{\omega_d}{\omega}\left(1 + \frac{\omega_{*p\sigma}}{z_\sigma \omega}\right) - \frac{(k_\theta \rho_s)^2}{\mu_\sigma^2} \times \right.$$
$$\left. \left[\left(1 + \frac{\omega_{*p\sigma}}{\omega}\right) - \frac{3}{2}\frac{\omega_d}{\omega}\left(1 + \frac{\omega_{*p\sigma} + \omega_{*T}}{z_\sigma \omega}\right)\right]\right\} \quad , \tag{4.16}$$

where $\omega_{*n\sigma} = k_\theta \rho_s / L_{n\sigma}$, $\omega_{*T} = k_\theta \rho_s / L_T$, $\omega_{*p\sigma} = \omega_{*n\sigma} + \omega_{*T}$, and $\omega_d = k_\theta \rho_s (2/R)$. Note that ω_d, as defined here, has no species dependence. Despite the seeming complexity of the response functions, the resulting eigenvalue equation is a simple quadratic in ω. We refer to Eq. (4.16) as the "nonresonant" expansion because it neglects the physical effects of the drift resonance.

Finally, by writing $\omega = \omega_R + i\gamma$ and using Eqs. (4.13) and (4.16), the explicit form of the quasilinear particle fluxes at a given $k_\theta \rho_s$ is given by

$$\Gamma_\sigma = k_\theta \rho_s \, |\phi|^2 n_e \frac{\gamma f_\sigma}{|\omega|^2} \left\{ \omega_{*n\sigma} - \omega_d \left(1 + \frac{2\omega_R \omega_{*p\sigma}}{z_\sigma |\omega|^2}\right) - \frac{(k_\theta \rho_s)^2}{\mu_\sigma^2} \times \right.$$
$$\left. \left[\omega_{*p\sigma} - \frac{3}{2}\omega_d \left(1 + \frac{2\omega_R\left(\omega_{*p\sigma} + \omega_{*T}\right)}{z_\sigma |\omega|^2}\right)\right]\right\} \quad . \tag{4.17}$$

4.7.2 Helium pinch formation

We focus on the case $1/L_{n\mathrm{He}} > 0$, which is the more relevant for helium ash transport. In the limit of small helium fraction, it is simple to compute the helium flow in the long-wavelength limit. We are specifically interested in computing the null point of helium flow, and so are interested in the zero of

$$\Gamma_{\mathrm{He}} \propto -\mathrm{Im}\, R_{\mathrm{He}} \sim -f_{\mathrm{He}}\, \mathrm{Im}\left(\frac{\omega_{*n\mathrm{He}} - \omega_d}{\omega} - \frac{\omega_d\, \omega_{*p\mathrm{He}}}{2\,\omega^2}\right) + \mathcal{O}(k_\theta \rho_s)^2 \tag{4.18}$$

We will work in the limit of small δ, f_{He} and $k_\theta \rho_s$. To determine the eigenmode frequency it is sufficiently accurate to solve

$$-(1 - i\delta) + \frac{\omega_{*n\mathrm{D}} - \omega_d}{\omega} - \frac{\omega_{*p\mathrm{D}}\omega_d}{\omega^2} = 0 \quad . \tag{4.19}$$

This expression can be use to write $\mathrm{Im}(1/\omega^2)$ in terms of $\mathrm{Im}(1/\omega)$, yielding a simple equation for the flow null

$$-\mathrm{Im}\, R_{\mathrm{He}} = f_{\mathrm{He}} \left[(\omega_{*n\mathrm{He}} - \omega_d) - \frac{\omega_{*p\mathrm{He}}}{2\omega_{*p\mathrm{D}}} (\omega_{*n\mathrm{D}} - \omega_d) \right] \frac{\gamma}{|\omega|^2} + f_{\mathrm{He}} \frac{\delta}{2} \frac{\omega_{*p\mathrm{He}}}{\omega_{*p\mathrm{D}}} = 0 \ , \qquad (4.20)$$

where $\gamma/|\omega|^2 \sim 1/(\omega_{*p\mathrm{D}}\omega_d)^{1/2}$. For the GA Standard Case parameters, Eq. (4.20) predicts that the flow null will occur at $L_{n\mathrm{He}}/L_{ne} = 0.84$ (the zero of the term in square brackets) in the adiabatic electron limit ($\delta = 0$). To make a comparison with GYRO results, it is useful to perform simulations both with and without adiabatic electrons. This elucidates the particular effect that electron dynamics has on the helium transport, as can be seen in Fig. 4.3. For kinetic electrons (and $f_{\mathrm{He}} = 0.1$) the GYRO flow null occurs at $L_{n\mathrm{He}}/L_{ne} = 1.4$, whereas for adiabatic electrons it occurs at $L_{n\mathrm{He}}/L_{ne} = 2.0$. To understand the source of the discrepancy between the GYRO and analytic values, we solved Eqs. (4.14) and (4.15) numerically. These more accurate equations predict that the flow null is located at $L_{n\mathrm{He}}/L_{ne} = 2.22$ in very good agreement with the adiabatic electron simulations. This lead us to conclude that the discrepancy between the simulation value, $L_{n\mathrm{He}}/L_{ne} = 2.0$, and our analytical prediction, $L_{n\mathrm{He}}/L_{ne} = 0.84$, is due to the omission of curvature drift resonance effects in Eq. (4.16). Nevertheless, from Eq. (4.20), we can still understand the pinch mechanism for which toroidal curvature plays the main role. The term $(\omega_{*n\mathrm{He}} - \omega_d)$ in Eq. (4.20) represents the interplay of curvature and helium drift physics, with curvature driving the pinch. The second term is the back-reaction of the analogous curvature-induced deuterium pinch. That is, as more deuterium flows inwards, some helium must flow out to compensate in order to maintain ambipolarity. Finally, we remark that the nonresonant theory also predicts a helium pinch for $L_{n\mathrm{He}}/L_{ne} > 0.84$, and outward flow for $L_{n\mathrm{He}}/L_{ne} < 0.84$, in qualitative agreement with both kinetic and adiabatic electrons simulations.

4.7.3 Density gradient and dilution effects on energy confinement

The purpose of this analysis is to understand the effect of $1/L_{n\mathrm{He}}$ and f_{He} on χ_{eff}. Scans over a range of f_{He} for two values of $1/L_{n\mathrm{He}}$ are reproduced in Fig. 4.5. From this figure, a puzzle emerges: why do inwardly-peaked impurities ($1/L_{n\mathrm{He}} = 1$) tend to stabilize the plasma while the opposite effect is found for outwardly peaked impurities ($1/L_{n\mathrm{He}} = -1$)? After all, as seen from Eq. (4.3), an increase in f_{He} decreases L_{ni} and consequently η_i when $1/L_T$ is kept fixed. Therefore, based on ITG physics alone, increasing f_{He} should stabilize the plasma in contradiction with our nonlinear results.

In the context of numerical simulations, this issue has been considered previously [35] where a strong coupling between the ITG and impurities is found to be responsible for this behavior, although no details of this coupling is given. To properly diagnose the situation, in what follows, we will compare results from a simple linear eigenvalue equation to GYRO linear calculations. Using the nonresonant expansion, Eq. (4.16), we solve Eq. (4.15) to find growth rates

$$\gamma_{\pm} = \sqrt{\gamma_{\mathrm{pure}}^2 - \frac{f_{\mathrm{He}}\omega_d}{2}\left(\omega_{*T} \pm |\omega_{*n\mathrm{He}}|\right)}\ , \tag{4.21}$$

where

$$\gamma_{\mathrm{pure}}^2 = \frac{4\omega_d\left(\omega_{*ne} + \omega_{*T}\right) - \left(\omega_{*ne} - \omega_d\right)^2}{4} \tag{4.22}$$

is the growth rate when $f_{\mathrm{He}} = 0$. Here, $\omega_{*ne} = k_\theta \rho_s (1/L_{ne})$ and $\omega_d = k_\theta \rho_s (2/R)$. In $\gamma_\pm$ the plus sign refers to the $1/L_{n\mathrm{He}} > 0$ case while the minus sign refers to $1/L_{n\mathrm{He}} < 0$. As before $\mathcal{O}(k_\theta\rho_s)^2$ corrections are neglected. The last formulae imply that $\gamma_- > \gamma_+$ for a given value of dilution according to what is found in [29]. However, these analytic estimates predict $\gamma_{\mathrm{pure}} > \gamma_-$ and $\gamma_{\mathrm{pure}} > \gamma_+$. Although the later is true, the former is in contradiction with linear [35] and nonlinear (Fig. (4.5)) simulations where $\gamma_{\mathrm{pure}} < \gamma_-$. To resolve this discrepancy, we must turn to a more accurate calculation of growth rates.

Table 4.2 describes in detail the assumptions which define each of six separate linear calculations. Here, (1) is the most realistic set of assumptions and (6) the least realistic. Table 4.3 shows the normalized growth rates, for each of the six cases described in Table 4.2, for $1/L_{n\mathrm{He}} = \pm 1$.

In Table 4.3, the results for $1/L_{n\mathrm{He}} = 1$ show agreement in trend with nonlinear simulations (that is, increasing f_{He} stabilizes the plasma). It also shows that trapping plays a minor role [compare (1) and (2)] while $v_\parallel$ has no effect [compare (2) and (3)] justifying the assumptions made for our analytical calculations. For the case of finite-Larmor-radius (FLR) effects we see a stronger variation, but as mentioned before the qualitative behavior is not modified. For the opposite case ($1/L_{n\mathrm{He}} = -1$) a more inter-

Table 4.2 Physical realism of linear, adiabatic-electron calculations summarized in Table 4.3. "Trapping" refers to ion trapping, "parallel motion" to treating $\partial/\partial\theta$ and the θ-dependence of the drifts exactly, "FLR" to full inclusion of finite-larmor-radius effects, and "drift resonance" to a nonperturbative treatment of the curvature drift resonance. RF denotes the "root finder" solution of Eqs. (4.14) and (4.15), while "analytic" refers to Eqs. (4.21) and (4.22).

Model	(1) GYRO	(2) GYRO	(3) GYRO	(4) GYRO	(5) RF	(6) Analytic
Trapping	×					
Parallel motion	×	×				
FLR	×	×	×			
Drift resonance	×	×	×	×	×	

esting behaviour is observed. When all physics effects are included [see (1)] we can see the trend predicted in Fig. (4.5a) where outwardly peaked impurities tend to destabilize the plasma when compared to the pure plasma case. However, as physical effects are removed, the destabilizing trend is almost eliminated for the GYRO simulations [cases (2) to (4)] and the root finder (RF) code [see (5); solution of Eqs. (4.14) and (4.15)]. It is only the analytic result which shows a reversal in the trend [see (6); Eqs. (4.21)] indicating that the effect observed in Fig. (4.5 is mainly caused by the drift resonance (see Eq. (4.14)). Moreover, by comparing the last column of Table 4.3, we see that the direction of the density gradient, $1/L_{n\mathrm{He}}$, does not seem to play as large a role in the instability formation as initially thought. Finally it is worth mentioning that parallel motion and FLR effects play a very small role and therefore their exclusion is justified.

The main conclusion from these results is that although impurities play some direct role, the behavior observed is mostly the result of all the physical mechanisms involved in the problem such as particle trapping, parallel motion, FLR and more important the drift resonance.

4.7.4 DT flow separation

Perhaps the most curious nonlinear simulation result is the observation of an asymmetric flow of deuterium and tritium in a 50-50 mixture. Upon discovering this asymmetry, we then computed quasilinear flow estimates using linear GYRO simulations. We

Table 4.3 Summary of growth rate shift, γ/γ_0, for $1/L_{n\mathrm{He}} = \pm 1$ and $f_{\mathrm{He}} = 0.1, 0.3$, for each of the six models outlined in Table 4.2. Here, γ_0 refers to the growth rate at $f_{\mathrm{He}} = 0$ for a given $1/L_{n\mathrm{He}}$ and model.

$1/L_{n\mathrm{He}}$	f_{He}	(1)	(2)	(3)	(4)	(5)	(6)
1	0.1	0.972	0.970	0.970	0.960	0.967	0.890
1	0.3	0.938	0.930	0.930	0.880	0.911	0.611
-1	0.1	1.028	1.0	1.0	1.001	1.008	0.947
-1	0.3	1.355	1.085	1.085	1.040	1.040	0.829

found that the quasilinear estimates also robustly exhibited the D-T flow asymmetry of the nonlinear simulations, predicting that the tritium flow is directed inward and the deuterium flow of equal magnitude outward. This motivated us to search for a simple analytic expression which could give some physical insight into the symmetry breaking. Setting $z_{\mathrm{D}} = z_{\mathrm{T}} = 1$, and $f_{\mathrm{D}} = f_{\mathrm{T}} = 1/2$, and noting that that response functions have the form

$$R_{\mathrm{D}} = A(\omega) + B(\omega) \quad \text{and} \quad R_{\mathrm{T}} = A(\omega) + \frac{1}{\mu_{\mathrm{T}}^2} B(\omega) \tag{4.23}$$

with $\mu_{\mathrm{T}}^2 = 2/3$, we can write the eigenvalue equation as

$$-(1 - i\delta) + 2A(\omega) + \left(1 + \frac{1}{\mu_{\mathrm{T}}^2}\right) B(\omega) = 0 \tag{4.24}$$

where

$$A(\omega) = \frac{\omega_{*n}}{2\,\omega} - \frac{\omega_d}{2\,\omega}\left(1 + \frac{\omega_{*p}}{\omega}\right) \tag{4.25}$$

$$B(\omega) = -\frac{(k_\theta \rho_s)^2}{2}\left[\left(1 + \frac{\omega_{*p}}{\omega}\right) - \frac{3}{2}\frac{\omega_d}{\omega}\left(1 + \frac{\omega_{*p} + \omega_{*T}}{\omega}\right)\right] \; . \tag{4.26}$$

By demanding that the eigenvalue equation be satisfied, it is easy to show that the imaginary part of the response functions become

$$\operatorname{Im} R_{\mathrm{D}} = -\frac{1}{2}\left(\frac{1}{\mu_{\mathrm{T}}^2} - 1\right) B(\omega) - \frac{\delta}{2} \quad \text{and} \quad \operatorname{Im} R_{\mathrm{T}} = \frac{1}{2}\left(\frac{1}{\mu_{\mathrm{T}}^2} - 1\right) B(\omega) - \frac{\delta}{2} \tag{4.27}$$

In the regime $\omega_{*p} \gg \omega_d \gg (k_\theta \rho_s)^2 \omega_{*p}$, we can compute a crude but illustrative expression for the explicit quasilinear particle flow, as defined by Eq. (4.13), at a given value of

$k_\theta \rho_s$:

$$\Gamma_{\rm D} = n_e (k_\theta \rho_s) |\phi|^2 \left(-{\rm Im}\, R_{\rm D}\right) = +\frac{n_e}{8} (k_\theta \rho_s)^3 \, |\phi|^2 \sqrt{\frac{1}{2}\left(\frac{R}{L_n} + \frac{R}{L_T}\right)} + \frac{n_e}{2}\, \delta\, (k_\theta \rho_s)\, |\phi|^2 \quad , \tag{4.28}$$

$$\Gamma_{\rm T} = n_e (k_\theta \rho_s) |\phi|^2 \left(-{\rm Im}\, R_{\rm T}\right) = -\frac{n_e}{8} (k_\theta \rho_s)^3 \, |\phi|^2 \sqrt{\frac{1}{2}\left(\frac{R}{L_n} + \frac{R}{L_T}\right)} + \frac{n_e}{2}\, \delta\, (k_\theta \rho_s)\, |\phi|^2 \quad . \tag{4.29}$$

The quasilinear result is quite robust, and indicates that in the (adiabatic) limit $\delta = 0$, for any form of the potential (i.e., independent of any mixing-length or similar assumptions) the tritium will flow inward and the deuterium outward at every value of $k_\theta \rho_s$. Note that the total transport coefficient is obtained by summation over the toroidal mode number n in $k_\theta \rho_s = (nq/r)\rho_s$. At finite $\delta > 0$, we observe that the added effect of electron dynamics is to symmetrically drive an outward flow of both species whereas in the opposite case ($\delta < 0$) an inward flow is driven. This shows that, within the accuracy of the $i\delta$-model, the particle flow asymmetry is purely an ion effect.

However, the DT flow separation effect discussed in this section is simply the result of having $f_{\rm D} = f_{\rm T} = 1/2$ and $1/L_{n{\rm D}} = 1/L_{n{\rm T}} = 1$. This in turn makes $A(\omega)$ the same for both species and consequently $B(\omega)/\mu_{\rm T}^2$, which is $\mathcal{O}((k_\theta \rho_s)^2)$, the only source of asymmetry. In the case of a real fusion plasma where the previous equalities may not be satisfied, $A(\omega)$ which is $\mathcal{O}(1)$ and different for deuterium and tritium, will dominate the dynamics of the particle fluxes.

In order to better understand this effect we write $\Gamma_{\rm D} = \Gamma_e/2 + \Delta$ and $\Gamma_{\rm T} = \Gamma_e/2 - \Delta$. For the sake of clarity we consider two cases. The first case looks at $f_{\rm T}$ variations keeping the density gradients fixed and equal ($1/L_{n{\rm D}} = 1/L_{n{\rm T}} = 1$), whereas in the second case we consider $1/L_{n{\rm T}}$ variations with fixed $f_{\rm T} = 1/2$. In both cases electron dynamics is not included ($\Gamma_e = 0$). To complement this analysis we use again the root finder (RF) code (solution of Eqs. (4.14) and (4.15)) used in the previous section. For the first case we find that $\Delta \propto f_{\rm T}$ as expected from ambipolarity constraints and no electron dynamics. In the second case we find a more interesting situation in which the particle flow is controlled by the density gradients of deuterium and tritium. For instance, when the density gradient of tritium is steepened enough, the deuterium flows inward while the tritium flows outward as opposed to the $1/L_{n\mathrm{D}} = 1/L_{n\mathrm{T}}$ case. This effect is reversed when the tritium density gradient is flattened enough. This comes from the fact that Eq. (4.3) is always enforced. The point of zero flow occurs at $1/L_{n\mathrm{T}} = 1.0398$ which indicates that the DT 50-50 effect found is very subtle indeed and that the slightest deviation from equal density gradients can restore equal D and T flows. Nevertheless, the validity of the previous analysis was verified with an additional nonlinear simulation. For this test we decided to steepen the tritium density to $1/L_{n\mathrm{T}} = 1.02$ and flatten the deuterium one to $1/L_{n\mathrm{D}} = 0.98$, while keeping the other paramteres fixed. The particle diffusivity found for the deuterium was $D_{\mathrm{D}} = -1.92 \pm 0.42$, whereas the one for the tritium was $D_{\mathrm{T}} = -2.4 \pm 0.42$, showing that a minimum change in the density gradients is enough to restore equal flows. Notice that in these results the ± 0.42 contribution is a measure of the intermittency of the turbulence and NOT an error bar.

4.7.5 On the accuracy of selected approximations

In attempting to construct an analytic theory of ITG modes which is reasonably accurate for typical tokamak parameters, one soon finds that many of the more popular approaches are rather problematic. Certain models, such as the ubiquitous slab approximation (which sets $\omega_d/\omega = 0$), may often be next to useless. A more sophisticated model which appears in the literature is derived by working to leading order in ω_d/ω, $k_\theta \rho_s$ and $k_\| c_s/\omega$ (the so-called fluid limit) to derive a soluble second-order differential equation for the eigenfrequency [53, 25, 88]. However, in this model, the neglect of resonant curvature drift effects leads to a rather serious error in the phase of the eigenfrequency and is thus a poor approximation for many purposes. For example, the eigenfrequency $\omega = \omega_R + i\gamma$ in the fluid limit tends to be almost purely growing, with $\omega_R \sim 0$. In reality, toroidal ITG modes for the GA Standard Case typically satisfy $|\omega_R| > |\gamma|$. This undesireable feature of the fluid limit is a consequence of the perturbative expansion in ω_d/ω. It turns out that for realistic parameters, it is better to ignore $\mathcal{O}(k_\| c_s/\omega)$ terms completely (thus transforming the problem to an algebraic rather than a differential one) and instead focus on working to higher order (or in fact, nonperturbatively) in ω_d/ω.

By referring to Fig. 4.8, one can see clearly the difference between working to lowest order in ω_d/ω (nonresonant theory) and nonperturbatively in ω_d/ω (resonant theory) for

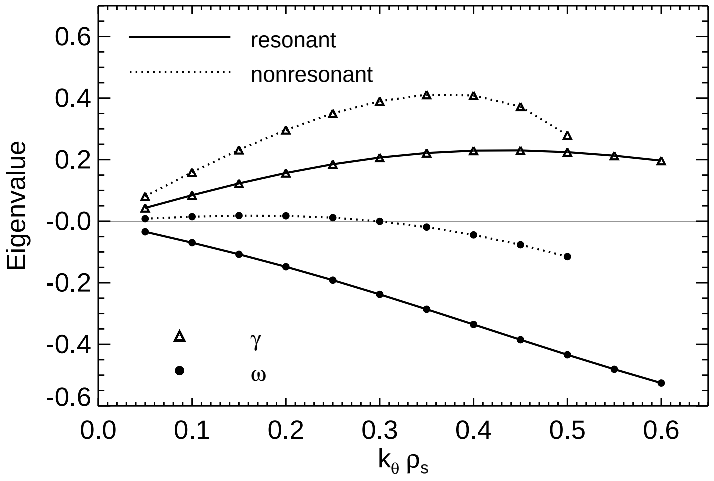

Figure 4.8 Comparison of eigenfrequencies for theory including nonperturbative drift resonance (solid curves) with those from the nonresonant expansion (dotted curves). GA Standard Case parameters for a 50-50 D-T plasma are used.

a D-T plasma. As claimed, the nonresonant theory predicts an eigenfrequency which is almost pure imaginary, while the resonant theory correctly predicts that the mode rotates strongly in the ion direction. To more systematically describe the effects of each approximation, we consider five different calculations of the quasilinear deuterium flow of the previous section. Fig. 4.9a shows the exact value [GYRO (1)] compared with that obtained by neglecting trapping [GYRO (2)] and parallel motion [GYRO (3)] entirely. The salient point is that parallel motion can be safely ignored.

In Fig. 4.9b, it is evident that the resonant integral theory [Theory (1)] agrees extremely well with the GYRO calculation that neglects parallel motion [GYRO (3)]. Thus, we believe the resonant integral theory should be used in any case where an accurate but still tractable model is required. Suprisingly, Fig. 4.9b also shows that the nonresonant theory [Theory (2)] gives a very good description of the quasilinear flow in the low-to-moderate $k_\theta \rho_s$ range. This lends some degree of confidence to the analytic results in Eqs. (4.28) and (4.29).

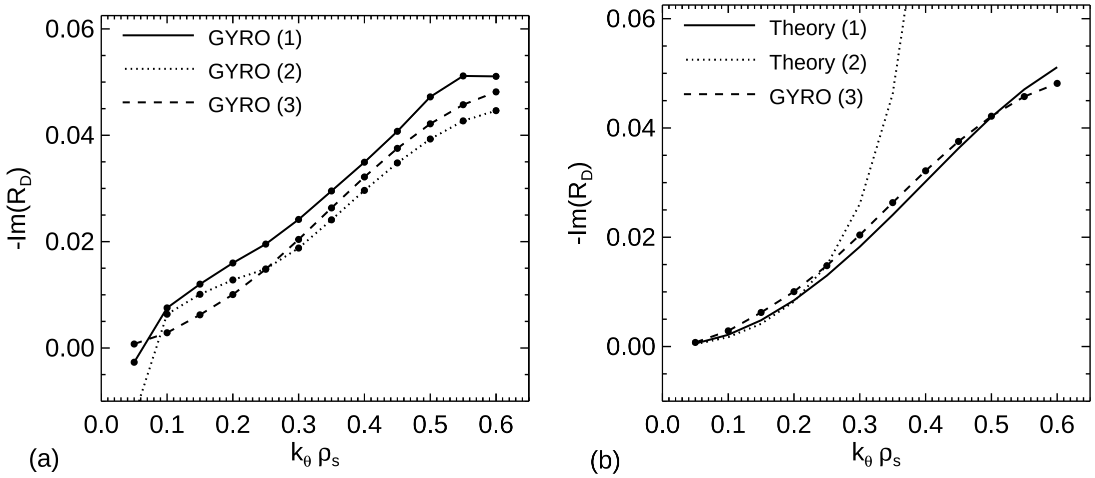

Figure 4.9 Plot (a) compares three GYRO calculations of the quasilinear deuterium flow in a 50-50 D-T plasma for the GA Standard Case. GYRO (1) makes no approximation. GYRO (2) neglects particle trapping by setting $r = 0.05$ (whereas GYRO (1) has $r = 0.5$) and GYRO (3) ignores the parallel motion (ion-sound physics) altogether. Plot (b) compares the GYRO (3) simulation with the full local kinetic theory (Theory 1, which uses Eq. (4.14)) and the long-wavelength local kinetic theory (Theory 2, which uses the simpler Eq. (4.16)).

4.8 Conclusions

The principal results of this chapter can be separated in two categories: plasmas with impurities and isotope flow separation.

In plasmas with impurities, the effects of impurity density gradients and dilution were considered. For moderate values of the helium density gradient, a helium pinch can be created and is driven largely by finite toroidicity (curvature). Further, we found that the direction of the density gradient introduces substantial qualitative and quantitative changes to the plasma. For example, a plasma with impurities peaked in the core has better energy confinement than a plasma with impurities peaked at the edge. Finally, we examined the validity of different approximations to transport in multiple-species plasmas; specifically, the dilution model and lumped-mass approximation. It was found that it is best to approximate an impure plasma with the simplest alternative, a pure plasma, at least when both species are similar (such as for deuterium and helium). Perhaps the most commonly discussed impurity problem is that of a deuterium-carbon plasma, but we have focused on deuterium-helium plasmas because most experiments are done with helium and because the helium ash removal is an important problem for burning plasmas. For the nominal parameters studied in this paper, the deuterium core ions flow inward and the helium impurity ions flow outward, verifying previous experimental observations (Ref. [102], and references therein).

In the second category, reactor-relevant D-T plasmas were analyzed. Contrary to what is normally assumed, the turbulent flows of deuterium and tritium are not equal but show an asymmetry. Starting from an optimal 50-50 mixture, the asymmetry favors the build-up of tritium in the core. A quasilinear model shows that this asymmetry is caused by FLR effects. However, a small steepening of the tritium profile can restore equal flows of D and T.

4.9 Acknowledgement

The text of this chapter, in full, includes material from “Gyrokinetic simulations of ion and impurity transport” [C. Estrada-Mila, J. Candy and R.E. Waltz, Phys. Plasmas **12**, 022305 (2005)]. The dissertation author was the primary researcher.

5

Turbulent Transport of Alpha Particles

5.1 Introduction

The study of energetic particle transport in fusion plasmas has been largely confined to processes connected with (a) magnetohydrodynamic (MHD) oscillations [121, 55], (b) toroidal field ripple [120], or (c) first-orbit loss. In case (a), resonant alpha particles can drive certain MHD modes (typically, toroidal or other Alfvén eigenmodes) unstable. These unstable modes have the potential to, in turn, degrade the alpha particle confinement via stochastic diffusion [18]. In case (b), toroidal field ripple, if it is large enough, can induce a stochastic diffusion of alpha particle banana tips. Case (c) simply corresponds to the birth of alphas whose outer orbit leg is outside the plasma. For instance, some of the most recent developments in this areas have been recently reviewed by Connor [26].

In contrast to the previous processes, the effect of core microturbulence on alpha particle transport has received little attention. Indeed, the "conventional wisdom" is that fast particles do not interact with small scale perturbations because of gyroradius and drift averaging effects [78, 79]. This view is supported by previous experimental studies, although no direct measurements of fluctuation-induced transport have been performed (see Ref. [55] and references therein). Because of that, any conclusion about the interaction of alpha particle and turbulence comes from indirect observations. For example, experimental work done in TFTR [119] showed that the typical alpha gyroradius of approximately 5 cm is substantially larger than the typical perpendicular correlation length of the turbulence ($\sim 1\,\mathrm{cm}$). This scale separation at least supported the speculation that there was no significant alpha interaction with the turbulence. The theoretical work [115, 80], on the other hand, focused on evaluating the effect of orbit averaging in simplified models. Perhaps unsurprisingly, these studies found that alpha transport is reduced when the gyroradius becomes larger. Although quasilinear simulations partially confirmed this view [86], they also shown that in some cases the alpha particle transport was of the same order as that of the background species [87]. A subsequent numerical work, using nonlinear simulations of 2-D Hasegawa-Mima turbulence and test particles [73], found no interaction between energetic species and turbulence.

However, a more recent computational study [101] of single-particle motion using the decorrelation trajectory method discusses the possibility of significant transport of fast ions under certain conditions. Although the results of Ref. [101] show decreasing energetic particle transport at sufficiently large gyroradius (at fixed turbulence levels), the authors suggest that transport at intermediate gyroradii (characteristic of fast ions) can be larger than transport at small gyroradii (characteristic of thermal ions). These provocative results are in qualitative agreement with the results of the present paper. However, the model used in Ref. [101] is quite simplified in that the motion of particles in a homogeneous magnetic field is considered. Results are presented in terms of dimensionless parameters which depend on features of the model stochastic potential. We are not aware of any means by which these dimensionless parameters can be reliably estimated for comparison to the present work.

To perform this research we used a combination of gyrokinetic theory and simulations. For the computational results, we used local (flux-tube) GYRO [20] simulations. Here, we consider alphas in a pure-D plasma for simplicity, under the assumption that pure-D turbulence is similar enough to $D-T$ turbulence. Local simulations rigorously reflect the $\rho_* \to 0$ limit of global simulations [21]. This limit is entirely appropriate since finite-ρ_* corrections, which are weak in existing tokamaks, will be many times smaller in a reactor. We consider only electrostatic fluctuations, and assume unshifted circular geometry, but retain full kinetic electron dynamics. Most importantly, gyrokinetic helium ions (ash or alphas) with complete finite-orbit effects are simulated. In all cases, both helium ions have very low densities such that their effect on the ITG turbulence itself is negligible (trace limit). The key advantage over previous works is the physical realism that the GYRO simulations can provide.

The remainder of this chapter is organized as follows: In Sec. 5.2, a description of the relevant alpha particle physics is presented. This includes a calculation of the equivalent Maxwellian temperature of a slowing-down distribution. In Sec. 5.3, a description of units, conventions and definitions is presented. Sec. 5.4 reports the nonlinear and quasilinear simulations used for this study. A preliminary discussion of the main results is given in Sec. 5.5, which is complemented by the theoretical analysis of Sec. 5.6. This theoretical analysis includes a discussion on the thermal helium pinch, as well as a high-temperature asymptotic theory of helium (alpha) transport. Finally, in Sec. 5.7, we offer a concluding summary.

5.2 Alpha particle physics

5.2.1 Slowing-down form of the alpha particle distribution

One conceptual difficulty for the simulations we will present is the choice of an appropriate distribution function for the energetic particles. In the vicinity of the the birth energy of alpha particles, $E_\alpha = m_\alpha v_\alpha^2/2 \simeq 3.5\,\mathrm{MeV}$, a steady-state slowing-down distribution is the appropriate limiting form. The functional form is obtained by solving the Fokker-Planck (FP) equation with a delta-function source [62]:

$$\frac{\partial F_s}{\partial t} = \frac{1}{\tau_\mathrm{s} v^2}\frac{\partial}{\partial v}\left(v^3 + v_c^3\right) F_s + \frac{S_0}{4\pi v_\alpha^2}\delta(v_\alpha - v) \quad = 0, \tag{5.1}$$

where τ_s is the slowing-down time, v_c is the crossover velocity, v_α is the alpha-particle birth speed (the birth energy is $3.5\,\mathrm{MeV}$), and S_0 is the alpha particle source intensity.

Table 5.1 T_e-dependence of parameters related to the alpha-particle distribution. Here, T_α and λ_α are the equivalent alpha-particle Maxwellian temperatures for each value of T_e.

T_e	v_c/v_α	I_2	I_4	T_α	λ_α
10 keV	0.309	1.185	0.414	815 keV	81.5
15 keV	0.378	0.990	0.380	897 keV	59.8
20 keV	0.437	0.855	0.351	958 keV	47.9
25 keV	0.488	0.753	0.325	1006 keV	40.2
30 keV	0.535	0.673	0.302	1046 keV	34.9

These are defined as

$$\tau_{\rm s} = \frac{3}{16\sqrt{\pi}} \frac{m_e m_\alpha v_e^3}{z_\alpha^2 e^4 n_e \ln\Lambda} \ , \tag{5.2}$$

$$v_c = \left(\frac{3\sqrt{\pi} m_e}{4 m_\alpha} Z_1\right)^{1/3} v_e \ , \tag{5.3}$$

$$S_0 = n_{\rm D} n_{\rm T} \langle \sigma v \rangle_{\rm DT} \ . \tag{5.4}$$

Here, $v_e \doteq \sqrt{2kT_e/m_e}$ is the electron thermal velocity, k is the Boltzmann constant, $\langle \sigma v \rangle_{\rm DT}$ is the thermonuclear D-T reaction rate, and

$$Z_1 = \sum_{i={\rm D,T}} \frac{n_i m_\alpha}{n_e m_i} z_i^2 = \frac{5}{3} \ . \tag{5.5}$$

Solving Eq. (5.1) yields the result

$$F_s(v) = \frac{S_0 \, \tau_{\rm s}}{4\pi} \frac{H(v_\alpha - v)}{v_c^3 + v^3} \ . \tag{5.6}$$

Taking the density moment of F_s provides the connection between particle number, n_α, and source rate:

$$n_{\rm He} = \int_0^\infty (4\pi v^2 dv) F_s(v) = S_0 \, \tau_{\rm s} \, I_2\left(\frac{v_c}{v_\alpha}\right) \ . \tag{5.7}$$

We have introduced the integral

$$I_n(a) \doteq \int_0^1 dx \, \frac{x^n}{a^3 + x^3} \ . \tag{5.8}$$

In what follows, the following formulae will be of use:

$$I_2(a) = \frac{1}{3} \ln\left(\frac{1 + a^3}{a^3}\right) \ , \tag{5.9}$$

$$I_4(a) = \frac{1}{2} - a^2 \left\{ \frac{1}{6} \ln\left(\frac{1 - a + a^2}{(1+a)^2}\right) + \frac{1}{\sqrt{3}} \left[\tan^{-1}\left(\frac{2-a}{a\sqrt{3}}\right) + \frac{\pi}{6} \right] \right\} \ . \tag{5.10}$$

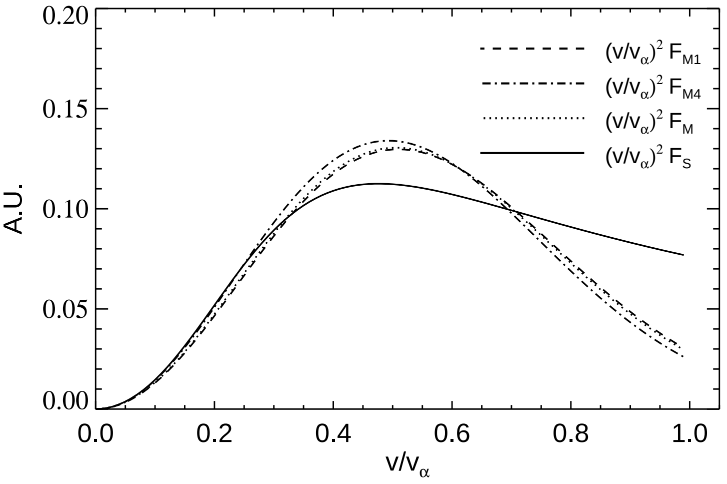

Figure 5.1 Comparison of slowing-down ($F_{\rm S}$) and Maxwellian distributions weighted by v^2 for $T_e = 15\,{\rm keV}$. $F_{\rm M}$ (dotted line) shows a Maxwellian with equivalent temperature given by Eq. (5.14), and used in all our simulations. $F_{\rm M1}$ and $F_{\rm M4}$ denote the resulting ditributions if v-moments and v^4-moments were matched instead.

The form of the distribution in Eq. (5.6) is appropriate for velocities much larger than a thermal velocity. At lower velocities, particles begin to thermalize and build up a Maxwellian (ash) component. We will discuss the issue of ash in more detail later.

5.2.2 An equivalent alpha-particle Maxwellian

Since GYRO is restricted to the simulation of a Maxwellian equilibrium distribution, it is necessary for us to consider the problem of constructing an "equivalent Maxwellian" for the slowing-down distribution of the previous section. We start by writing a Maxwellian distribution, F_M, with a number density n_α

$$F_M = \frac{n_\alpha}{\pi^{3/2}\, v_0^3}\, e^{-v^2/v_0^2} \quad . \tag{5.11}$$

Here, v_0 is a free parameter. To obtain an approximate correspondance between Maxwellian and slowing-down distributions, we compare pressure obtained from the two distribu-

Table 5.2 T_e-dependence of $\lambda_\alpha \doteq T_\alpha/T_e$. Here, $\lambda_\alpha^{(1)}$ and $\lambda_\alpha^{(4)}$ denote the equivalent alpha-particle Maxwellian temperatures obtained by matching v-moments and v^4-moments respectively.

T_e	$\lambda_\alpha^{(1)}$	λ_α	$\lambda_\alpha^{(4)}$
10 keV	80.5	81.5	79.8
15 keV	60.6	59.8	56.7
20 keV	49.3	47.9	44.5
25 keV	41.9	40.2	36.8
30 keV	36.6	34.9	31.6

tions:

$$p_M \doteq \frac{1}{3}\langle m_\alpha v^2 \rangle_M = n_\alpha T_\alpha \ , \tag{5.12}$$

$$p_s \doteq \frac{1}{3}\langle m_\alpha v^2 \rangle_s = \frac{2\,I_4}{3\,I_2}\, n_\alpha E_\alpha \ , \tag{5.13}$$

where $T_\alpha \doteq m_\alpha v_0^2$, and angle brackets denote integration over the indicated distribution. If we equate the two moments, the "equivalent temperature", T_α, of a slowing-down distribution becomes

$$T_\alpha = \frac{2\,I_4}{3\,I_2}\, E_\alpha \ . \tag{5.14}$$

For example, if $T_e = 15\,\text{keV}$, the alpha particles are approximately described by a Maxwellian with temperature $T_\alpha = 897\,\text{keV}$. For convenience, we have tabulated these and other T_e-dependent parameters in Table 5.1. Also, Fig. 5.1 shows a comparison of the two distributions weighted by v^2, when $T_e = 15\,\text{keV}$ (solid and dotted lines). We remark that the definition of an equivalent temperature is not unique. For example, one could have matched v-moments which would have given an equivalent temperature $T_\alpha^{(1)} = (\sqrt{\pi} I_3/2I_2)^2\, E_\alpha$; or v^4-moments with $T_\alpha^{(4)} = \sqrt{4I_6/15I_2}\, E_\alpha$. However, as shown in Fig. 5.1, the resulting distributions are almost insensitive to the choice of moments. The same is true for different T_e as can be seen in Table 5.2, although more noticeable differences can be observed at higher T_e. Finally, it is important to remind the reader the interaction of alphas and turbulence is essentially a spatial one and therefore velocity space instabilities are not relevant.

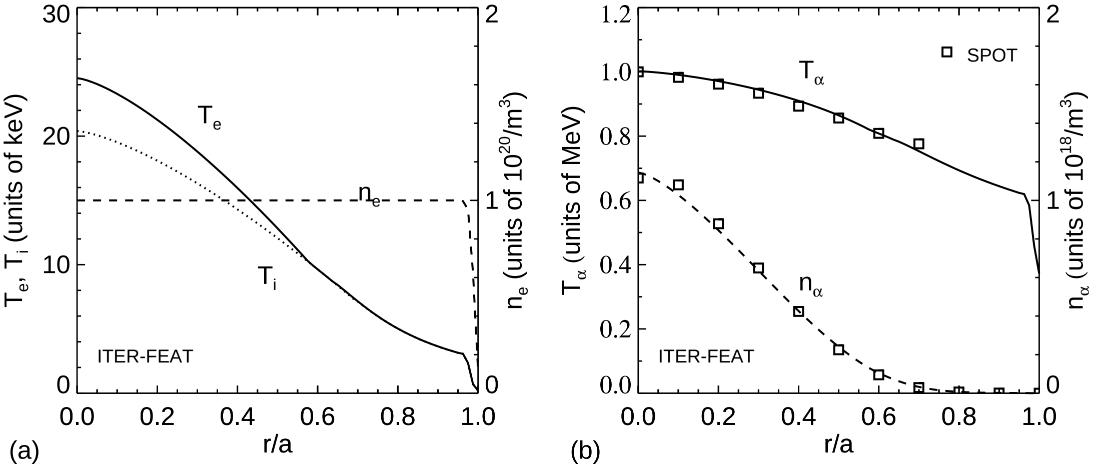

Figure 5.2 ITER-FEAT profile data for electrons and ions (a) and energetic helium (alpha particles) (b). Data in part (b) was computed using Eqs. (5.7) and (5.14) and complemented with SPOT simulations [93].

5.2.3 Alpha particle profiles in ITER

In order to pinpoint the parameter regime of interest, we can compute the relevant alpha-particle profiles as functions of nominal ITER-FEAT [17] parameters. In Fig. 5.2a, we plot temperature and density profiles based on TRANSP analysis [16], but slightly modified in order to accomodate a pedestal. The corresponding energetic helium (alpha) profiles, based on Eqs. (5.7) and (5.14) are plotted in Fig. 5.2b. Focusing on Fig. 5.2b, it is apparent that the helium density (dashed curve) is peaked, owing to the strong T_i-dependence of the source intensity, S_0. However, the helium temperature (solid curve) is a much broader function, because of the relatively weak T_e-dependence of the ratio I_4/I_2. A summary of local energetic helium parameters, based on the profiles in Fig. 5.2, is given in Table 5.3.

Since these profiles were obtained without taking into account finite-orbit-size effects, it is possible that in reality n_α is somewhat broader. To assess this, a more accurate profile was obtained using the SPOT code [93]. SPOT is a Monte Carlo code that follows fast particle guiding centre orbits and can be used to quantify these effects. The results of the simulation are shown on Fig. 5.2b where it can be seen that finite-orbit-size effects are negligible for this set of parameters. The values for $L_{n\alpha}$ and $\eta_\alpha \doteq L_{n\alpha}/L_{T\alpha}$

Table 5.3 Approximate expected local alpha parameters in ITER, ignoring finite-orbit effects.

r/a	λ_α	n_α/n_e	$L_{n\alpha}$	$L_{T\alpha}$	η_α
0.1	42.5	0.0103	0.639	6.18	0.103
0.2	45.6	0.0084	0.421	4.21	0.100
0.3	50.2	0.0064	0.298	3.11	0.096
0.4	57.0	0.0043	0.211	2.31	0.092
0.5	67.4	0.0024	0.146	1.67	0.087
0.6	83.8	0.0010	0.106	1.62	0.065
0.7	105.4	0.0003	0.078	1.22	0.064
0.8	138.0	0.0001	0.062	1.26	0.049

in Table 5.3 can be used as input for nonlinear transport calculations.

5.3 Simulation units and conventions

Unless otherwise specified, the following units and conventions are employed for simulation data. Length is measured in units of the minor radius a, mass in units of the deuterium mass m_D, temperatures in units of T_e (electron temperature) and velocities in units of the deuterium sound speed ($c_s \doteq \sqrt{T_e/m_\mathrm{D}}$). Frequencies and growth rates use a combination of the former and are measured in units of c_s/a. Because diffusivities have a natural gyroBohm scaling, we will generally normalize these to a reference gyroBohm level $\chi_\mathrm{GB} \doteq \rho_s^2 c_s/a$, where $\rho_s \doteq c_s/\Omega_\mathrm{cD}$ is the deuterium-sound Larmor radius and $\Omega_\mathrm{cD} = eB/m_\mathrm{D}$ is the deuterium cyclotron frequency. In these units, the relation between alpha and deuterium gyroradii is given by

$$\rho_\alpha = \frac{\sqrt{\lambda_\alpha}}{z_\alpha \mu_\alpha}\, \rho_s \ , \tag{5.15}$$

where $\lambda_\alpha \doteq T_\alpha/T_e$ and $\mu_\alpha \doteq \sqrt{m_\mathrm{D}/m_\alpha}$.

In this chapter, the symbol σ is used as a species index. Using this convention and the units described above, the particle and energy fluxes, Γ_σ and Q_σ, are related to the particle and energy diffusivities, D_σ and χ_σ, according to

$$\Gamma_\sigma = -D_\sigma \frac{\partial n_\sigma}{\partial r} \quad \text{and} \quad Q_\sigma = -n_\sigma \chi_\sigma \frac{\partial T_\sigma}{\partial r} \ , \tag{5.16}$$

where n_σ and T_σ refer to the equilibrium density and temperature, and r is a flux-surface label (physically, the midplane minor radius). A detailed discussion about the meaning of these fluxes and how they relate to physical units can be found in Appendix A.

The density and temperature gradient scale lengths are $L_{n\sigma} \doteq -[\partial(\ln n_\sigma)/\partial r]^{-1}$ and $L_{T\sigma} \doteq -[\partial(\ln T_\sigma)/\partial r]^{-1}$, respectively. Consequently, a negative density gradient means that particle density increases with radius (outwardly peaked profile), whereas a positive density gradient implies the usual inward-peaked profile.

One difficulty that arises in this problem is how to quantify the interaction bewteen the turbulence and the alpha population, considering the fact that alphas have very different concentrations, gradients and temperatures, when compared with deuterium or electrons. To address this, we decided to compute the alpha fluxes divided by density. We emphasize that the flows (not the diffusivities) are the actual physical quantities that contain ALL the dynamical information about the transport. Dividing the flows by density will therefore yield information about the turbulent transport of each particle. Now, if we normalize these fluxes per particle to their deuterium counterparts we can write

$$\frac{(\Gamma/n)_\alpha}{|\Gamma/n|_\mathrm{D}} \quad \text{and} \quad \frac{(Q/n)_\alpha}{(Q/n)_\mathrm{D}} \ . \tag{5.17}$$

The above ratios are a measure of how strong the turbulent fluxes of helium are compared to the deuterium fluxes. Consequently, they can be used to verify or reject the "conventional wisdom" assumption. This description is valid as long as the deuterium flow is not close to a null.

Finally, for this study the helium charge dilution is defined as $f_\alpha \doteq z_\alpha\,(n_\alpha/n_e)$, where the subscript α refers to the helium ions (alphas or ash).

5.4 GYRO simulations

The linear and nonlinear simulations presented in this paper use the GA Standard case (STD) parameters [111] unless otherwise specified. These are $1/L_{Te} = 1/L_{T\mathrm{D}} = 3$, $1/L_{ne} = 1/L_{n\mathrm{D}} = 1$, $R_0 = 3$, $r = 0.5$, $s = 1$, $q = 2$, $T_e = T_\mathrm{D}$, $\alpha = 0$, $\beta_e = 0$, and $\nu_{ei} = 0$. Although we are interested in physics regimes relevant to reactors, we restrict simulations to a simple two-component plasma with $n_\mathrm{D}/n_e = 0.99$ and trace amounts of

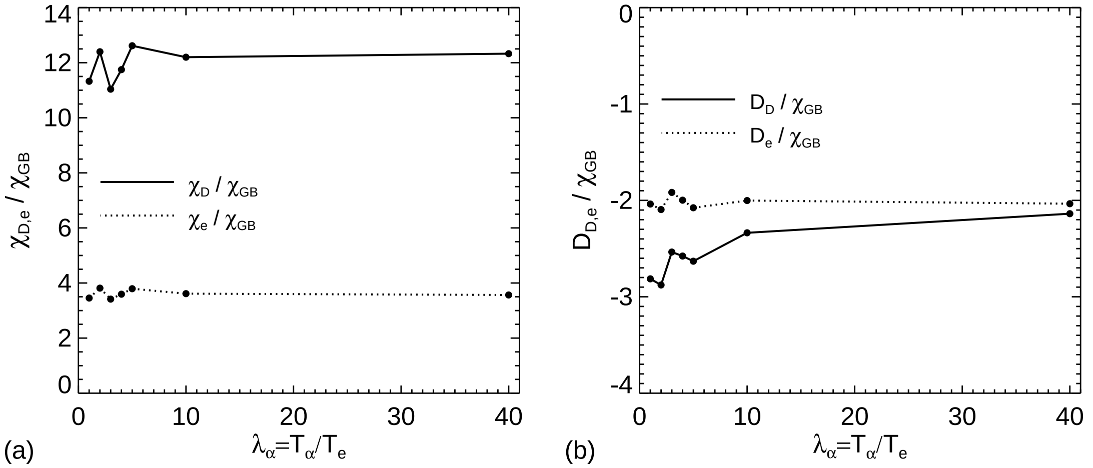

Figure 5.3 Dependence of energy diffusivity (a) and particle diffusivity (b) on the temperature ratio, $\lambda_\alpha = T_\alpha/T_e$, for deuterium and electrons for $\eta_{\rm He} = 0.1$. The helium fraction is $n_\alpha/n_e = 0.005$. Otherwise, GA standard case parameters are used.

helium: $n_\alpha/n_e = 0.005$ (or equivalently, $f_\alpha = 0.01$). For the second ion species (helium) we consider both low- and high-η_α regimes. The low-η_α regime is consistent with the values calculated previously for alphas in ITER. In this case we set $1/L_{T\alpha} = 0.5$ and $1/L_{n\alpha} = 5$ which give $\eta_\alpha = 0.1$. The high-η_α regime, which is more representative of helium ash profiles, was chosen because of extensive experience at this operating point and to make a connection with the previous chapter. Here, we use the same gradients scale lengths as for the deuterium and electrons: $1/L_{T\alpha} = 3$ and $1/L_{n\alpha} = 1$ ($\eta_\alpha = 3$).

Based on the *D*-*T* results of the previous chapter, we do not expect the behavior of the helium impurity to be significantly altered by the assumption of a pure deuterium background. Nonlinear simulations include drift-kinetic electrons with the physical mass ratio: ($m_{\rm D}/m_e \simeq 3600$). Further, we consider only unshifted circular geometry and electrostatic fluctuations. The usual definition of magnetic shear, $s = (r/q)(dq/dr)$, is used, where q is the safety factor.

As explained in the introduction, we are interested in local studies only and thus run GYRO in the flux-tube limit. Standard code resolution for nonlinear simulations uses a 128-point velocity-space grid (8 energies, 8 pitch angles and 2 signs of velocity), and 10 poloidal (orbit) gridpoints per sign of velocity. In the perpendicular directions (x, y), we content ourselves with an $(L_x, L_y)/\rho_s = (128, 128)$ box. Here, x denotes the

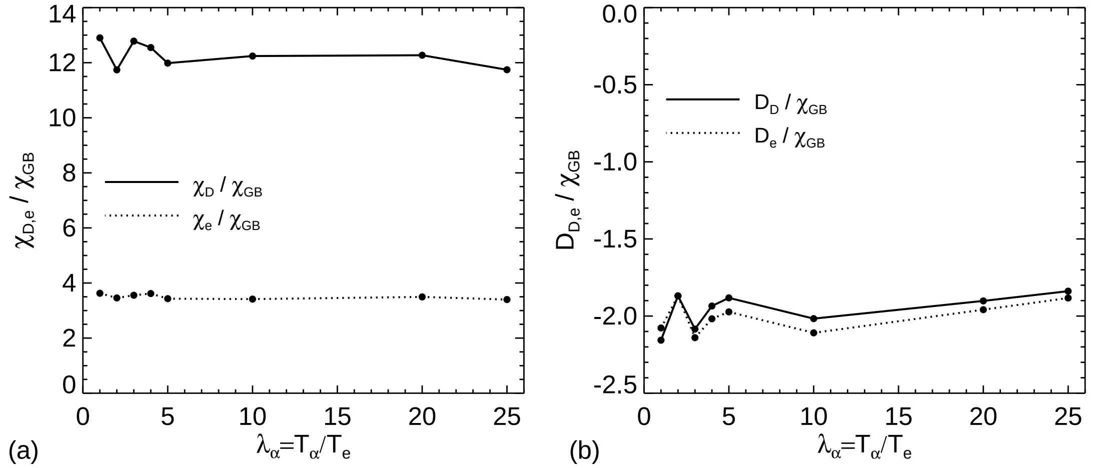

Figure 5.4 Same as previous figure, except $\eta_\alpha = 3.0$.

radial direction, and y denotes the binormal direction such that $L_y = 2\pi/(k_\theta)_{\min}$. In the x-direction we have $n_r = 140$ radial gridpoints (so that $\Delta r/\rho_s = 0.91$). In the y-direction we have $n_n = 16$ complex toroidal modes. With these choices, we resolve up to $(k_\theta)_{\max}\rho_s = 0.75$.

5.4.1 Nonlinear temperature scan

As the helium temperature increases beyond $T_\alpha/T_e = 10$, the simulations require progressively smaller time step in order to resolve an increasingly restrictive α Courant condition. Below $T_\alpha/T_e = 10$, the normal GYRO timestep for kinetic electrons can be used $[(c_s/a)\Delta t = 0.02]$. In addition, the number of radial points in the gyroaverage stencil must grow in order to accomodate the physically larger gyroradius. These issues make simulations at very high temperature prohibitive. For example, a simulation with $T_\alpha/T_e = 40$ was more than 6 times as expensive as $T_\alpha/T_e = 10$.

Taking these considerations into account, we have carried out limited simulations over the range $1 \leq \lambda_\alpha \leq 40$ for $\eta_\alpha = 0.1$ and $1 \leq \lambda_\alpha \leq 25$ for $\eta_\alpha = 3.0$, where $\lambda_\alpha \doteq T_\alpha/T_e$. We remind the reader that $\lambda_\alpha = 1$ corresponds to helium ash (thermalized alphas), whereas $\lambda_\alpha \simeq (82, 35)$ corresponds to fast alpha particles in a plasma with $T_e = (10, 30)\,\text{keV}$.

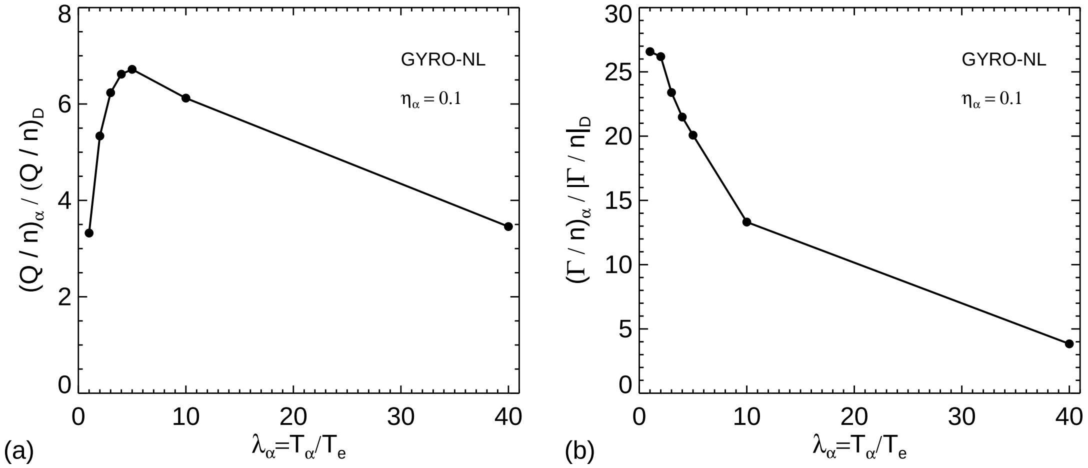

Figure 5.5 Dependence of the normalized helium energy flux (a) and helium particle flux (b) on $\lambda_\alpha = T_\alpha/T_e$. Data is from the same simulations as in Fig. 5.3.

Results for the deuterium and electron diffusivities as a function of λ_α can be seen in Fig. 5.3 and 5.4. Little variation is observed over the indicated range in λ_α due to the small helium concentration. Thus, the presence of the helium impurity does not affect the core turbulence features of both regimes. This will be an important working assumption in the analytic theory which will be presented later.

For the discussion of the helium transport we decided to discuss the different η_α regimes separately.

$\eta_\alpha = 0.1$: Alphas

Figure 5.5a shows that the energy flux increases dramatically up to $\lambda_\alpha = 5$ and then decreases slowly for higher values. However, at large temperatures ($\lambda_\alpha = 40$), the turbulent energy flux of helium is more than three times the flux of the deuterium counterpart. For the case of particle transport we see an analogous effect. As the temperature is increased the strength of the flow decreases rapidly, but despite this reduction the turbulent helium particle transport at high temperatures remains stronger than the deuterium transport.

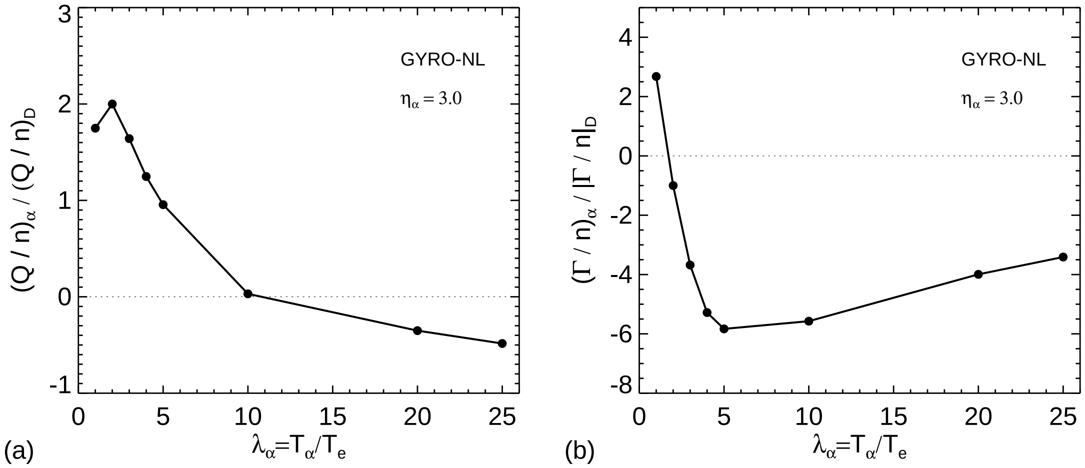

Figure 5.6 Same as previous figure, but the data is from the simulations shown in Fig. 5.4.

$\eta_\alpha = 3.0$**: Ash**

Figure 5.6a shows that the thermal helium ash fluxes ($\lambda_\alpha = 1$) are positive in both cases, as seen in experiments for this type of profiles. However, the energy flux decays rapidly and become negative as λ_{He} increases. In this case the energy flux is weaker than the flux of deuterium, but by no means negligible. For the case of the particle transport, Fig. 5.6b shows that the helium flux becomes negative as well when the temperature is increased, but its strength is more than four times the one of the deuterium when $\lambda_\alpha = 25$. Even though this regime is less relevant for alphas, the results at $\lambda_\alpha = 25$ shows what will happen if the alpha temperature become peaked. Remarkably, in this case, the core turbulence will help prevent energy and particle losses.

5.4.2 Quasilinear GYRO scans

In order to understand some of the nonlinear results presented in the previous subsection we use use a simple type of quasilinear approximation. This is nothing more than evaluating the nonlinear fluxes using the complex linear eigenmodes and eigenfrequencies at a selected $k_\theta \rho_s$. Specifically, the particle flow is the product of the density perturbation ($\tilde{n}$) and the perturbation of the E$\times$B velocity ($\tilde{v}_{\mathrm{E\times B}}$) such that $\Gamma = \tilde{n}\,\tilde{v}_{\mathrm{E\times B}}$. The quasilinear approximation takes $\tilde{n_k} = F(\omega_k)(\tilde{v}_{\mathrm{E\times B}})_k$ for each mode k, where F is a

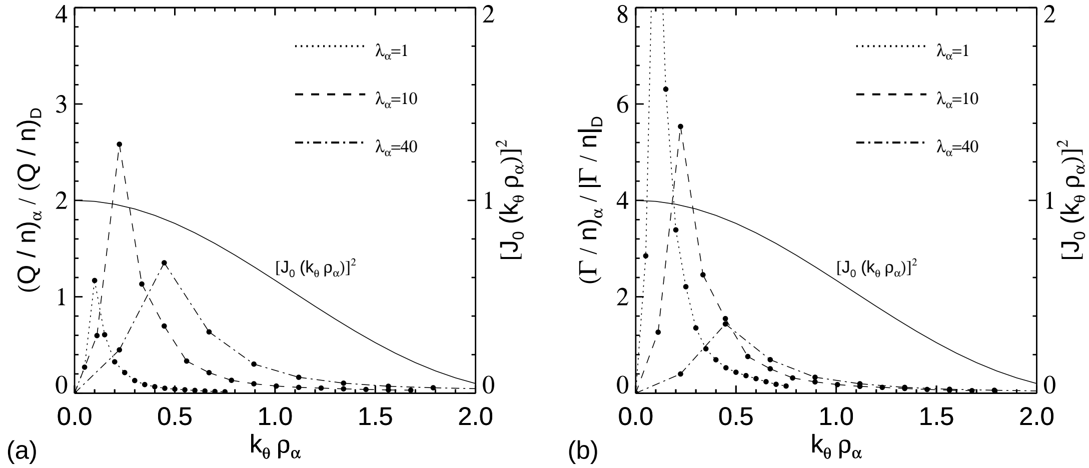

Figure 5.7 Comparison of $k_\theta \rho_\alpha$-dependence of the normalized helium energy flux (a) and helium particle flux (b) for three different temperatures ($\lambda_\alpha = 1, 10, 40$) at $\eta_\alpha = 0.1$. The solid line ($[J_0(k_\theta \rho_\alpha)]^2$) is a measure of gyroaveraging effects.

complex linear function given by the linear response of the density perturbation to the potential perturbation, at the complex linear mode frequency $\omega = \omega_R + i\gamma$. The main advantage of this approach is that simulations are considerably less expensive than their nonlinear counterparts and therefore we can perform numerous scans. It is important to notice that a quasilinear scan can only give a qualitative picture of the turbulence, therefore in order to get realistic (physical) numbers one must always resort to a nonlinear simulation. To determine the validity of the approach in this case, we repeated the same temperature scans for the helium and then we compared it with our previous nonlinear results. For both η_α regimes we chose $k_\theta \rho_s = 0.2$ since as can be seen in Fig. 5.7 the highest contribution to transport occurs at low $k_\theta \rho_s$ for all the temperatures considered. Figures 5.8 and 5.9 show several ratios. The solid curve (GYRO-NL) was obtained by taking the ratio of the respective nonlinear diffusivities shown previously, while the dotted curve (GYRO-QL) represents the quasilinear counterpart. The GYRO-QL data comes from a linear simulation with the same physics as the nonlinear run. The results show a very good agreement for particle transport and moderately good for energy transport in both cases. Two other scans were also performed, one to study the effects of shear and the other one to study the effects of η_α. These are summarized in Fig. 5.10 and 5.11. For the shear ($\eta_\alpha = 3$) we observe noticeable effects on the energy fluxes at

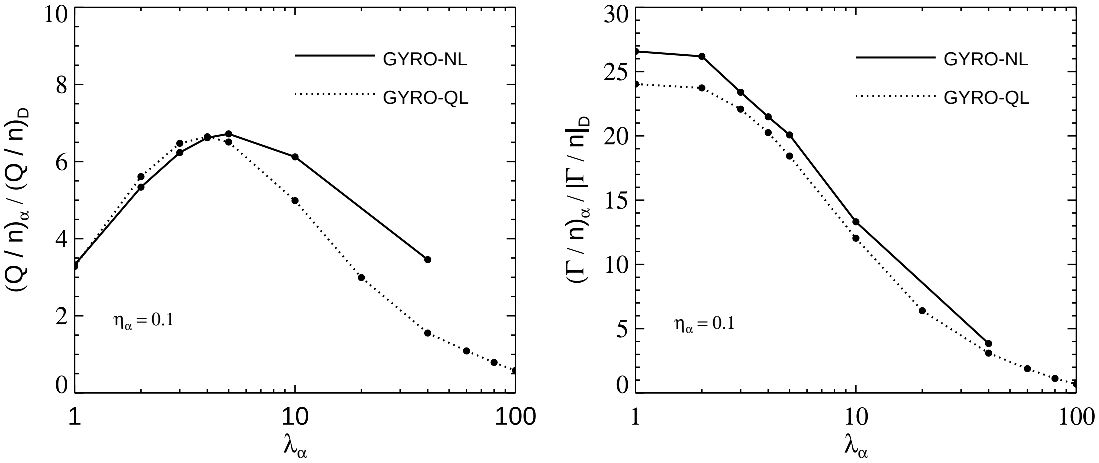

Figure 5.8 Comparison of nonlinear simulation results with quasilinear theory for helium energy fluxes (a) and helium particle fluxes (b) as functions of λ_α. The fluxes are normalized to the deuterium energy flux. Solid curves show full nonlinear simulation results (GYRO-NL), while dotted curves show quasilinear results (GYRO-QL) at fixed $k_\theta \rho_s = 0.2$.

moderate temperatures ($5 \leq \lambda_\alpha \leq 20$), where a reduction of the pinch strength (or a flow reversal in some cases) is found. In the case of particles we only observe changes, characterized by stronger fluxes, for shears below 0.6. A more dramatic situation occurs in the η_α scan. As η_α is decreased both energy and particle fluxes become positive and stronger for the entire temperature range. This effects are not surprising since it is a known fact that η is one of the most important parameters regulating ITG turbulence. This scan was performed by setting $a/L_{T\alpha} = 3.0$ and changing $a/L_{n\alpha}$ with the exception of $\eta_\alpha = 0.1$ where $a/L_{T\alpha} = 0.5$ and $a/L_{n\alpha} = 5.0$. The conclusion is that as the helium density profile becomes more peaked, more outward transport is driven as expected. The importance of these two scans will become more obvious later.

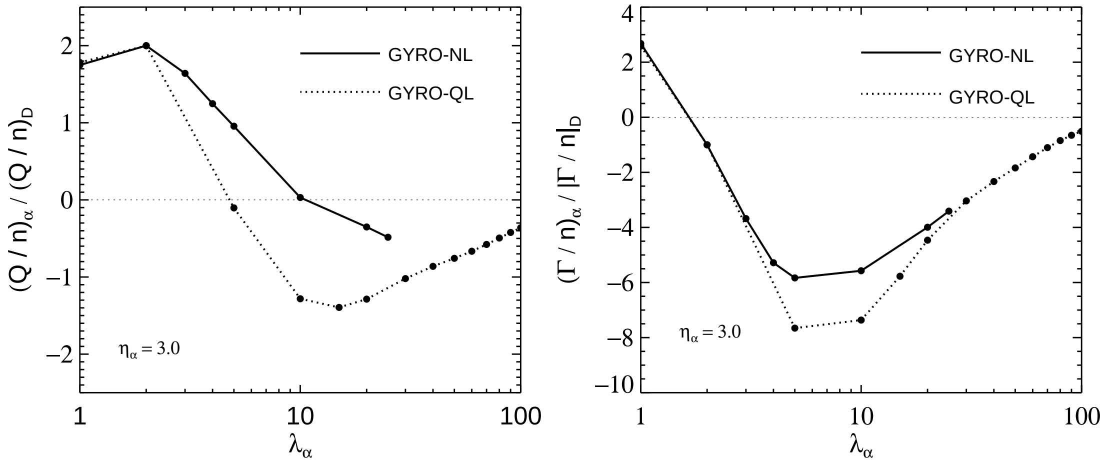

Figure 5.9 Same as previous figure, except $\eta_\alpha = 3.0$.

5.5 Discussion of results

5.5.1 General features and relevance of alpha transport

The results obtained from nonlinear and quasilinear simulations show that there is a strong interaction between alpha particles and turbulence. Although both the alpha energy and alpha particle fluxes per particle are stronger than their deuterium counterparts in most cases, it is the particle transport that exhibits the most noticeable effects. Even though our nonlinear simulations went up to temperatures (λ_α) that are lower than the ones predicted for alpha particles (according to the *equivalent Maxwellian*), if we look at the quasilinear results combined with the temperatures tabulated in Table 5.1, we can see that the transport will still be significant at higher values of λ_α. It is also obvious that as $\lambda_\alpha \to \infty$, the diffusivities $\chi_\alpha, D_\alpha \to 0$. In other words, *conventional wisdom* would apply only if the energy of the species in question is larger compared to E_α. For example, if alphas were born at 7.0 Mev instead of 3.5 MeV, we would get $\lambda_\alpha \sim 120$, which according to Figs. 5.8 and 5.9 will yield no interaction with the turbulence. We would also like to emphasize that we are not seeing unexpected qualitative features. We see the averaging effect that *conventional wisdom* talks about, however when realistic physics are included we see that the averaging is not enough to say that there is no inter-

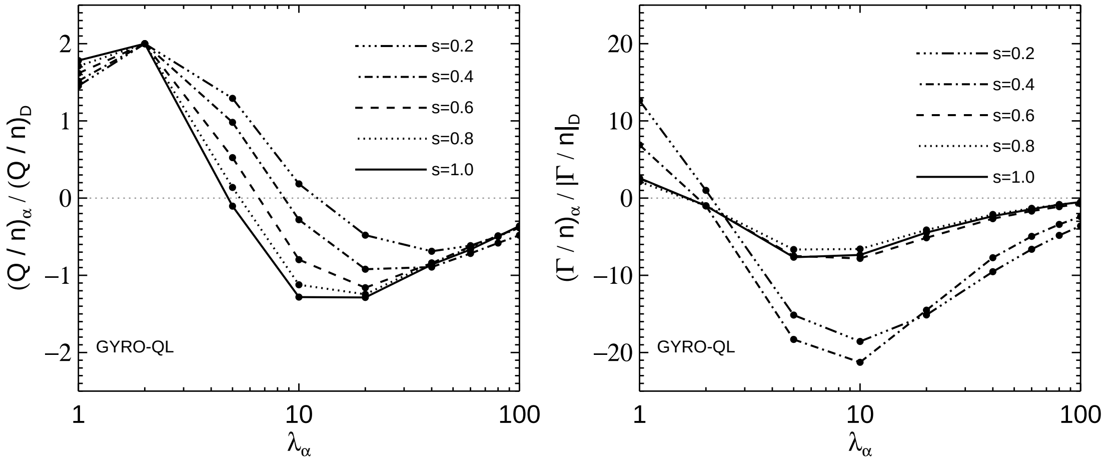

Figure 5.10 Quasilinear scan showing magnetic shear dependence of the helium transport fluxes for $\eta_\alpha = 3.0$.

action between alphas and turbulence. Another point of interest is the case of η_α which determines the direction of the fluxes. For ITER relevant plasmas we expect strongly outward fluxes which eventually can cause the flattening of the alpha density profiles. We also found that for higher values of η_α we can have inward fluxes or pinches of both energy and particles, although this case is more relevant to helium ash.

Another issue we want to address in this paper is the practical relevance of these results. The best way to quantify said relevance is by comparing the resulting alpha fluxes against other fluxes known to be important, such as the TOTAL helium ash fluxes (alpha ash + recycling). Even though this is a global problem, we can still make some conclusions based on our local results. We know from Eq. A.1 that the total fluxes can be written as

$$\Gamma_\sigma = D_\sigma \frac{n_\sigma}{n_e} \frac{a}{L_{n\sigma}} \ , \tag{5.18}$$

$$Q_\sigma = \chi_\sigma \frac{n_\sigma}{n_e} \frac{a}{L_{T\sigma}} \lambda_\sigma \ . \tag{5.19}$$

Typical inputs for alpha particles and their resulting fluxes are tabulated in Table 5.4. Notice that for the diffusion coefficients (D,χ), we extrapolated the results obtained for $\lambda_\alpha = 40$ to the effective alpha temperature ($\lambda_\alpha = 59.8$ for $T_e = 15$ keV) to find $D_\alpha = 0.89$ and $\chi_\alpha = 2.84$. To perform these extrapolations we used some of the analytical results

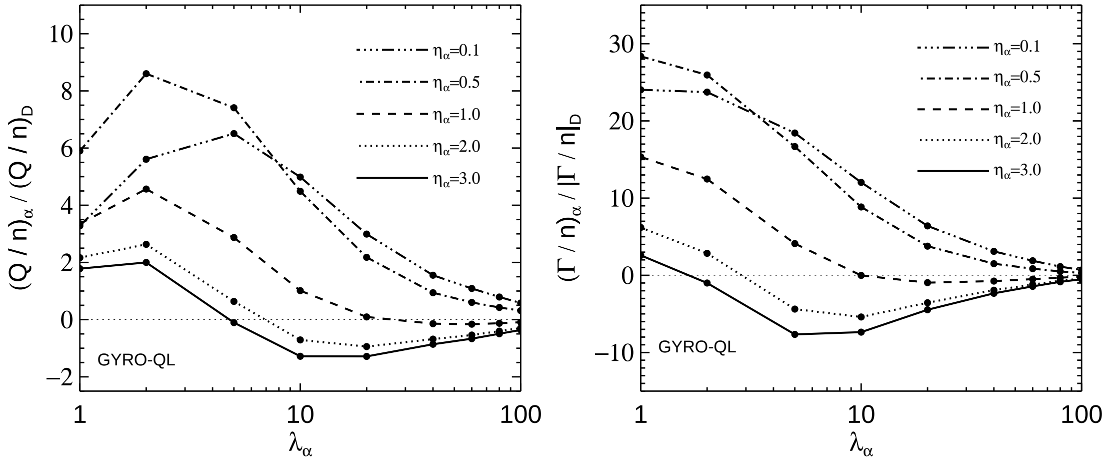

Figure 5.11 Quasilinear scan showing η_α dependence of the helium transport for $s = 1$.

that are presented in the next section. With respect to the total helium ash fluxes, shown in Table 5.4, we used the inputs and results from a previous work [42], which are also consistent with typical reactor parameters. What we see is that although the alpha fluxes are small compared to the total ash fluxes, they are not negligible. The above formulae also highlight the difficulty of measuring the turbulent interaction that was discussed in Sec. 5.3. For instance, knowing that $(D_{\mathrm{D}}, \chi_{\mathrm{D}}) = (-2.13, 12.32)$ and that sometimes diffusivities alone are used to measure the transport, we could have got $D_\alpha/|D_{\mathrm{D}}| \sim 0.42$ or $D_\alpha/\chi_{\mathrm{D}} \sim 0.072$, yielding very different conclusions about the particle transport. A similar, if not more confusing, situation will occur for the energy transport as well. However, the actual physical quantities containing ALL the dynamical information about the transport are the fluxes and not the diffusivities.

The main implication of the above results is that when doing transport modeling of the type discussed in [16], the effect of turbulence on energetic particles should be considered. It is important to emphasize that this is only true for regions with significant levels of turbulence AND alpha particles. To better illustrate this, Fig. 5.12 shows the growth rates for our ITER parameters as a function of the minor radius (r/a). The vertical line shows the reference value $(r/a = 0.5)$ used in all the simulations. As can be seen from the curves, the turbulent interaction is important in the range $(0.4 \leq r/a \leq 0.6)$ where there is turbulence and alpha particles. For $r/a > 0.6$ there are

Table 5.4 Comparison between alpha particles fluxes and total helium ash fluxes (alpha ash + recycling).

Species	n_σ/n_e	$a/L_{n\sigma}$	a/L_{T_σ}	λ_σ	D_σ	χ_σ	Γ_σ	Q_σ
α	0.005	5.0	0.5	59.8	0.89	2.84	0.0225	0.426
He	0.05	1.0	3.0	1.0	4.70	20.05	0.2350	3.0

practically no alphas and for $r/a < 0.4$ the turbulence is almost negligible. The most likely implication from these results is that the alpha population in the core will not be affected by turbulence. However, for $r/a > 0.4$ turbulent effects are expected.

5.5.2 Implications for alpha confinement

Another potential implication of the previous results can be summarized with the following question: Will alphas have enough time to slow down and deposit their energy before the turbulence “expels” them? The classical alpha slowing-down time (τ_s^α) for this type of parameters is of the order of 1 s (0.5 s at $r/a = 0.5$). If we assume $\tau_E \sim \tau_E^{\mathrm{D}}$, where τ_E is the total energy confinement time and τ_E^{D} is the deuterium energy confinement time, we can estimate the alpha energy confinement time (τ_E^α) which can be written as

$$\tau_E^\alpha = \lambda_\alpha \frac{(Q/n)_{\mathrm{D}}}{(Q/n)_\alpha} \tau_E \sim 26\, \tau_E \ . \tag{5.20}$$

The above ratio was computed at the effective alpha temperature ($\lambda_\alpha = 59.8$) and therefore we used the data from Table 5.4. For the deuterium we used $\chi_{\mathrm{D}} = 12.32$, $n_{\mathrm{D}}/n_e = 0.99$, $\lambda_{\mathrm{D}} = 1$ and $a/L_{T\mathrm{D}} = 3.0$. Knowing that the reference energy confinement time in ITER is $\tau_E \sim 6$ s [2], we find that

$$\tau_s^\alpha \ll \tau_E^\alpha \ , \tag{5.21}$$

meaning that alphas will have enough time to slow down. In other words, the alpha pressure profile is expected to be classical. Notice that the high value of τ_E^α is the result of the high energies of the alpha particles. This implies that alphas are so energetic that the rate at which they are losing energy is meaningless, even if it is high compared to the deuterium. However, this is not the case for particle transport. If we compare the alpha particle confinement time (τ_n^α) and the total helium ash confinement time (τ_n^{He})

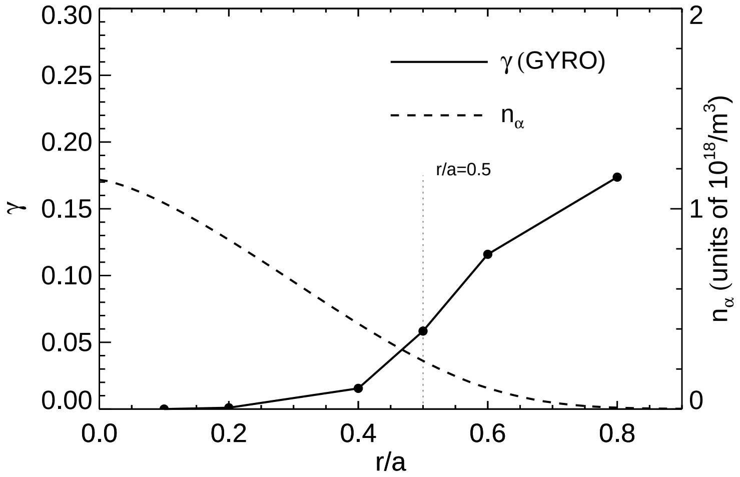

Figure 5.12 Growth rate (γ) and helium density (n_α) as a function of the minor radius (r/a) for ITER parameters. The vertical line shows the reference point ($r/a = 0.5$) used in the simulations.

we get

$$\tau_n^\alpha = \frac{(\Gamma/n)_{\rm D}}{(\Gamma/n)_\alpha}\,\tau_n^{\rm He} \sim \tau_n^{\rm He} \ . \tag{5.22}$$

In the previous chapter we shown that $\tau_n^{\rm He} \sim \tau_E$. This result is also supported by previous experimental [102] studies on helium ash transport. In this case we get

$$\tau_s^\alpha \sim \tau_n^\alpha \ , \tag{5.23}$$

suggesting that the alpha density profile will be slightly non-classical in regions where the turbulence interaction is important. This result would also imply that the temperature profile may also be non-classical. As the alpha density flattens because of the turbulence, the temperature profile will become more peaked, but the pressure profile will remain the same (i.e. classical). Notice that this discussion does not include the effect of helium recycling which is outside the scope of this work.

5.6 Analysis

The quasilinear scans from the previous subsection suggest that it might be possible to further explore some of the previous results using a simple theoretical approach. Although the analysis presented here is general, we chose $\eta_\alpha = 3$ as our test case, because it offers more interesting qualitative features. In particular, we are interested in understanding how the observed pinch is created when the helium temperature is increased, and how rapidly the effect of turbulence on transport decreases at high energies.

5.6.1 General theory

For all analytic calculations we begin from the linear GK equation with no parallel dynamics. This approach closely follows that of the previous chapter, where the reader can find some additional discussion of motivation and validity. Such analysis assumed $\lambda_\sigma = 1$, where $\lambda_\sigma \doteq T_\sigma/T_e$ is the normalized temperature, but has been generalized herein for arbitrary λ_σ. Taking the unit of length to be a, the unit of time to be a/c_s and the unit of velocity to be c_s, we write

$$(\omega + \omega_{d\sigma})g_\sigma = n_\sigma \left(\frac{z_\sigma}{\lambda_\sigma}\omega + \omega_{*\sigma} \right) J_0 \left(\frac{k_\theta \rho_s v_\perp \sqrt{\lambda_\sigma}}{z_\sigma \mu_\sigma} \right) \phi F_M \ . \tag{5.24}$$

In Eq. (5.24), g_σ is the nonadiabatic part of the perturbed gyrocenter distribution function, n_σ is the ion density, ϕ is the normalized electrostatic potential ($\phi \doteq e\phi^{\mathrm{p}}/T_e$, where ϕ^{p} is the physical potential), $\mu_\sigma \doteq \sqrt{m_{\mathrm{D}}/m_\sigma}$ is the mass-ratio relative to the main ion. The velocity-dependent drifts are

$$\omega_{*\sigma} \doteq k_\theta \rho_s \left[\frac{1}{L_{n\sigma}} + \left(\frac{v_\perp^2 + v_\parallel^2 - 3}{2} \right) \frac{1}{L_T} \right] \ , \tag{5.25}$$

$$\omega_{d\sigma} \doteq \frac{2k_\theta \rho_s}{z_\sigma R} \lambda_\sigma \left(\frac{v_\perp^2}{4} + \frac{v_\parallel^2}{2} \right) \ . \tag{5.26}$$

In Eq. (5.24), we have ignored the parallel dynamics (i.e., $\partial_\theta = 0$) and evaluated $\omega_{d\sigma}$ and other poloidally-varying functions at the outboard midplane, $\theta = 0$. This approximation is evidently sensible for modes which are strongly ballooning. Indeed, for the STD case, it is in fact a very good approximation. The validity of this approach, however, is questionable in weak or reversed-shear plasmas, close to threshold, etc. Because of this we performed a quasilinear scan for different values of shear which is summarized in Fig. 5.10. The findings can be divided in two groups. For the case of energy transport the main conclusion is that although shear has a noticeable effect for $5 \leq \lambda_\alpha \leq 40$, it has none at higher temperatures. For the case of particle transport we only see noticeable effects when $s < 0.6$, although the null flow point remains the same. This means that our low energy pinch analysis will be valid for all shears, but our high energy study will be limited to $s > 0.6$. Bearing these caveats in mind, we proceed by writing the Poisson (i.e., quasineutrality) equation for two ion species as

$$\begin{aligned} n_e\,\phi &= \sum_{\sigma=1,2} z_\sigma \left[-\frac{f_\sigma n_e}{\lambda_\sigma}\phi + \int d^3v\, J_0\left(\frac{b v_\perp \sqrt{\lambda_\sigma}}{z_\sigma \mu_\sigma}\right) g_\sigma \right] \qquad (5.27) \\ &\doteq \sum_{\sigma=1,2} R_\sigma(\omega)\, n_e\, \phi \qquad (5.28) \end{aligned}$$

Above, $f_\sigma \doteq z_\sigma n_\sigma / n_e$ is the charge factor such that $f_1 + f_2 = 1$. The result is a remarkably simple eigenvalue equation:

$$-1 + R_1(\omega) + R_2(\omega) = 0 \ . \qquad (5.29)$$

In the present paper, we will find it convenient to decompose R_σ into the form

$$R_\sigma = -\frac{z_\sigma f_\sigma}{\lambda_\sigma} + f_\sigma A_\sigma \ . \qquad (5.30)$$

The quasilinear particle and energy fluxes at a given $k_\theta \rho_s$ are defined as

$$\begin{aligned} \Gamma_\sigma &= f_\sigma \,\mathrm{Re}\left[i k_\theta \rho_s\, |\phi|^2 A_\sigma(\omega)\, n_e \right] \ . \qquad (5.31) \\ Q_\sigma &= f_\sigma \,\mathrm{Re}\left[i k_\theta \rho_s\, |\phi|^2 B_\sigma(\omega)\, n_e T_e \right] \ . \qquad (5.32) \end{aligned}$$

The assumption of no ion trapping allows us to write the functions A_σ and B_σ as

$$\begin{aligned} A_\sigma &= \frac{1}{\sqrt{2\pi}} \int_{-\infty}^{\infty} dv_\parallel \int_0^\infty v_\perp dv_\perp\, e^{-\varepsilon} J_0^2\left(\frac{k_\theta \rho_s v_\perp \sqrt{\lambda_\sigma}}{z_\sigma \mu_\sigma}\right) \frac{z_\sigma \omega/\lambda_\sigma + \omega_{*\sigma}}{\omega + \omega_{d\sigma}} \ , \qquad (5.33) \\ B_\sigma &= \frac{\lambda_\sigma}{\sqrt{2\pi}} \int_{-\infty}^{\infty} dv_\parallel \int_0^\infty v_\perp dv_\perp\, \varepsilon e^{-\varepsilon} J_0^2\left(\frac{k_\theta \rho_s v_\perp \sqrt{\lambda_\sigma}}{z_\sigma \mu_\sigma}\right) \frac{z_\sigma \omega/\lambda_\sigma + \omega_{*\sigma}}{\omega + \omega_{d\sigma}} \ , \qquad (5.34) \end{aligned}$$

where

$$\varepsilon(v_\parallel, v_\perp) \doteq \frac{v_\parallel^2 + v_\perp^2}{2} \ . \qquad (5.35)$$

The extra factor of λ_σ in the formula for B_σ arises because the latter quantity is an energy moment. At this point, the problem is simple enough so that the eigenvalue problem, Eq. (5.29), can be solved using a combination of numerical integration and

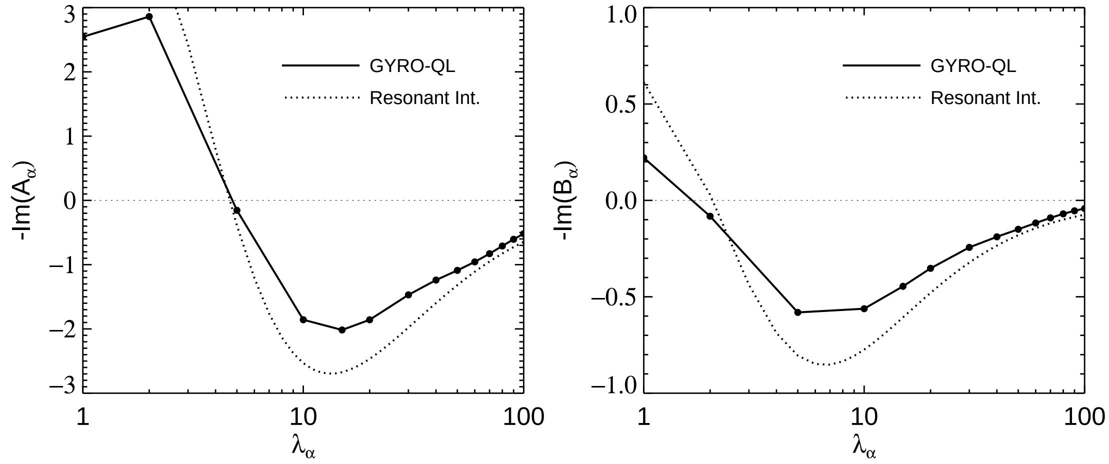

Figure 5.13 Comparison of quasilinear theory with analytic resonant integral theory for helium energy diffusivity (a) and helium particle diffusivity (b) as functions of λ_α.

root finding. We will refer to this method of solution as the *resonant integral* approach. The eigenvalue so obtained can then be substituted into the expressions for Γ_σ and Q_σ to obtain quasilinear estimates for the particle and energy fluxes. A comparison between this approach and quasilinear GYRO simulations can be seen in Fig. 5.13. Beyond this, one can work out asymptotic expansions of A_σ and B_σ to obtain purely analytic estimates for the fluxes. We will pursue both approaches in this paper.

Because we are interested in the dynamics of trace amounts of helium, it is sufficient to consider the perturbative limit for all analytic calculations. That is, we take the eigenmode frequency to be determined by the core ion dynamics only. Operationally, then, we solve the eigenvalue equation $-1 + R_{\rm D}(\omega) = 0$ (i.e, assuming $f_{\rm D} = 1$ and $f_\alpha = 0$) with the STD parameters as defined in Section IV. In Table 5.5 we list a series of eigenvalues for different values of $k_\theta \rho_s$. We will use these results in subsequent asymptotic analyses.

5.6.2 Helium pinch

We know that the helium pinch occurs at low temperatures and therefore work in that limit. If we expand the integrand in Eq. (5.33) through orders $\mathcal{O}(k_\theta\rho_s)$, $\mathcal{O}(\omega_d/\omega)$,

Table 5.5 Eigenvalues for the resonant integral model. Here, STD case parameters are used, assuming $f_\mathrm{D} = 1$ and $f_\alpha = 0$.

$k_\theta \rho_s$	$(a/c_s)\omega_R$	$(a/c_s)\gamma$
0.05	-0.034	0.043
0.1	-0.070	0.085
0.2	-0.146	0.160
0.3	-0.233	0.217
0.4	-0.329	0.250

$\mathcal{O}(\omega_d/\omega \times k_\theta \rho_s)$ we can get a nonresonant expansion for the response functions given by

$$R_\sigma = f_\sigma \left\{ \frac{\omega_{*n\sigma}}{\omega} - \frac{\omega_d}{\omega}\left(1 + \frac{\lambda_\sigma}{z_\sigma \omega}\omega_{*p\sigma}\right) - \frac{(k_\theta \rho_s)^2}{(\mu_\sigma z_\sigma)^2} \times \left[\left(z_\sigma + \frac{\lambda_\sigma}{\omega}\omega_{*p\sigma}\right) - \frac{3}{2}\frac{\omega_d \lambda_\sigma}{\omega}\left(1 + \frac{\lambda_\sigma\left(\omega_{*p\sigma} + \omega_{*T}\right)}{z_\sigma \omega}\right)\right]\right\} \quad , \tag{5.36}$$

where $\omega_{*n\sigma} = k_\theta \rho_s / L_{n\sigma}$, $\omega_{*T} = k_\theta \rho_s / L_T$, $\omega_{*p\sigma} = \omega_{*n\sigma} + \omega_{*T}$, and $\omega_d = k_\theta \rho_s (2/R_0)$. Note that ω_d, as defined here, has no species dependence. Despite the seeming complexity of the response functions, the resulting eigenvalue equation is a simple quadratic in ω. Then, by writing $\omega = \omega_R + i\gamma$ and using Eqs. (5.31) and (5.36), the explicit form of the quasilinear particle fluxes neglecting $\mathcal{O}(k_\theta \rho_s)^2$ is given by

$$\Gamma_\sigma = k_\theta \rho_s \, |\phi|^2 n_e \frac{\gamma f_\sigma}{|\omega|^2} \left\{ \omega_{*n\sigma} - \omega_d \left(1 + \frac{2\omega_R \omega_{*p\sigma} \lambda_\sigma}{z_\sigma |\omega|^2}\right)\right\} \quad . \tag{5.37}$$

Since we are specifically interested in computing the temperature at which the null occurs ($\Gamma_\alpha = 0$), we only need to solve

$$\omega_{*n\alpha} - \omega_d - \frac{2\omega_R \omega_{*p\alpha} \lambda_\alpha}{z_\alpha |\omega|^2} = 0 \quad . \tag{5.38}$$

As said before, to determine the eigenmode frequency it is sufficiently accurate to solve $-1 + R_\mathrm{D}(\omega) = 0$ or in this particular limit

$$-1 + \frac{\omega_{*n\mathrm{D}} - \omega_d}{\omega} - \frac{\omega_{*p\mathrm{D}} \omega_d}{\omega^2} = 0 \quad . \tag{5.39}$$

Solving the previous equation yields an eigenmode frequency given by

$$\omega \sim \frac{\omega_{*n\mathrm{D}} - \omega_d}{2} + i\left(\omega_d \, \omega_{*p\mathrm{D}}\right)^{1/2} \quad , \tag{5.40}$$

Table 5.6 Helium null-flow temperatures (for which $\Gamma_\alpha = 0$) as predicted by different theories. Here, QL refers to a quasilinear simulation (GYRO-QL), RI refers to the resonant integral theory of Eq. (5.42), and NR refers to the nonresonant formula given by Eq. (5.41).

$1/L_{n\alpha}$	$\lambda_\alpha^{\mathrm{QL}}$	$\lambda_\alpha^{\mathrm{RI}}$	$\lambda_\alpha^{\mathrm{NR}}$
0.9	1.85	1.84	1.43
1.0	1.90	2.0	2.0
1.1	2.16	2.16	2.54
1.3	2.42	2.41	3.53

where $|\omega|^2 \sim \omega_d \omega_{*p\mathrm{D}}$. These results give a simple equation for the temperature at which the flow null occurs

$$\lambda_\alpha \sim 2\frac{(1/L_{n\mathrm{D}} + 1/L_{T\mathrm{D}})\,(1/L_{n\alpha} - 2/R_0)}{(1/L_{n\alpha} + 1/L_{T\alpha})\,(1/L_{n\mathrm{D}} - 2/R_0)} \quad . \tag{5.41}$$

For the STD parameters, Eq. (5.41) where $z_\alpha = 2$ is implied, predicts a flow null at $\lambda_\alpha \sim 2$. Comparing to our GYRO results we have that both nonlinear and quasilinear simulation predict a flow null at $\lambda_\alpha \sim 1.9$. The agreement between results is good, however the number obtained with Eq. (5.41) could be just a coincidence for this particular set of paramters, since both density and temperature gradient scale lengths are the same ($1/L_{n\mathrm{D}} = 1/L_{n\alpha}$, $1/L_{T\mathrm{D}} = 1/L_{T\alpha}$). To test the validity of our formula we did some scans varying $1/L_{n\alpha}$. The results are summarized in Table 5.6 where we compared the most realistic quasilinear simulation against the kinetic integral given by Eq. (5.33) and the nonresonant formula found in Eq. (5.41). The agreement between the GYRO simulation is very good when compared with the resonant theory and fair when compared with the nonresonant theory. This suggests that the discrepancy found between our analytical prediction and the simulation values is due to the omission of curvature drift resonance effects in Eq. (5.41). In any case, we can still understand the pinch mechanism since the qualitative agreement between the three approximations is very good. The location of the pinch as a function of the temperature is a consequence of ambipolarity. In this case, as helium flows out some deuterium has to flow in. Finally, in this study the temperature gradient scale lengths were kept the same for simplicity.

5.6.3 Turbulence decay at high energies

The second effect we want to understand is the decay of turbulence at high energies. For this, we need to work out the form of the response function A_α in the limit $\lambda_\alpha \gg 1$. We start by writing the resonant integral, as defined in Eq. (5.33), for the case of helium:

$$A = \frac{1}{\sqrt{2\pi}} \int_{-\infty}^{\infty} dv_\parallel \, e^{-v_\parallel^2/2} \int_0^\infty dv_\perp \, v_\perp e^{-v_\perp^2/2} \, J_0^2\left(\lambda^{1/2} k_\theta \rho_s \, v_\perp/\sqrt{2}\right) \times \\ \frac{2\omega/\lambda + \omega_* \left[1 + \eta(v_\perp^2 + v_\parallel^2 - 3)/2\right]}{\omega + \lambda \, \omega_d \left(v_\parallel^2 + v_\perp^2/2\right)/4} \;, \tag{5.42}$$

In Eq. (5.42) and in the remainder of this section, we have supressed the α label in all subscripts for brevity, and have explicitly set $z_\alpha = 2$ and $\mu_\alpha = 1/\sqrt{2}$. For clarity, we remind the reader of the remaining abbreviations: $\lambda_\alpha \to \lambda$, $\omega_* \to k_\theta \rho_s / L_{n\alpha}$, $\omega_d \to k_\theta \rho_s (2/R_0)$, and $\eta \to L_{n\alpha}/L_{T\alpha}$.

Although previous works on ITG dynamics [98, 88] usually set $v_\parallel^2 = v_\perp^2/2$ in order to capture the resonant denominator (∇B model), we prefer a simple but exact transformation to reduce the 2-dimensional resonance to a 1-dimensional form. Writing

$$v_\perp = \sqrt{2} r \sin\beta \tag{5.43}$$

$$v_\parallel = r \cos\beta \tag{5.44}$$

the integral becomes

$$A = \omega_* \sqrt{\frac{2}{\pi}} \int_0^\pi d\beta \sin\beta \int_0^\infty dx \, x^2 e^{-x^2(1+\sin^2\beta)/2} \, \frac{J_0^2\left(\lambda^{1/2} x \, k_\theta \rho_s \, \sin\beta\right)}{\omega + \lambda x^2 \, \omega_d/4} \times \\ \left[\left(1 - \frac{3\eta}{2}\right) + \frac{\eta x^2}{2}\left(1 + \sin^2\beta\right) + \frac{2\omega}{\lambda\omega_*}\right] \;. \tag{5.45}$$

At this point it is important to point out that the asymptotic expansions of the real and imaginary parts of the integral above differ in an important way. For any complex number $\hat{\omega} \doteq \hat{\omega}_R + i\hat{\gamma}$, such that $u \in \mathbb{R}$, we can write

$$\mathrm{Im}\left(\frac{1}{\hat{\omega} + u}\right) = \frac{-\hat{\gamma}}{(u + \hat{\omega}_R)^2 + \hat{\gamma}^2} \sim -\frac{\hat{\gamma}}{u^2} \quad \text{as} \quad u \to \infty \tag{5.46}$$

This means that the x-integral in Eq. (5.45) will converge even if the exponential factor is neglected. Then, we anticipate that the dominant contribution to the integral will come from small x in the region $x \sim \lambda^{-1/2}$, and therefore order

$$1-\frac{3\eta}{2} \gg \frac{\eta x^2}{2}\left(1+\sin^2\beta\right) , \ \frac{2\omega}{\lambda\omega_*} \quad . \tag{5.47}$$

Thus, we are motivated to change variable to $u \doteq \lambda x^2/4$, and define $\hat{\omega} \doteq \omega/\omega_d$ to find

$$-\mathrm{Im}\, A \sim \frac{4}{\lambda^{3/2}}\frac{\omega_*}{\omega_d}\left(1-\frac{3\eta}{2}\right)\sqrt{\frac{2}{\pi}}\int_0^\infty du\, \frac{\hat{\gamma}\, u^{1/2}}{(u+\hat{\omega}_R)^2+\hat{\gamma}^2}\, S(u,k_\theta\rho_s) \quad . \tag{5.48}$$

where S has the form

$$S(u,k_\theta\rho_s) \doteq \int_0^\pi d\beta\, \sin\beta J_0^2\left(2k_\theta\rho_s u^{1/2}\sin\beta\right) \quad . \tag{5.49}$$

This form of the result makes it clear that the helium (alpha) particle flux decays as $\lambda^{-3/2}$, independent of the value of $k_\theta\rho_s$. A comparison of the asymptotic form, Eq. (5.48), with the full resonant integral, Eq. (5.42) – or equivalently, Eq. (5.45) – is shown in Fig. 5.14.

It is of interest to do the remaining integrals analytically by taking the subsidiary limits $k_\theta\rho_s \to 0$ and $k_\theta\rho_s \to \infty$. First, when $k_\theta\rho_s \to 0$, a simple (keyhole) contour integration yields

$$-\mathrm{Im}\, A \sim \frac{2}{\lambda^{3/2}}\sqrt{\frac{2}{\pi}}\frac{\omega_*}{\omega_d}\left(1-\frac{3\eta}{2}\right) 4\pi\, \mathrm{Re}\sqrt{-\hat{\omega}} \quad . \tag{5.50}$$

This form is compared with more exact results in Fig 5.14a. In the opposite limit $k_\theta\rho_s \to \infty$, a large-argument expansion of the Bessel function produces

$$-\mathrm{Im}\, A \sim \frac{2}{\lambda^{3/2}}\sqrt{\frac{2}{\pi}}\frac{\omega_*}{\omega_d}\left(1-\frac{3\eta}{2}\right)\left[\frac{\pi}{2}+\arctan\left(\frac{-\hat{\omega}_R}{\hat{\gamma}}\right)\right]\frac{1}{k_\theta\rho_s} \tag{5.51}$$

This form is compared with more exact results in Fig 5.14c.

In the case of the energy transport, we must work out the large-λ expansion for B. Here, we focus exclusively on the limit $k_\theta\rho_s \to 0$ (equivalently, the drift-kinetic limit). This is easily justified by looking again at Fig 5.7a which shows that most of the transport comes from $k_\theta\rho_\alpha < 1$ or equivalently $k_\theta\rho_s < z_\alpha\mu_\alpha/\sqrt{\lambda_\alpha} \ll 1$. Unlike the expansion scheme for A, in this case the dominant contribution to the integral comes from $x \sim 1$ rather than $x \sim \lambda^{-1/2}$. The result is

$$-\mathrm{Im}\, B \sim \frac{4}{\lambda}\frac{\hat{\gamma}\,\omega_*}{\omega_d^2}\left(1+\frac{\pi}{2}\right)(1-\eta) \quad . \tag{5.52}$$

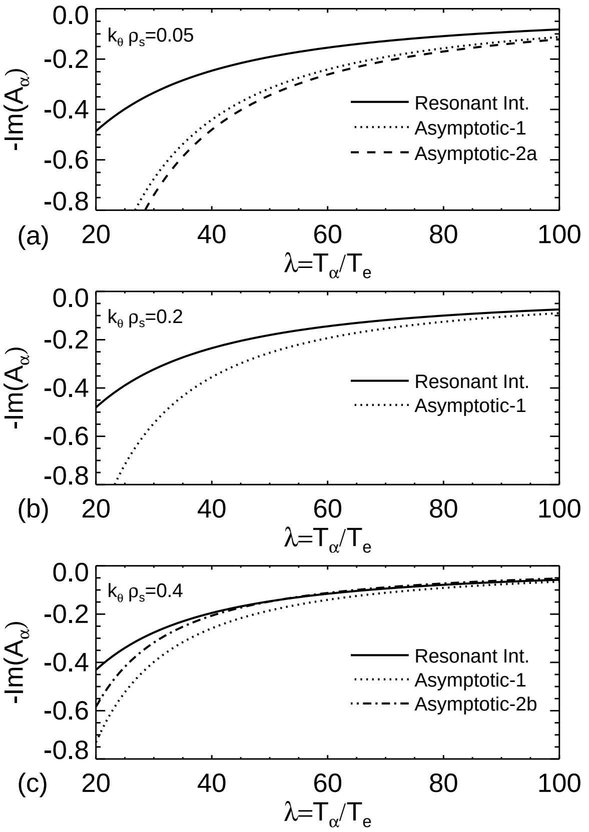

Figure 5.14 Large-λ_α form of the energetic helium (alpha-particle) response function for $k_\theta \rho_s = 0.05$ (a), $k_\theta \rho_s = 0.2$ (b), and $k_\theta \rho_s = 0.4$ (c). Solid lines show the full resonant theory as defined in Eq. (5.42), and dotted lines show the $\lambda^{-3/2}$-theory of Eq. (5.48). We have plotted the low-$k_\theta \rho_s$ formula, given by Eq. (5.50, as a dashed curve in (a). Similarly, we have plotted the high-$k_\theta \rho_s$ formula, given by Eq. (5.51), in (c).

5.7 Conclusions

The principal results of this study can be separated in two groups: alpha particle and turbulence interaction and relevance of turbulent alpha particle transport.

For the interaction of alpha particle and turbulence we found that contrary to "conventional wisdom" (which usually neglects it) there is a strong interaction for typical α-parameters in ITER. Curvature drift plays the main role in the coupling as can be seen from Eqs. (5.33) and (5.34). For particle transport the flow magnitude decays as $\lambda_\alpha^{-3/2}$. We estimate that as long as $\eta_\alpha > 2/3$ the flow remains negative or pinched. For energy transport the energy flux decays as λ_α^{-1}. A surprising finding is that for $\eta_\alpha > 1$, the energy flux is inward (pinched).

Concerning the relevance of alpha particle transport we discovered that although the alpha population is expected to be very small, its turbulent fluxes are significant even when compared to the total helium fluxes resulting from energetic ions and recycling. This suggests the necessity to introduce turbulent effects for said particles in transport modelling calculations, in regions where the turbulence levels and the alpha population are significant.

5.8 Acknowledgement

The text of this chapter, in full, includes material from "Turbulent transport of alpha particles in reactor plasmas" [C. Estrada-Mila, J. Candy and R.E. Waltz, submitted to Nucl. Fusion (2006)]. The dissertation author was the primary researcher.

6

Conclusions

In this thesis we have presented a systematic study of particle transport in tokamaks. The principal results of this investigation can be classified into three main categories: *particle transport in a pure plasma*, *particle transport in impure plasmas* and *turbulent transport of alpha particles* .

In the first category we studied pure plasmas and found that the temperature gradient plays the dominant role in the pinch formation, whereas electron collisions generally oppose the production of such pinch. We also addressed the problem of density peaking using global simulations of L-mode DIII-D discharges, and found the existence of a pinch under experimental conditions. These results reconcile the apparent discrepancies between anomalous pinches and collisionality, and supports our hypothesis that fully realistic simulations are crucial to the reliable calculation of experimental flows.

In the second category we investigated plasmas with two ion species. First, we consider the case of helium ash transport and found that for moderate values of the helium density gradient, a helium pinch can be created and driven by finite toroidicity. Further, we found that the direction of the density gradient introduces substantial qualitative and quantitative changes to the plasma. For example, a plasma with impurities peaked in the core has better energy confinement than a plasma with impurities peaked at the edge. We also examined the validity of different approximations to transport in multiple-species plasmas. It was found that it is best to approximate an impure plasma with the simplest alternative, a pure plasma, at least when both species are similar (such as for deuterium and helium). Second, we studied reactor-relevant D-T plasmas and discover that the turbulent flows of deuterium and tritium are not equal but show an asymmetry. However, a quasilinear model showed that this asymmetry is caused by FLR effects, and that a small steepening in one of the profiles can restore equal flows of D and T.

In the third category we analyzed the interaction between alpha particles, which have a large gyroradius, and turbulence. We found that contrary to "conventional wisdom" there is a strong interaction for typical reactor parameters, with curvature drift effects playing the main role in the coupling. We also discovered that although the alpha population is expected to be very small, its turbulent fluxes are not negligible even when compared to the total helium fluxes resulting from energetic ions and recycling. This suggests the necessity to introduce turbulent effects for said particles in transport modelling calculations, in regions where the turbulence levels AND the alpha population are significant.

A

Units and Conventions

Unless otherwise specified, the choice of units and conventions follows closely the ones used in the GYRO code [20].

A.1 Units

The choice of basic units is summarized in Table A.1. All other units are constructed by using a combination of them. For example, frequencies and growth are measured in units of c_s/a.

A.2 Diffusivities and Fluxes

Diffusivities are normalized to a reference gyroBohm level $\chi_{\mathrm{GB}} \doteq \rho_s^2 c_s/a$, where $\rho_s \doteq c_s/\Omega_{ci}$ is the ion-sound Larmor radius and $\Omega_{ci} = z_i eB/m_i$ is the ion cyclotron frequency.

In the units described above, the particle and energy fluxes, Γ_σ and Q_σ where σ is a species label, are related to the particle and energy diffusivities, D_σ and χ_σ, according to

$$\Gamma_\sigma = -D_\sigma \frac{\partial n_\sigma}{\partial r} \quad \text{and} \quad Q_\sigma = -n_\sigma \chi_\sigma \frac{\partial T_\sigma}{\partial r} \ . \tag{A.1}$$

Γ_σ and Q_σ are computed as the magnetic-flux-surface-, time- and radial-averages of the primitive fluxes computed from the gyrokinetic equations. Converting quantities back

Table A.1 Summary of basic units.

Dimension	Unit	Description
Length	a	Minor radius
Mass	m_1	Primary ion mass
Velocity	c_s	Ion sound speed $\sqrt{T_e/m_1}$
Time	a/c_s	
Temperature	T_e	Electron temperature

to physical units is straightforward; for example, the physical radius is $a \times r$, the physical flux is $c_s \times \Gamma_\sigma$ and the physical diffusivity is $c_s \times a \times D_\sigma$. Density and temperature are in physical units.

A.3 Gradient scale lengths

The density and temperature gradient scale lengths are written as

$$L_{n\sigma} \doteq -\left[\frac{\partial(\ln n_\sigma)}{\partial r}\right]^{-1} \quad \text{and} \quad L_{T\sigma} \doteq -\left[\frac{\partial(\ln T_\sigma)}{\partial r}\right]^{-1} \quad . \tag{A.2}$$

Consequently, a negative density gradient means that particle density increases with radius (outwardly peaked profile), whereas a positive density gradient implies the usual inward-peaked profile.

B

The $s - \alpha$ equilibrium in Shafranov Coordinates

The best alternative to describe the $s - \alpha$ equilibrium [28], which consists of shifted circular flux surfaces and large aspect ratio, is by using Shafranov coordinates. More specifically, we can write

$$R = R_0 + r\cos\theta - \Delta(r) \ , \tag{B.1}$$

$$\xi = \ -\varphi \ , \tag{B.2}$$

$$Z = r\sin\theta \ , \tag{B.3}$$

where R_0 is the major radius, r is the minor radius and $\Delta(r)$ is the Shafranov shift. The variables ξ and θ denote toroidal and poloidal angles respectively as can be seen in Fig. B.1. The connection with the remaining cartesian coordinates (x, y) follows directly and it is given by

$$x = R\cos\xi \quad \text{and} \quad y = R\sin\xi \ . \tag{B.4}$$

In this geometry we can define a covariant basis

$$\hat{\mathbf{e}}_r \doteq \frac{\partial \mathbf{r}}{\partial r} \quad , \qquad \hat{\mathbf{e}}_\theta \doteq \frac{\partial \mathbf{r}}{\partial \theta} \qquad \text{and} \qquad \hat{\mathbf{e}}_\xi \doteq \frac{\partial \mathbf{r}}{\partial \xi} \ , \tag{B.5}$$

where $\mathbf{r} = (x, y, Z)$. We can also define a contravariant basis given by

$$\hat{\mathbf{e}}^r \doteq \nabla r \quad , \qquad \hat{\mathbf{e}}^\theta \doteq \nabla\theta \qquad \text{and} \qquad \hat{\mathbf{e}}^\xi \doteq \nabla\xi \ . \tag{B.6}$$

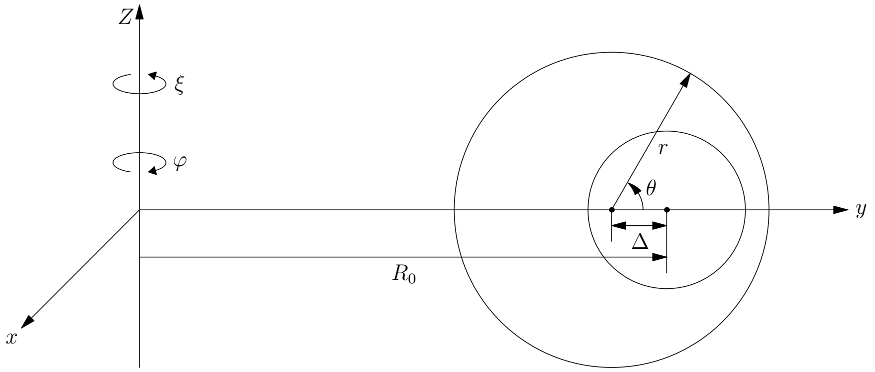

Figure B.1 $s-\alpha$ equilibrium in Shafranov Coordinates.

With this information we can write the covariant and contravariant components of the metric tensor g as

$$g_{ij} = \hat{\mathbf{e}}_i \cdot \hat{\mathbf{e}}_j \quad \text{and} \quad g^{ij} = \hat{\mathbf{e}}^i \cdot \hat{\mathbf{e}}^j \ , \tag{B.7}$$

where the indices i and j refer to r, θ and ξ. Writing each covariant component explicitly gives

$$g_{ij} = \begin{bmatrix} 1-2\Delta'\cos\theta+(\Delta')^2 & \Delta' r\sin\theta & 0 \\ \Delta' r\sin\theta & r^2 & 0 \\ 0 & 0 & R^2 \end{bmatrix} \ . \tag{B.8}$$

Since we also know that $g_{ij}\cdot g^{ij} = I$, where I is the identity matrix, we can easily determine the contravariant counterpart by calculating the inverse of g_{ij}. This yields

$$g^{ij} = \begin{bmatrix} \frac{1}{(1-\Delta'\cos\theta)^2} & -\frac{\Delta'\sin\theta}{r(1-\Delta'\cos\theta)^2} & 0 \\ -\frac{\Delta'\sin\theta}{r(1-\Delta'\cos\theta)^2} & \frac{1-2\Delta'\cos\theta+(\Delta')^2}{r^2(1-\Delta'\cos\theta)^2} & 0 \\ 0 & 0 & \frac{1}{R^2} \end{bmatrix} \ , \tag{B.9}$$

where the prime denotes a derivative with respect to r. Another quantity of interest that follows directly from g_{ij} is the jacobian given by

$$\mathcal{J} = \sqrt{|g_{ij}|} = rR(1-\Delta'\cos\theta) \ , \tag{B.10}$$

where $|g_{ij}|$ denotes the determinant of g_{ij}.

The final quantity we would like to determine in this coordinate system is the magnetic field $\mathbf{B}$. For this geometry we can write

$$\mathbf{B} = g\nabla\theta + f\nabla\varphi \ , \tag{B.11}$$

where f and g can be determined from $\mathbf{B} = \nabla\alpha \times \nabla\psi$ (α is given by Eq. 2.53). If we compute $\mathbf{B} \cdot \nabla\theta$ and $\mathbf{B} \cdot \nabla\varphi$ in both descriptions we can find

$$g = \frac{1}{\mathcal{J}|\nabla\theta|^2} \quad \text{and} \quad f = -\frac{q}{\mathcal{J}|\nabla\varphi|^2}\left[1 - \cos\theta\left(\frac{r}{R_0} + \Delta'\right)\right] \ . \tag{B.12}$$

With these values in terms of known quantities the magnitude of the magnetic field is straightforward to calculate and can be written as

$$\frac{B}{B_0} \sim 1 - \frac{r}{R_0}\cos\theta + \mathcal{O}(\epsilon^2) \ , \tag{B.13}$$

where $\epsilon \doteq r/R_0$.

C

The GYRO Code

Before discussing any of the numerical schemes used in the code, it is convenient to write the gyrokinetic and Poisson equations derived in Chapter 2 using the appropiate units, and introduce the following additional normalizations

$$n_{0s(r)} = n_{0s}^{nr}(r) n_e \quad , \qquad h_{sn}(r) = \frac{h_{sn}^{nr}(r) F_{0s}}{n_{0s}(r)} \qquad \text{and} \quad \phi = \frac{T_e \phi^{nr}}{e} \quad . \tag{C.1}$$

Above, the superscript nr refers to a normalized quantity, the subscript n is a mode number and the subscript s is a species label. For simplicity, unshifted circular equilibrium will be used in the following discussion. Using the GYRO units, the gyrokinetic equation (Eq. 2.27) with the relevant drifts (Eqs. 2.69, 2.70 and 2.71) becomes

$$\begin{aligned} \frac{\partial h_{sn}}{\partial t} &+ \left[\frac{v_\parallel}{q R_0} \frac{\partial}{\partial \theta} - i \omega_{ds}^{(1)} - i \omega_{ds}^{(r)} \frac{\partial}{\partial r} \right] \left(h_{sn} + z_s \alpha_s \overline{\delta \phi}_n \right) + i n_{0s} \omega_{*s} \overline{\delta \phi}_n \\ &- i \hat{\rho} \left\{ \overline{\delta \phi}, h_s \right\}_n = C(h_{sn}) \ , \end{aligned} \tag{C.2}$$

where the curvature and diamagnetic terms are given by

$$\omega_{ds}^{(1)} \doteq k_\theta \rho_s \frac{2T_s}{z_s R_0} \epsilon \left(1 - \frac{v_\perp^2}{2v^2} \right) \left[\cos\theta + s\theta \sin\theta \right] \ , \tag{C.3}$$

$$\omega_{ds}^{(r)} \doteq -i \rho_s \frac{2T_s}{z_s R_0} \epsilon \left(1 - \frac{v_\perp^2}{2v^2} \right) \sin\theta \ , \tag{C.4}$$

$$\omega_{*s} \doteq k_\theta \rho_s \left[\frac{a}{L_{ns}} + \left(\epsilon - \frac{3}{2} \right) \frac{a}{L_{Ts}} \right] \ . \tag{C.5}$$

Notice that in these equations all quantities are normalized even though the superscript nr does not appear (omitted for clarity). Also, new definitions were introduced, namely

$\alpha_s \doteq n_{0s}/T_s$, $\epsilon \doteq m_s v^2/2T_s$ and $\rho_s \doteq c_s/\Omega_{c1}$ where the subscript 1 refers to the primary species. The Poisson equation (Eq. 2.38) is practically unchanged and can be written as

$$\sum_s^{n_{ion}} \alpha_s z_s^2 \left[\delta\phi(\mathbf{x},t) - \overline{\overline{\delta\phi}}(\mathbf{x},t)\right] = \sum_s^{n_{kinetic}} z_s \delta N_s(\mathbf{x},t) \ . \tag{C.6}$$

C.1 Code variables

The equations presented in Chapter 2 and the actual equations solved by the code differ slightly in the choice of variables. The connection between both sets is straightforward and can be written as

$$h_{sn}(r,\theta,\varphi,\varepsilon,\mu,t) \to h_{sn}^G(r,\tau,\varphi,\lambda,\epsilon,t) \ , \tag{C.7}$$

where the superscript G refers to GYRO and (r,θ,φ) are the usual radial, poloidal and toroidal coordinates. On the left hand side $\varepsilon \doteq v^2/2 + (z_s e/m_s)\Phi_0(\mathbf{x})$ is the total energy, $\mu \doteq v_\perp^2/(2B)$ is the magnetic moment and t is the time. On the right hand side side τ denotes the orbit time, $\lambda \doteq v_\perp^2/v^2$ and $\epsilon \doteq m_s v^2/2T_s$ is the kinetic energy. Inside the actual code, the indices are written using the following order and notation

$$h_{sn}^G(r,\tau,\varphi,\lambda,\epsilon,t) \to \mathtt{h}\left[\mathtt{m},\mathtt{i},\{\mathtt{ie},\mathtt{k}\},\mathtt{is}\right] \ , \tag{C.8}$$

where

$$\begin{aligned} \mathtt{m} &\to \tau \ , \\ \mathtt{i} &\to r \ , \\ \mathtt{ie} &\to \epsilon \ , \\ \mathtt{k} &\to \lambda \ , \\ \mathtt{is} &\to s \ . \end{aligned} \tag{C.9}$$

In the expression above, the brackets indicate distributed variables among processors and `is` denotes a species index (ions and electrons).

C.2 Numerical techniques

The discretization schemes used in each dimension are briefly discussed in this section. A detailed presentation, which is outside the scope of this work, can be found in Ref. [20].

C.2.1 Radius ($r \rightarrow \texttt{i}$)

Radial derivatives are treated with upwind or central differences depending on the term. For the case of advective derivatives ($\omega_{ds}^{(r)}\partial/\partial r$) the former method is used, whereas derivatives on fields (ϕ_n, h_{sn}) are treated with the latter one. Nonlocal operators such as the gyroaverage operator are approximated using a pseudospectral representation. The order of all discretizations is adjusted at run-time. Radial boundary conditions are either periodic (flux-tube) or nonperiodic (global).

C.2.2 Poloidal angle ($\tau \rightarrow \texttt{m}$)

The motion due only to parallel advection can be written as

$$\frac{\partial h_{sn}}{\partial t} + \frac{v_\parallel(\theta)}{qR_0}\frac{\partial \overline{h}}{\partial \theta} = 0 \ , \tag{C.10}$$

where $\overline{h} \doteq h_{sn} + z_s\alpha_s\overline{\delta\phi}_n$. However, the use of a θ-grid is a poor choice for the solution of the gyrokinetic equation. The main reason is that a singularity in $\partial/\partial\theta$ develops at bounce points θ_b, where $v_\parallel(\theta_b) = 0$, affecting the accuracy of any finite difference scheme. To solve this problem the following transformation is used

$$\frac{v_\parallel(\theta)}{qR_0}\frac{\partial}{\partial\theta} \rightarrow \Omega\frac{\partial}{\partial\tau} \ , \tag{C.11}$$

where τ is the orbit time and Ω is independent of the poloidal angle θ. Once this is done, an upwind scheme in τ is used to discretize $\partial/\partial\tau$. Finally, the use of such grid requires that the Poisson equation is solved by expansion of fields in complex finite-elements. The simulations presented in this work used 20 orbit gridpoints per trapped particle, and 10 orbit gridpoints per passing particle for each sign of velocity. For the ions a third-order upwind scheme was used, whereas for the electrons a fourth-order centered scheme was chosen. With respect to the Poisson equation we typically used six piecewise-quadratic elements in its solution.

C.2.3 Toroidal angle ($n \rightarrow \texttt{n}$)

The toroidal direction is treated in a fully spectral manner. However, simulations need not cover a complete toroidal loop $(0, 2\pi]$ since turbulence is essentially local. Instead, a partial torus is usually simulated. In more detail, we know from Chapter 2 that perturbed quantities such as h_s can be represented as

$$h_s = \sum_{j=0}^{n_n - 1} h_{sn} \, e^{-ij\Delta n \alpha} \quad , \tag{C.12}$$

where n_n is the number of toroidal modes used in the simulation and $\alpha = \varphi - q\theta$ (unshifted circular equilibrium only). The perturbed quantity h_s is $2\pi/\Delta n$-periodic in φ for fixed θ. Most of the simulations presented in this dissertation used 16 modes or less with a typical separation between modes ($\Delta n = 50$) allowing to cover about $1/50^{\mathrm{th}}$ of the torus.

C.2.4 Velocity Space ($(\lambda, \epsilon) \rightarrow (\texttt{k}, \texttt{ie})$)

A transformation property under integration of velocity-space integrals over θ is used to recast the velocity-space integration. Then, in both ϵ and λ, an exact Gauss-Legendre quadrature scheme [84] is numerically generated at run-time. This is different at each radius and for different plasma equilibria. The typical values used in this thesis were four passing pitch-angles, four trapped pitch-angles, eight energy gridpoints and two signs of velocity, for a total of 128 points in velocity space.

C.2.5 Nonlinearity

The nonlinear Poisson bracket $\left\{\overline{\delta\phi}, h_s\right\}$ represents the $\mathbf{E}\times\mathbf{B}$ nonlinearity. This is defined as

$$\{f, g\} = \frac{\partial f}{\partial \alpha}\frac{\partial g}{\partial r} - \frac{\partial g}{\partial \alpha}\frac{\partial f}{\partial r} \quad , \tag{C.13}$$

and evaluated with a conservative analogue of the Arakawa method [8]. This scheme ensures the exact conservation of density and generalized entropy, by re-writing the bracket as

$$\begin{aligned}\{f,g\} = \frac{1}{3}\Bigg[\frac{\partial}{\partial\alpha}\left(f\frac{\partial g}{\partial r} - g\frac{\partial f}{\partial r}\right) \\ - \frac{\partial}{\partial r}\left(f\frac{\partial g}{\partial\alpha} - g\frac{\partial f}{\partial\alpha}\right) + \frac{\partial f}{\partial\alpha}\frac{\partial g}{\partial r} - \frac{\partial g}{\partial\alpha}\frac{\partial f}{\partial r}\Bigg] \ .\end{aligned} \tag{C.14}$$

In this dissertation, the above terms were evaluated with a combination of differences and spectral methods, since the typical number of modes was not high. However, a fully spectral option via fast Fourier transforms is also available.

C.2.6 Time-advance

Once all the spatial operators are discretized and the system reduced to a set of ordinary differential equations, a time-advance scheme is used. This technique is referred to as the method of lines. The resulting initial value problem (IVP) can be written as

$$\frac{dh}{dt} = L_{NS}(h) + L_S(h) + NL(h) \quad \text{with} \quad t \in [t_0, t_1] \ . \tag{C.15}$$

Here L_{NS} is a non-stiff linear term, L_S is a stiff linear term, NL is the nonlinear term and $h \rightarrow \mathtt{h}$. In this system the stifness parameter, which is given by $\mu \doteq \sqrt{m1/m_e}$, appears in the $v_\parallel$ term of the electron equations, and consequently it is only relevant when ion and electron dynamics are included. The code has a number of available time-integration schemes to address this IVP, which include Runge-Kutta (RK) and recently-developed implicit-explicit Runge-Kutta (IMEX-RK) schemes. The RK scheme is generally used in simulations with adiabatic species, although it can also be used for fully kinetic ones (i.e. ion and electron dynamics included), at a considerable computational cost. To address this problem the IMEX-RK schemes were developed. The basic idea behind IMEX-RK methods is to treat the stiff terms implicitly, whereas all other terms are treated explicitly making the scheme very useful for fully kinetic simulations. For instance, most of the simulations used in this thesis used a second order implicit-explicit scheme (IMEX2), combined with a fourth order Runge-Kutta method (RK4).

Bibliography

[1] ITER Physics Basis Editors. *Nucl. Fusion*, 39:2175, 1999.

[2] ITER Physics Basis Editors. *Nucl. Fusion*, 39:2137, 1999.

[3] J. Adam, W. Tang, and P. Rutherford. Destabilization of the trapped-electron mode by magnetic curvature drift resonances. *Phys. Fluids*, 19:561, 1976.

[4] C. Angioni, A. Peeters, X. Garbet, A. Manini, F. Ryter, and ASDEX Upgrade Team. Density response to central electron heating: theoretical investigations and experimental observations in asdex upgrade. *Nucl. Fusion*, 44:827, 2004.

[5] C. Angioni, A. Peeters, F. Jenko, and T. Dannert. Collisionality dependence of density peaking in quasilinear gyrokinetic calculations. *Phys. Plasmas*, 12:112310, 2005.

[6] C. Angioni, A. Peeters, G. Pereverzev, F. Ryter, G. Tardini, and ASDEX Upgrade Team. Theory-based modeling of particle transport in ASDEX Upgrade H-mode plasmas, density peaking, anomalous pinch and collisionality. *Phys. Plasmas*, 10:3225, 2003.

[7] T. Antonsen and B. Lane. Kinetic equations for low frequency instabilities in inhomogeneous plasmas. *Phys. Fluids*, 23:1205, 1980.

[8] A. Arakawa. Computational design for long-term numerical integration of the equations of fluid motion: Two-dimensional incompressible flow. part i. *J. Comput. Phys.*, 1:119, 1966.

[9] D. Baker. A perturbative solution of the drift kinetic equation yields pinch type convective terms in the particle and energy fluxes for strong electrostatic turbulence. *Phys. Plasmas*, 11:992, 2004.

[10] D. Baker and M. Rosenbluth. Density profile consistency and its relation to the transport of trapped versus passing electrons in tokamaks. *Phys. Plasmas*, 5:2936, 1998.

[11] D. Baker, M. Wade, C. Petty, M. Rosenbluth, T. Luce, J. deGrassie, B. Rice, R. Groebner, C. Greenfield, E. Doyle, C. Rettig, T. Rhodes, and M. Mahdavi. Particle transport phenomena in the DIII-D tokamak. *Nucl. Fusion*, 40:1003, 2000.

[12] M. Beer. *Gyrofluid Models of Turbulent Transport in Tokamaks.* PhD thesis, Princeton University, 1995.

[13] M. Beer, S. Cowley, and G. Hammett. Field-aligned coordinates for nonlinear simulations of tokamak turbulence. *Phys. Plasmas*, 2:2687, 1995.

[14] M. Beer and G. Hammett. Toroidal gyrofluid equations for simulations of tokamak turbulence. *Phys. Plasmas*, 3:4046, 1996.

[15] S. Braginskii. Transport processes in a plasma. In *Reviews of Plasma Physics*, volume 1, pages 205–311, New York, 1965. Consultants Bureau.

[16] R. Budny. Fusion alpha parameters in tokamaks with high dt fusion rates. *Nucl. Fusion*, 42:1383, 2002.

[17] D. Campbell. The physics of the International Thermonuclear Experimental Reactor FEAT. *Phys. Plasmas*, 8:2041, 2001.

[18] J. Candy, D. Borba, H. Berk, G. Huysmans, and W. Kerner. Nonlinear interaction of fast particles with Alfvén waves in toroidal plasmas. *Phys. Plasmas*, 4:2597, 1997.

[19] J. Candy and R. Waltz. Anomalous transport in the diii-d tokamak matched by supercomputer simulation. *Phys. Rev. Lett.*, 91:045001–1, 2003.

[20] J. Candy and R. Waltz. An eulerian gyrokinetic-maxwell solver. *J. Comput. Phys.*, 186:545, 2003.

[21] J. Candy, R. Waltz, and W. Dorland. The local limit of global gyrokinetic simulations. *Phys. Plasmas*, 11:L25, 2004.

[22] B. Carreras. Progress in anomalous transport research in toroidal magnetic confinement devices. *IEEE Trans. Plasma Sci.*, 25:1281, 1997.

[23] Y. Chen, S. Parker, B. Cohen, A. Dimits, W. Nevins, D. Schumaker, V. Decyk, and J. Leboeuf. Simulations of turbulent transport with kinetic electrons and electromagnetic effects. *Nucl. Fusion*, 43:1121, 2003.

[24] C. Cheng and H. Okuda. Numerical simulation of trapped-electron instabilities in toroidal geometry. *Phys. Rev. Lett.*, 41:1116, 1978.

[25] C. Cheng and K. Tsang. Electrostatic drift wave eigenmodes in tokamaks. *Nucl. Fusion*, 21:643, 1981.

[26] J. Connor. Magnetic confinement theory summary. *Nucl. Fusion*, 45:S1, 2005.

[27] J. Connor and R. Hastie. Low frequency stability theory of axisymmetric toroidal plasmas. i. general theory. *Plasma Phys.*, 17:97, 1975.

[28] J. Connor, R. Hastie, and J. Taylor. Shear, periodicity and plasma balloning modes. *Phys. Rev. Lett.*, 40:396, 1978.

[29] B. Coppi, H. Furth, M. Rosenbluth, and R. Sagdeev. Drift instability due to impurity ions. *Phys. Rev. Lett.*, 17:377, 1966.

[30] B. Coppi, M. Rosenbluth, and R. Sagdeev. Instabilities due to temperature gradients in complex magnetic field configurations. *Phys. Fluids*, 10:582, 1967.

[31] B. Coppi and C. Spight. Ion-mixing mode and model for density rise in confined plasmas. *Phys. Rev. Lett.*, 41:551, 1978.

[32] T. Dannert and F. Jenko. Gyrokinetic simulation of collisionless trapped-electron mode turbulence. *Phys. Plasmas*, 12:072309, 2005.

[33] A. Dimits, G. Bateman, M. Beer, B. Cohen, W. Dorland, G. Hammett, C. Kim, J. Kinsey, M. Kotschenreuther, A. Kritz, L. Lao, J. Mandrekas, W. Nevins, S. Parker, A. Redd, D. Shumaker, R. Sydora, and J. Weiland. Comparisons and physics basis of tokamak transport models and turbulence simulations. *Phys. Plasmas*, 7:969, 2000.

[34] A. Dimits, T. Williams, J. Byers, and B. Cohen. Scalings of ion-temperature-gradient-driven anomalous transport in tokamaks. *Phys. Rev. Lett.*, 77:71, 1996.

[35] J. Dong and W. Horton. Study of impurity mode and ion temperature gradient mode in toroidal plasmas. *Phys. Plasmas*, 2:3412, 1995.

[36] J. Dong, W. Horton, and W. Dorland. isotope scaling and η_i mode with impurities in tokamak plasmas. *Phys. Plasmas*, 1:3635, 1994.

[37] W. Dorland. *Gyrofluid Models of Plasma Turbulence.* PhD thesis, Princeton University, 1993.

[38] W. Dorland and G. Hammett. Gyrofluid turbulence models with kinetic effects. *Phys. Fluids B*, 5:812, 1993.

[39] W. Dorland, F. Jenko, M. Kotschenreuther, and B. Rogers. Electron temperature gradient turbulence. *Phys. Rev. Lett.*, 85:5579, 2000.

[40] D. Dubin, J. Krommes, C. Oberman, and W. Lee. Nonlinear gyrokinetic equations. *Phys. Fluids*, 26:3524, 1983.

[41] D. Ernst, P. Bonoli, P. Catto, W. Dorland, C. Fiore, R. Granetz, M. Greenwald, A. Hubbard, M. Porkolab, M. Redi, J. Rice, K. Zhurovich, and the Alcator C-Mod Group. Role of trapped electron mode turbulence in internal transport barrier control in the alcator c-mod tokamak. *Phys. Plasmas*, 11:2637, 2004.

[42] C. Estrada-Mila, J. Candy, and R. Waltz. Gyrokinetic simulations of ion and impurity transport. *Phys. Plasmas*, 12:022305, 2005.

[43] E. Frieman and L. Chen. Nonlinear gyrokinetic equations for low-frequency electromagnetic waves in general plasma equlibria. *Phys. Fluids*, 25:502, 1982.

[44] U. Frisch. *Turbulence, The Legacy of A.N. Kolmogorov.* Cambridge Univ. Press, U.K., 1995.

[45] X. Garbet, L. Garzotti, P. Mantica, H. Nordman, M. Valovic, H. Weisen, and C. Angioni. Turbulent particle transport in magnetized plasmas. *Phys. Rev. Lett.*, 91:035001–1, 2001.

[46] L. Garzotti, X. Garbet, P. Mantica, V. Parail, M. Valovic, G. Corrigan, D. Heading, T. Jones, P. Lang, H. Nordman, B. Pégourié, G. Saibene, J. Spence, P. Strand, J. Weiland, and contributors to the EFDA-JET Workprogramme. Particle transport and density profile analysis of different jet plasmas. *Nucl. Fusion*, 43:1829, 2003.

[47] J. Greene, J. Johnson, and K. Weimer. Tokamak equilibrium. *Phys. Fluids*, 14:671, 1971.

[48] T. Hahm. Nonlinear gyrokinetic equations for turbulence in core transport barriers. *Phys. Plasmas*, 3:4658, 1996.

[49] K. Hallatschek and W. Dorland. Giant electron tails and passing electron pinch effects in tokamak-core turbulence. *Phys. Rev. Lett.*, 95:055002, 2005.

[50] G. Hammett, M. Beer, W. Dorland, S. Cowley, and S. Smith. Developments in the gyrofluid approach to tokamak turbulence simulations. *Plasma Phys. Controlled Fusion*, 35:973, 1993.

[51] G. Hammett and F. Perkins. Fluid moment models for landau damping with application to the ion-temperature-gradient instability. *Phys. Rev. Lett.*, 64:3019, 1990.

[52] A. Hasegawa and K. Mima. Stationary spectrum of strong turbulence in magnetized nonuniform plasma. *Phys. Rev. Lett.*, 39:205, 1977.

[53] R. Hastie, K. Hesketh, and J. Taylor. Shear damping of two-dimensional drift waves in a large-aspect-ratio tokamak. *Nucl. Fusion*, 19:1223, 1979.

[54] R. Hazeltine and J. Meiss. *Plasma Confinement.* Dover, New York, 2003.

[55] W. Heidbrink and G. Sadler. The behaviour of fast ions in tokamak experiments. *Nucl. Fusion*, 34:535, 1994.

[56] F. Hinton and R. Hazeltine. Theory of plasma transport in toroidal confinement systems. *Rev. Mod. Phys.*, 48:239, 1976.

[57] F. Hinton, M. Rosenbluth, and R. Waltz. Reduced equations for electromagnetic turbulence in tokamaks. *Phys. Plasmas*, 10:168, 2003.

[58] W. Horton. Drift waves and transport. *Rev. Mod. Phys.*, 71:735, 1999.

[59] M. Isichenko, A. Gruzinov, and P. Diamond. Invariant measure and turbulent pinch in tokamaks. *Phys. Rev. Lett.*, 74:4436, 1995.

[60] F. Jenko. Particle pinch in collisionless drift-wave turbulence. *Phys. Plasmas*, 7:514, 2000.

[61] F. Jenko and B. Scott. Numerical computation of collisionless drift alfvén turbulence. *Phys. Plasmas*, 6:2705, 1999.

[62] J. G. Jr. Energetic ion distribution resulting from neutral beam injection in tokamaks. *J. Plasma Physics*, 16:149, 1976.

[63] M. Kotschenreuther. Invited talk 9i4. *Bull. Am. Phys. Soc.*, 33:2107, 1988.

[64] M. Kotschenreuther, G. Rewoldt, and W. Tang. Comparison of initial value and eigenvalue codes for kinetic toroidal plasma instabilities. *Comput. Phys. Commun.*, 88:128, 1995.

[65] J. Krommes. Systematic statistical theories of plasma turbulence and intermittency: Current status and future prospects. *Phys. Reports*, 283:5, 1997.

[66] M. Kruskal and R. Kulsrud. Equilibrium of a magnetically confined plasma in a toroid. *Phys. Fluids*, 1:265, 1958.

[67] W. Lee. Gyrokinetic approach in particle simulation. *Phys. Fluids*, 26:556, 1983.

[68] W. Lee, J. Krommes, C. Oberman, and R. Smith. Nonlinear evolution of drift instabilities. *Phys. Fluids*, 27:2652, 1984.

[69] W. Lee and W. Tang. Gyrokinetic particle simulation of ion temperature gradient drift instabilities. *Phys. Fluids*, 31:612, 1988.

[70] Z. Lin, T. Hahm, W. Lee, W. Tang, and R. White. Turbulent transport reduction by zonal flows: Massively parallel simulations. *Science*, 281:1835, 1998.

[71] R. Littlejohn. Variational principles of guiding centre motion. *J. Plasma Physics*, 29:111, 1983.

[72] C. Liu, M. Rosenbluth, and W. Tang. Dissipative universal instability due to trapped electrons in toroidal systems and anomalous diffusion. *Phys. Fluids*, 19:1040, 1976.

[73] G. Manfredi and R. Dendy. Test-particle transport in strong electrostatic drift turbulence with finite larmor radius effects. *Phys. Rev. Lett.*, 76:4360, 1996.

[74] G. McKee, M. Murakami, J. Boedo, N. Brooks, K. Burrell, D. Ernst, R. Fonck, G. Jackson, M. Jakubowski, R. L. Haye, A. Messiaen, J. Ongena, C. Rettig, B. Rice, C. Rost, G. Staebler, R. Sydora, D. Thomas, B. Unterberg, M. Wade, and W. West. Impurity-induced turbulence suppression and reduced transport in the diii-d tokamak. *Phys. Plasmas*, 7:1870, 2000.

[75] G. McKee, C. Petty, R. Waltz, C. Fenzi, R. Fonck, J. Kinsey, T. Luce, K. Burrell, D. Baker, E. Doyle, X. Garbet, R. Moyer, C. Rettig, T. Rhodes, D. Ross, G. Staebler, R. Sydora, and M. Wade. Non-dimensional scaling of turbulence characteristics and turbulent diffusivity. *Nucl. Fusion*, 41:1235, 2001.

[76] R. Miller, M. Chu, J. Greene, Y. Lin-liu, and R. Waltz. Noncircular, finite aspect ratio, local equilibrium model. *Phys. Plasmas*, 5:973, 1998.

[77] F. Miskane, X. Garbet, A. Dezairi, and D. Saifaoui. Anomalous particle pinch in tokamaks. *Phys. Plasmas*, 7:4197, 2000.

[78] H. Mynick and J. Krommes. Particle diffusion by magnetic perturbations of axisymmetric geometries. *Phys. Rev. Lett.*, 43:1506, 1979.

[79] H. Mynick and S. Zweben. Modification of turbulent transport by orbit averaging. *Nucl. Fusion*, 32:518, 1992.

[80] J. Myra, P. Catto, H. Mynick, and R. Duvall. Quasilinear diffusion in stochastic magnetic fields: Reconciliation of drift-orbit modification calculations. *Phys. Fluids B*, 5:1160, 1993.

[81] S. Parker and W. Lee. A fully nonlinear characteristic method for gyrokinetic simulation. *Phys. Fluids B*, 5:77, 1993.

[82] A. Peeters, C. Angioni, M. Apostoliceanu, G. Pereverzev, E. Quigley, F. Ryter, D. Strintzi, F. Jenko, U. Fahrbach, C. Fuchs, O. Gehre, J. Hobirk, B. Kurzan, C. Maggi, A. Manini, P. McCarthy, H. Meister, J. Schweinzer, J. Stober, W. Suttrop, G. Tardini, and the ASDEX Upgrade Team. Understanding of the density profile shape, electron heat transport and internal transport barriers observed in asdex upgrade. *Nucl. Fusion*, 45:1140, 2005.

[83] G. Pereverzev, C. Angioni, A. Peeters, and O. Zolotukhin. Theoretical predictions of the density profile in a tokamak reactor. *Nucl. Fusion*, 45:221, 2005.

[84] C. Pozrikidis. *Numerical Computation in Science and Engineering*. Oxford Univ. Press, U.S.A., 1998.

[85] D. Reiter, G. Wolf, and H. Kever. Burn condition, helium particle confinement and exhaust efficiency. *Nucl. Fusion*, 30:2141, 1990.

[86] G. Rewoldt. Alpha-particle effects on high-n instabilities in tokamaks. *Phys. Fluids*, 31:3727, 1988.

[87] G. Rewoldt. Comparison of high-n instabilities including alpha particle effects in bpx and tftr. *Nucl. Fusion*, 31:2333, 1991.

[88] F. Romanelli. Ion-temperature-gradient-driven modes and anomalous ion transport in tokamaks. *Phys. Fluids B*, 1:1018, 1989.

[89] M. Romanelli, C. Bourdelle, and W. Dorland. Effects of high density peaking and high collisionality on the stabilization of the electrostatic turbulence in the frascati tokamak upgrade. *Phys. Plasmas*, 11:3845, 2004.

[90] M. Rosenbluth and F. Hinton. Poloidal flow driven by ion-temperature-gradient turbulence in tokamaks. *Phys. Rev. Lett.*, 80:724, 1998.

[91] D. Ross and W. Dorland. Comparing simulation of plasma turbulence with experiment. ii. gyrokinetic simulations. *Phys. Plasmas*, 9:5031, 2002.

[92] P. Rutherford and E. Frieman. Drift instabilities in general magnetic field configurations. *Phys. Fluids*, 11:569, 1968.

[93] M. Schneider, L.-G. Eriksson, V. Basiuk, and F. Imbeaux. On alpha particle effects in tokamaks with a current hole. *Plasma Phys. Controlled Fusion*, 47:2087, 2005.

[94] P. Snyder. *Gyrofluid Theory and Simulation of Electromagnetic Turbulence and Transport in Tokamak Plasmas*. PhD thesis, Princeton University, 1999.

[95] G. Staebler, J. Kinsey, and R. Waltz. Gyro-landau fluid equations for trapped and passing particles. *Phys. Plasmas*, 12:102508, 2005.

[96] R. Sydora. Toroidal gyrokinetic particle simulations of core fluctuations and transport. *Phys. Scr.*, 52:474, 1995.

[97] J. Taylor and R. Hastie. Stability of general plasma equilibria. i. formal theory. *Plasma Phys.*, 10:479, 1968.

[98] P. Terry, W. Anderson, and W. Horton. Kinetic effects on the toroidal ion pressure gradient drift mode. *Nucl. Fusion*, 22:487, 1982.

[99] P. Terry and W. Horton. Stochasticity and the random phase approximation for three electron drift waves. *Phys. Fluids*, 25:491, 1982.

[100] M. Valovic, R. Budny, L. Garzotti, X. Garbet, A. Korotkov, J. Rapp, R. Neu, O. Sauter, P. deVries, B. Alper, M. Beurskens, J. Brzozowski, D. McDonald, H. Leggate, C. Giroud, V. Parail, I. Voitsekhovitch, and JET EFDA contributors. Density peaking in low collisionality elmy h-mode in jet. *Plasma Phys. Controlled Fusion*, 46:1877, 2004.

[101] M. Vlad, F. Spineanu, S.-I. Itoh, M. Yagi, and K. Itoh. Turbulent transport of ions with large larmor radii. *Plasma Phys. Controlled Fusion*, 47:1015, 2005.

[102] M. Wade, D. Hillis, J. Hogan, R. Maingi, M. M. M. Mahdavi, W. West, K. Burrell, P. Gohil, R. Groebner, R.-M. Hong, D. Kellman, J. Phillips, R. Seraydarian, the DIII-D Team, and D. Finkenthal. Helium transport and exhaust studies in enhanced confinement regimes in diii-d. *Phys. Plasmas*, 2:2357, 1995.

[103] R. Waltz. Rho-star scaling and physically realistic gyrokinetic simulations of transport in DIII-D. *Fus. Sci. Technol.*, 48:1051, 2005.

[104] R. Waltz, J. Candy, F. Hinton, C. Estrada-Mila, and J. Kinsey. Advances in comprehensive simulations of transport in tokamaks. *Nucl. Fusion*, 45:741, 2005.

[105] R. Waltz, J. Candy, and C. Petty. Projected profile similarity in gyrokinetic simulations of bohm and gyrobohm scaled DIII D L- and H-modes. *Submitted to Phys. Plasmas*, 2006.

[106] R. Waltz and R. Dominguez. Note on detailed models for trapped electron transport in tokamaks. *Phys. Fluids B*, 1:1935, 1989.

[107] R. Waltz, R. Dominguez, and G. Hammett. Gyro-landau fluid models for toroidal geometry. *Phys. Fluids B*, 4:3138, 1992.

[108] R. Waltz, G. Kerbel, and J. Milovich. Toroidal gyro-landau fluid model turbulence simulations in a nonlinear ballooning mode representation with radial modes. *Phys. Plasmas*, 1:2229, 1994.

[109] R. Waltz, G. Kerbel, J. Milovich, and G. Hammett. Advances in the simulation of toroidal gyro-landau fluid model turbulence. *Phys. Plasmas*, 2:2408, 1995.

[110] R. Waltz, W. Pfeiffer, and R. Dominguez. Electrostatic drift waves in tokamaks: a numerical study of instability and transport. *Nucl. Fusion*, 20:43, 1980.

[111] R. Waltz, G. Staebler, W. Dorland, G. Hammett, M. Kotschenreuther, and J. Konings. A gyro-landau fluid transport model. *Phys. Plasmas*, 4:2482, 1997.

[112] A. Ware. Pinch effect for trapped particles in a tokamak. *Phys. Rev. Lett.*, 25:15, 1970.

[113] H. Weisen, A. Zabolotsky, C. Angioni, I. Furno, X. Garbet, C. Giroud, H. Leggate, P. Mantica, D. Mazon, J. Weiland, L. Zabeo, K.-D. Zastrow, and JET-EFDA contributors. Collisionality and shear dependences of density peaking in jet and extrapolation to iter. *Nucl. Fusion*, 45:L1, 2005.

[114] R. White. *The theory of toroidally confined plasmas.* Imperial College Press, London, 2001.

[115] R. White and H. Mynick. Alpha particle confinement in tokamaks. *Phys. Fluids B*, 1:980, 1989.

[116] V. Yancov. The pinch effect explains turbulent transport in tokamaks. *JETP Lett.*, 60:171, 1994.

[117] A. Zabolotsky, H. Weisen, and TCV Team. Observation and empirical modelling of the anomalous particle pinch in tcv. *Plasma Phys. Controlled Fusion*, 45:735, 2003.

[118] A. Zabolotsky, H. Weisen, and TCV Team. Density profile peaking in the presence of ecrh heating in tcv. *Plasma Phys. Controlled Fusion*, 48:369, 2006.

[119] S. Zweben, R. Budny, D. Darrow, S. Medley, R. Nazikian, B. Stratton, E. Synakowski, and G. Taylor. Alpha particle physics experiments in the tokamak fusion test reactor. *Nucl. Fusion*, 40:91, 2000.

[120] S. Zweben, D. Darrow, S. Batha, R. Budny, and M. Diesso. Effects of $q(r)$ on the alpha particle ripple loss in TFTR. *Nucl. Fusion*, 38:739, 1998.

[121] S. Zweben, S. Medley, and R. White. Summary of alpha particle transport. *Nucl. Fusion*, 38:1345, 1998.